



저작자표시-비영리-동일조건변경허락 2.0 대한민국

이용자는 아래의 조건을 따르는 경우에 한하여 자유롭게

- 이 저작물을 복제, 배포, 전송, 전시, 공연 및 방송할 수 있습니다.
- 이차적 저작물을 작성할 수 있습니다.

다음과 같은 조건을 따라야 합니다:



저작자표시. 귀하는 원저작자를 표시하여야 합니다.



비영리. 귀하는 이 저작물을 영리 목적으로 이용할 수 없습니다.



동일조건변경허락. 귀하가 이 저작물을 개작, 변형 또는 가공했을 경우에는, 이 저작물과 동일한 이용허락조건하에서만 배포할 수 있습니다.

- 귀하는, 이 저작물의 재이용이나 배포의 경우, 이 저작물에 적용된 이용허락조건을 명확하게 나타내어야 합니다.
- 저작권자로부터 별도의 허가를 받으면 이러한 조건들은 적용되지 않습니다.

저작권법에 따른 이용자의 권리는 위의 내용에 의하여 영향을 받지 않습니다.

이것은 [이용허락규약\(Legal Code\)](#)을 이해하기 쉽게 요약한 것입니다.

[Disclaimer](#)

공학박사 학위논문

Fabrication and Characterization of
Three-Dimensional Plasmonic Devices
Utilizing Aerosol-Derived Nanoparticles

에어로졸 나노입자를 적용한 3 차원 플라즈모닉
소자의 제조와 특성 분석

2014 년 8 월

서울대학교 대학원

기계항공공학부

정 기 남

에어로졸 나노입자를 적용한 3 차원
플라즈모닉 소자의 제조와 특성 분석

Fabrication and Characterization of Three-Dimensional
Plasmonic Devices Utilizing Aerosol-Derived Nanoparticles

지도 교수 최 만 수

이 논문을 공학박사 학위논문으로 제출함
2014 년 4 월

서울대학교 대학원
기계항공공학부
정 기 남

정기남의 공학박사 학위논문을 인준함.
2014 년 6 월

위 원 장 _____ 이 창 희



부위원장 _____ 최 만 수



위 원 _____ 전 누 리



위 원 _____ 고 승 환



위 원 _____ 정 현 석



FABRICATION AND CHARACTERIZATION OF
THREE-DIMENSIONAL PLASMONIC DEVICES UTILIZING
AEROSOL-DERIVED NANOPARTICLES

A Thesis Presented to Seoul National University
for the Degree of Doctor of Philosophy

August 2014

KINAM JUNG

Dedicated to my beloved family and parents.

Fabrication and Characterization of Three-Dimensional Plasmonic Devices Utilizing Aerosol-Derived Nanoparticles

Kinam Jung

School of Mechanical and Aerospace Engineering

The Graduate School

Seoul National University

Abstract

In this study I applied bottom-up type dry aerosol technology to fabricate plasmonic devices such as organic solar cells and surface-enhance Raman scattering (SERS) by constructing nanoparticle-assembled three-dimensional nanoarchitecture platform.

Firstly, I have demonstrated a considerable enhancement both in J_{SC} and PCE of the plasmonic PCDTBT : PC₇₀BM solar cells employing the NBA composed of MoO₃ layer and Ag NPs under the active layer,

compared to the reference devices including MoO₃ hole extraction layer(HEL) without nanoparticles (NPs). Here, the NPs with different diameters (Ag 20, 40, and 60 nm) have been generated by the evaporation and condensation method using the aerosol process in dry environment without aggregation, impurity, and contamination issues that can usually happen in the wet synthesis. Finite-difference time domain (FDTD) calculation results on scattering cross-sections and near field profiles inside the active materials show higher intensities with a strong forward scattering effect in the devices with the nanobump assembly (NBA) than those with the flat PEDOT:PSS. J-V characteristics show that J_{SC} increases continuously as the size of NPs increases and the best performance is achieved at the device embedding NBA-40. The improved performance depending on the size of NPs is explained by the strong forward light scattering effect coming from near-field enhancement in the vicinity of Ag NP in the visible region, as well as the multi-reflection between the cathode and the nanobump anode in the near IR region. Therefore, this approach can be a promising platform for efficient light harnessing in a broad spectral range for use in diverse OPV devices.

Secondly, I studied 3D mesoscopic multipetal flowers assembled by metallic nanoparticles as a SERS substrate. Seven orders of SERS enhancement, sufficiency for single molecule detection, and

multiresonance features in whole visible frequency range were achieved by plasmonic hot-spot engineering through increasing the number of petals from four to eight. By performing DF imaging, spectrum measurements, and FEM analysis I addressed that hot-spots and multipole resonance modes are responsible for peculiar optical properties of multipetal flower structures. Because the nanofabrication technique based on atmospheric spark discharge and electrostatic parallel focusing has capability to construct well-defined, uniform, and reproducible 3D nanostructures in wafer scales, it can not only open the way for manufacturing a reliable 3D SERS substrate sufficient for single molecule detection, but apply to a broad range of novel plasmonic devices.

To conclude, novel 3D plasmonic devices utilizing aerosol-derived metal nanoparticles were demonstrated, which would pave the way for the future development of diverse nanoscale optoelectric devices with maneuvering their surface plasmon traits in a broad spectral range.

Keywords: aerosol-derived nanoparticle, spark discharge method, evaporation and condensation method, organic solar cells, surface-enhanced Raman scattering (SERS), surface plasmon

Student Number: 2009-30168

PUBLICATIONS

1. Jung, K. et al. Plasmonic Organic Solar Cells Employing Nanobump Assembly via Aerosol-Derived Nanoparticles. *ACS Nano*, 8, 2590–2601 (2014).
2. Jung, K. et al. Hotspot-Engineered 3D Multipetal Flower Assemblies for Surface-Enhanced Raman Spectroscopy. *Adv. Mater.* (2014). doi:10.1002/adma.201401004

CONTENTS

i	INTRODUCTION	1
1	INTRODUCTION	3
1.1	Objective and Outline of the Research	3
1.2	Aerosol Synthesis for Plasmonic Devices	5
1.2.1	Spark Discharge Method	5
1.2.2	Evaporation and Condensation Method	6
1.3	Plasmonics	8
1.3.1	Basic Concept and Applications	8
ii	AEROSOL-DERIVED NANOPARTICLE BASED PLASMONIC DEVICES: PLASMONIC ORGANIC SOLAR CELLS	9
2	PLASMONIC ORGANIC SOLAR CELLS	11
2.1	Introduction	12
2.1.1	Metal Nanoparticles	12
2.1.2	PEDOT : PSS vs. MoO ₃	12
2.1.3	Nanobump architecture via Aerosol Process	13
2.1.4	Outline of the Research	14
2.2	Results and discussion	15
2.2.1	The Fabrication Process of the Plasmonic OPV Employing Nanobump Assembly	15
2.2.2	Evaporation and Condensation Method	17
2.2.3	FDTD Simulation : Cross-sections and E-field distributions of NBA OPV	17
2.2.4	FDTD Simulation : Near Field Radiation Patterns of NBA OPV	20
2.2.5	J-V and IPCEs characteristics of NBA OPV	24
2.2.6	J-V, IPCE, and PL characteristics of devices with different HEL layers	26
2.2.7	TEM analysis and EDS mapping data for the NBA with different sizes of Ag NP	32
2.2.8	Steady-state and time resolved PL of PCDTBT layer on the NBA structure	32
2.2.9	Exciton generation rate of the OPVs with and without Ag NPs	34

2.2.10	Absorption enhancement of PCDTBT : PC ₇₀ BM with and without the NBA	36
2.2.11	J-V characteristics of the OPVs with different concentrations and sizes	37
2.2.12	Device parameters of OPV embedding the NBA with different volume concentrations	37
2.2.13	Multi-reflection effect with and without Al cathode within plasmonic OPV cells	40
2.3	Experiment and Method	40
2.3.1	3D FDTD simulation for CS and IPCE enhancement	40
2.3.2	Device fabrication and electro-optical measurement	41
2.4	Conclusions	42
	Bibliography	42
iii	AEROSOL-DERIVED NANOPARTICLE BASED PLASMONIC DEVICES: SERS	49
3	SERS (SURFACE-ENHANCED RAMAN SCATTERING)	51
3.1	Introduction	52
3.1.1	Surface plasmon	52
3.1.2	SERS Substrate	52
3.1.3	Outline	53
3.2	Result and Discussion	54
3.2.1	IAAL(ion-assisted aerosol lithography) for Nanoflower Arrays	54
3.2.2	Fabrication of Multipetal Nanoflower Arrays using IAAL Method	55
3.2.3	SERS Experiments	57
3.2.4	Electromagnetic Simulations for Four and Eight Petal Nanostructures	60
3.2.5	Dark field(DF) microscopy : DF Spectra and DF Images	61
3.2.6	Reproducible and Uniform SERS Substrate of <i>m</i> -PF Arrays	61
3.3	Experiment	72
3.3.1	SERS Enhancement Factor Calculation	72
3.3.2	Penetration Depth	74
3.3.3	SERS Experiment	75

3.3.4	Dark field (DF) Microscopy	76
3.3.5	Method for SERS experiment	76
3.3.6	Method for DF experiment	80
3.4	Conclusions	83
	Bibliography	83

LIST OF FIGURES

- Figure 1 The aerosol nanoparticle fabrication platform for the plasmonic optoelectronic devices 4
- Figure 2 IAAL method for SERS substrate (a) Schematic of spark discharge chamber (b) nanoparticle assembly process 6
- Figure 3 The schematic of evaporation and condensation aerosol setup for organic solar cells 7
- Figure 4 Excitation of plasmon from incident electromagnetic field interacting with free electrons in the conduction band of nanoparticles 8
- Figure 5 The fabrication process of the plasmonic OPV employing nanobump assembly : (a) preparation of a cleaned ITO substrate, (b) Ag NPs deposition on the ITO substrate via the evaporation and condensation method, (c) thermal evaporation of MoO₃ nanobump layer on Ag NPs / ITO, (d) spin coating of PCDTBT : PC₇₀BM active layer on MoO₃ layer, (e) thermal evaporation of LiF and Al electrode on the active layer, (f) schematic cross-section of completed device: ITO / Ag 40 / MoO₃ / PCDTBT : PC₇₀BM / LiF / Al, (g) cross-sectional TEM image and its corresponding EDS data showing the elements of Ag and Mo in the NBA (scale bar : 50 nm). 16
- Figure 6 (a) Schematic of the evaporation and condensation setup to generate Ag NPs and deposit them onto the substrate sample. (b) FE-SEM images of Ag 20, 40, and 60 coated on ITO electrodes. The insets represent the size distribution of the NPs generated by the aerosol method (scale bar: 500 nm). 18

- Figure 7 (a) Schematics of the FDTD simulation structures of Ag NPs in the different HELs (PEDOT : PSS, flat MoO₃, NBA, and without HEL) surrounded by PCDTBT : PC₇₀BM, and calculated scattering cross-sections (CS) for differently sized Ag NPs : (b) Ag 20, (c) 40, and (d) 60. (e) The ratio of scattering CS to absorption CS as a function of particle diameter in different surrounding media. Here, PF-d, FM-d, and NBA-d represent d nm Ag NPs embedded within PEDOT : PSS, flat MoO₃, and NBA, respectively, surrounded by PCDTBT : PC₇₀BM, while w/o HEL-d denotes d nm Ag NPs surrounded only by the PCDTBT : PC₇₀BM without HEL. 21
- Figure 8 Calculated electric field distributions in xz-plane at LSPR peak of the NBA-40 ($\lambda = 533$ nm) for the schematics shown in (a): (f) FP-40, (g) FM-40, (h) NBA-40, and (i) w/o HEL-40. 22
- Figure 9 FDTD simulations on near field radiation patterns arising from the plasmonic resonance peaks of the NBA for the flat PEDOT : PSS, flat MoO₃, NBA, and without HEL embedding (a) Ag 20, (b) 40, and (c) 60 in xz-plane, and (d) Ag 20, (e) 40, and (f) 60 in yz-plane. 23
- Figure 10 (a) J-V characteristics of the plasmonic OPVs with the NBA incorporating sized NPs (NBA-20, 40, and 60). (b) IPCEs of the OPVs with the NBA. (c) The IPCE enhancement ratio and (d) calculated absorption enhancement ratios of the plasmonic solar cells as a function of wavelength. The inset graphs in (c) and (d) illustrate the enhancement ratio in a full scale. 27

- Figure 11 (a) The J-V characteristics of devices with different HEL layers. The solid lines denote the devices with Ag 40, while the dash lines represent the devices without Ag NP. (b) The IPCE data and their enhancement ratios compared to each reference sample (c) Steady-state PL spectra of PCDTBT films with different buffer layers (d) Time resolved PL ($\lambda = 690$ nm) of PCDTBT films with the NBA-40 compared to the FP-40, where the numbers represent the exciton lifetime inside each active material. Here, the measured data (symbols) are fitted using exponential functions (solid lines). 31
- Figure 12 Cross-sectional S-TEM images and their EDS analysis to confirm the morphology and existence of the NBA embedding (a) Ag 20, (b) 40, and (c) 60. 33
- Figure 13 (a) Steady-state PL spectra and (b) transient PL of PCDTBT (80 nm) films with and without the NBA. The sizes of NPs for NBA are 20, 40, and 60 nm. 34
- Figure 14 Photocurrent density (J_{ph}) versus effective voltage characteristics of the OPVs incorporating Ag NPs with different diameters. 35
- Figure 15 Absorption spectra of PCDTBT : PC₇₀BM (a) with and without the NBA structure containing various sizes of NPs, and (b) with and without 40 nm Ag NPs inside PEDOT : PSS. (c) The absorption enhancement of the NBA-40 and the FP-40 with respect to each reference sample. 36
- Figure 16 (a) The analysis of J-V characteristics for the OPVs with differently sized Ag-NPs under dark condition and white illumination of AM 1.5G 100 mW/cm² J-V characteristics of the OPVs with different concentrations of Ag 60 and without NPs, (b) under illumination, and (c) dark condition. (d) The representative S-TEM image of the NBA-60. 38

- Figure 17 Device performance parameters: (a) Efficiency, (b) J_{SC} , (c) FF, and (d) V_{OC} of the NBA-20, 40, and 60, as a function of volume concentration under illumination. 39
- Figure 18 (a) Schematic of light trapping and multi-reflection by the excitation of LSPR and scattering of the devices with the NBA, (b) calculated absorption enhancement versus wavelength for Ag NPs incorporated devices with the Al electrode (solid line) and without the one (dash line). 40
- Figure 19 Fabrication of plasmonic 3D multipetal flower (*m*-PF) arrays and illustration of ion-assisted focusing lenses. (a) Scheme of *m*-PF building method using spark discharge device. (b) cross-sectional view illustrating assembly process of nanoparticles for 4-PF array through ion-assisted focusing lenses: a flat structure in an early stage (left), full grown flower structure in a 3D building stage (right). 56
- Figure 20 FE-SEM images of fabricated multipetal flowers (*m*-PF) arrays with etched pattern geometries at each left top corner. (a) 4-PF (b) 6-PF (c) 8-rPF (d) 8-tPF (scale bar: 1000 nm). 57
- Figure 21 (a) Schematic illustration of SERS substrate configuration for a multipetal architecture (left) and a particle film (right). These SERS configurations consist of three steps: copper nanoparticle deposition on the substrate via spark discharge, 50 nm thick gold layer sputtering on the structure, and BT molecules binding on the top gold layer. (b) Raman spectra of BT molecules for the particle film, 4-, 6-, 8-r, and 8-tPF array (scale bar: 1000 nm). 59

- Figure 22 Electromagnetic simulation results of the 4-PF. (a) Schematic view of the simulation model (left), model structure and geometry (middle), a cross-section location of A-A line (right). (b) 3D perspective view (top) and 2D electric field distributions in the plane containing A-A (bottom), (c) The electric field distribution at $z = 220$ nm for unpolarized light. 62
- Figure 23 Electromagnetic simulation results of the 8-tPF. (a) Schematic view of the simulation model (left), model structure and geometry (middle), a cross-section location of B-B line (right). (b) 3D perspective view (top) and 2D electric field distributions in the plane containing B-B (bottom), (c) The electric field distribution at $z = 300$ nm for unpolarized light 63
- Figure 24 DF spectra, DF images of a 4-PF and an 8-tPF, and calculated surface charge density distributions. DF spectra and images (inset) of the 4-PF (a) and the 8-tPF (b). Surface charge density distributions of the 4-PF (c and d) and the 8-tPF (e and f) at $\lambda = 495$ nm (c and e) and $\lambda = 700$ nm (d and f) for the x- polarized light. 64
- Figure 25 DF images of gold film coated copper nanoparticle multipetal arrays with m-fold symmetric multicolor distribution : (a) 4-PF (b) 6-PF (c) 8-rPF (d) 8-tPF (Scale bar : 3000 nm) 65
- Figure 26 FE-SEM images of fabricated multipetal flower arrays for two different samples. (a) 4-PF (b) 6-PF (c) 8-rPF (d) 8-tPF arrays in the SERS sample 1 and (e) 4-PF (f) 6-PF (g) 8-rPF (h) 8-tPF arrays in the SERS sample 2 (scale bar: 1000 nm). 68

- Figure 27 Raman spectra of BT molecules for (a) gold coated Cu particle film on Si substrate (b) spin-coated Au NPs ($d = 50$ nm) on Si substrate (c) gold coated pre-patterned samples (having SiO_2 etched part as shown in Figure 20) without Cu nanoparticles deposition. Each schematic inset at the bottom side represents the experiment configuration for SERS substrate. Each inset table at the top right corner demonstrates Raman intensity of the BT molecules at 1575 cm^{-1} . 69
- Figure 28 Raman spectra of BT molecules for (a) 4-PF (b) 6-PF (c) 8-rPF (c) 8-tPF arrays of the SERS substrate sample 1 depicted in Figure 26 (a)-(d). Each inset table at the top right corner demonstrates Raman intensity of the BT molecules at 1575 cm^{-1} for five different locations. 70
- Figure 29 Raman spectra of BT molecules for (a) 4-PF (b) 6-PF (c) 8-rPF (c) 8-tPF arrays of the second SERS substrate sample 2 depicted in Figure 26 (e)-(h). Each inset table at the top right corner demonstrates Raman intensity of the BT molecules at 1575 cm^{-1} for five different locations. 71
- Figure 30 Schematic representation of Raman spectroscopy system for measuring SERS signals (top), SERS experimental setup of confocal micro-Raman microscope (bottom) 77
- Figure 31 Schematic representation of dark-field spectroscopy system for measuring spectra and images (top), experimental setup for dark-field spectroscopy (bottom) 78
- Figure 32 Raman experiments for bulk BT solution (left), BT adsorbed SERS substrate (right) 81

LIST OF TABLES

Table 1	Ratios of scattering CS to absorption CS for differently sized Ag NPs in each HEL	20
Table 2	Device performance of the plasmonic solar cells containing the NBA with differently sized NPs ^a	28
Table 3	Exciton generation rate and its enhancement for the devices with NBA and reference sample with 20 nm of MoO ₃ HEL	28
Table 4	Comparison of device performance for the NBA-40 and the FP-40. ^a	30
Table 5	Device performance of the NBA-60 with different concentrations. The values inside parenthesis represent the amounts of increase in percentage with respect to that of the reference cell without NPs.	35
Table 6	Raman intensities and enhancement factors of BT molecules (10^{-4} M) for particle film and <i>m</i> -PF arrays at 1575cm^{-1}	58
Table 7	Average Raman intensities of BT molecules at 1575 cm^{-1} and their differences for 3D multipetal flower arrays obtained from two different SERS substrates sample 1 and 2 (SEM images shown in Figure 26).	70
Table 8	Calculated ratios of $ E ^4$ integration for 4-PF (8-tPF) over the SERS volume covering multipetal surface with variation of the layer thickness ($t = 10 - 50\text{ nm}$) compared to that of gold coated film.	71
Table 9	Comparison of penetration depths with respect to calculations and references	74

Part I

INTRODUCTION

INTRODUCTION

1.1 OBJECTIVE AND OUTLINE OF THE RESEARCH

The objective of this research is to fabricate and characterize three-dimensional plasmonic devices such as organic photovoltaics (OPVs) and SERS (surface-enhanced Raman scattering) utilizing aerosol-derived nanoparticles. In this study I realized bottom-up type dry aerosol technology (at room temperature and atmospheric condition) into both plasmonic devices for constructing nanoparticle-assembled nanoarchitecture platform so as to enhance their performances or efficiencies. This research is mainly dealt with the fabrication and characterization of 1) plasmonic OPV and 2) SERS devices via aerosol process and 3) electromagnetic field simulations for those plasmonic devices. I implemented silver and copper nanoparticles (NPs) from two different aerosol syntheses (evaporation and condensation, spark discharge) into the plasmonic devices to increase near-field intensity around the nanoparticle-assembled structure. Evaporation and condensation is applied to organic solar cell for larger silver nanoparticle generation (> 20 nm), whereas spark discharge method is applied to the SERS application for smaller copper nanoparticle generation (< 10 nm). The objective and outline of this research are summarized in Figure 1.

In organic solar cells, 20 ~ 60 nm sized three-dimensional (3D) spherical silver nanoparticle (NPs) are randomly deposited onto the ITO-coated glass via evaporation and condensation. The efficiency of OPV employing Ag NPs is increased to 18% owing to the near-field enhancement plasmonic effect, increased forward scattered light, and amplified multireflection from aerosol-derived Ag NPs. I characterized the optical and electrical properties of Ag NPs embedded nanobump assembly (NBA) structured polymer solar cell. The optical characteristics of the plasmonic NBA OPVs are theoretically calculated by FDTD (finite-difference time domain) method.

In SERS device, 3 ~ 5 nm sized copper NPs are assembled into 3D complex flower-like nanostructures via IAAL (ion-assisted aerosol lithog-

Aerosol Nanoparticle(NP) Fabrication Platform Pave the Way for Plasmonic Optoelectronic Devices

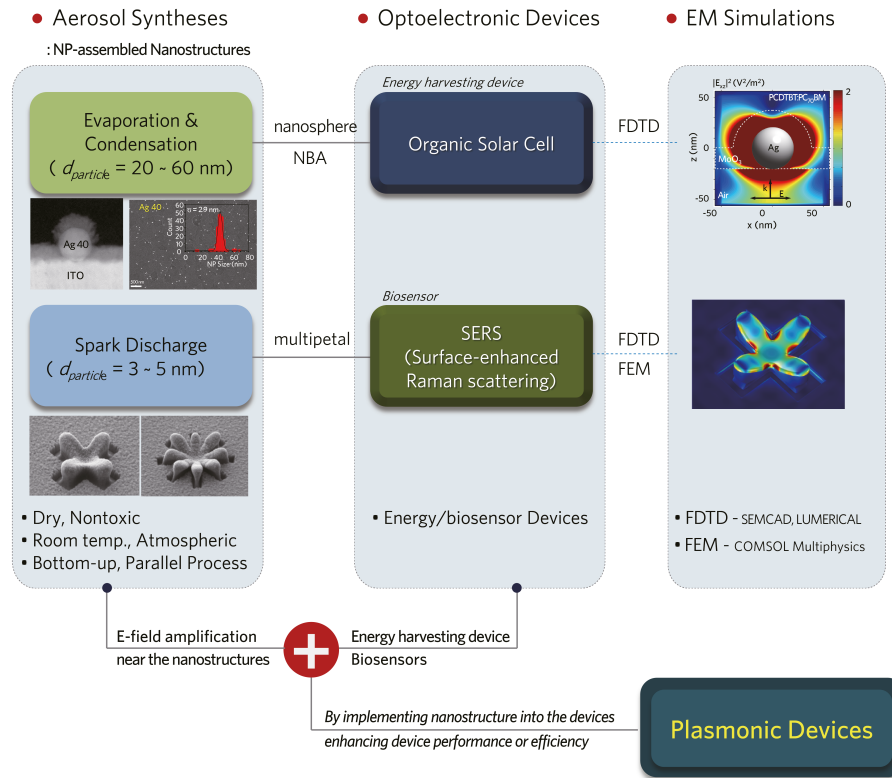


Figure 1: The aerosol nanoparticle fabrication platform for the plasmonic optoelectronic devices

raphy) using spark discharge chamber onto the SiO_2 prepatterned Si substrate. I maneuvered various shapes of 3D metallic multipetal architectures like four, six, and eight petal nanoflowers to engineer the hotspots formed within the nanogaps between neighbouring petals. As a results, I achieved to fabricate the uniform and reproducible SERS substrate whose enhancement factor was order of 10^7 enough to detect single molecular detection. Electromagnetic field distributions of four and eight petal nanoflowers are analyzed using FEM(finite element method) code to identify hotspots between nanogaps and SERS enhancement factors.

1.2 AEROSOL SYNTHESIS FOR PLASMONIC DEVICES

1.2.1 *Spark Discharge Method*

I fabricated 3D plasmonic multipetal SERS substrates using spark discharge and ion induced electrostatic focusing method. The homemade spark discharge device is constructed by three chambers schematically shown in Figure 2a: a pin-to-plate type spark and a corona discharge chamber and a deposition chamber. In the spark discharge chamber a sharpened copper pin and a copper plate with a hole (~ 1 mm in diameter) are fixed with a distance of about 1 mm. Prior to the charged nanoparticle generation process, positive N_2 ions generated in the corona discharge chamber are deposited on the surface of SiO_2 which is patterned on a Si substrate. In the spark discharge chamber electric sparks are periodically generated between the pin and the plate by applying a positive voltage to the pin and connecting a ground to the plate. Electric sparks evaporate quasi-instantaneously copper, and charged copper nanoparticles (2 - 4 nm in diameter) are produced and blown into the deposition chamber by N_2 carrier gas fed into the spark discharge chamber. In the deposition chamber, a patterned electrically insulating SiO_2 layer with a 100 nm thickness on a Si substrate is biased by a negative voltage through the sample holder to attract only positive copper nanoparticles. Due to the repulsive Coulomb interaction from deposited N_2 positive ions on the surface of the SiO_2 layer, positively charged copper nanoparticles can be convergently assembled onto the center of bare Si surface in etched SiO_2 area.

At the early stage equi-potential lines determined by positive nitrogen ions on the SiO_2 layer and the negative voltage on the Si substrate form a convex electrostatic lens which focuses electric field lines on the bare Si surface. Therefore, positively charged copper nanoparticles following the electric field lines are deposited on the center region of etched area within the SiO_2 layer. As assembled metal nanoparticles pile up in the vertical direction, quasi-electrostatic field lines change. In the 3D building stage, the attractive lenses covering the open area in the SiO_2 layer are weakened and suppressed by the neighboring repelling lenses, which eventually allows nanoparticles to grow in the lateral direction as well. The repelling fields act as an electrostatic scaffold which determines lateral shapes of 3D nanoparticle buildings.

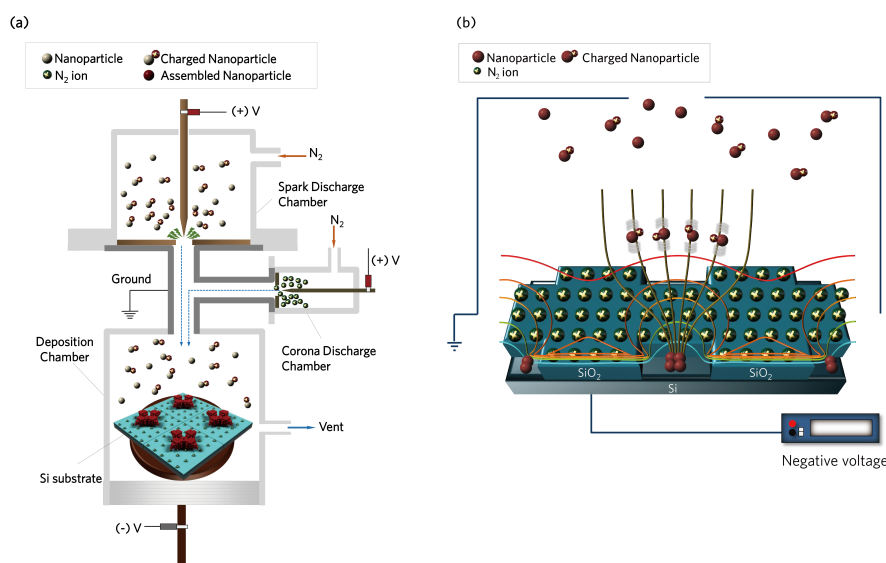


Figure 2: IAAL method for SERS substrate (a) Schematic of spark discharge chamber (b) nanoparticle assembly process

1.2.2 Evaporation and Condensation Method

Figure 3a depicts the experimental setup for the evaporation and condensation method via the aerosol process, which consists of a tube furnace, a nano-differential mobility analyzer (nano-DMA), a DMA controller, a neutralizer, a high voltage power supply, two mass flow controllers (MFCs), and a deposition chamber in a glove box. To deposit Ag NPs on the substrate, a solid silver strip was placed at the end of quartz tube located inside the center of the tube furnace. Two MFCs were utilized to supply N₂ carrier gas with 1.5 standard liter per minute into the quartz tube. As the tube furnace was heated at 1150 °C, the Ag NPs were generated. After the high temperature NPs passed through cooling water line maintaining 26 °C, charged NPs were grown by condensation and coagulation processes. The ionized poly-dispersive Ag NPs were produced via a neutralizer, and positively charged mono-dispersive NPs were classified by the nano-DMA and the DMA controller. By varying the applied voltage according to particle's electrical mobility through the DMA controller, I could classify silver NPs with well-defined sizes.

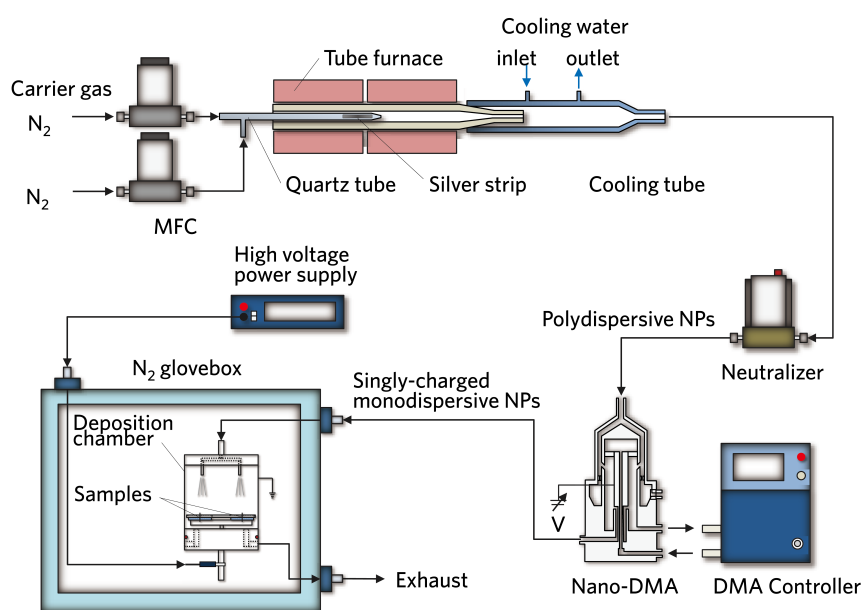


Figure 3: The schematic of evaporation and condensation aerosol setup for organic solar cells

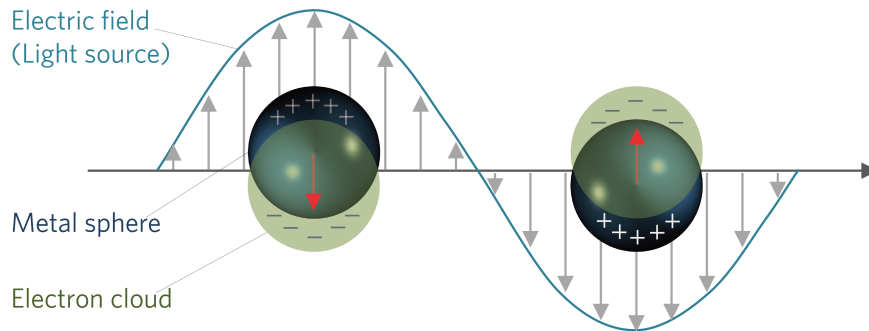


Figure 4: Excitation of plasmon from incident electromagnetic field interacting with free electrons in the conduction band of nanoparticles

1.3 PLASMONICS

1.3.1 Basic Concept and Applications

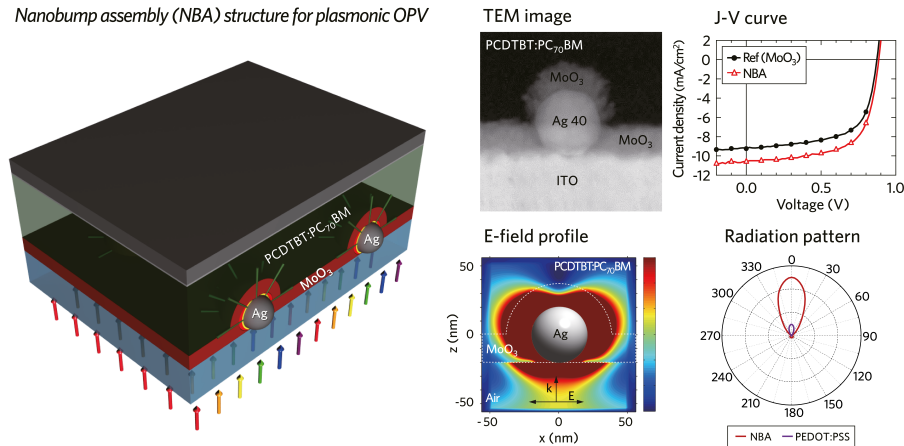
To enhance the device performance or efficiency, plasmonic metal nanoparticles, i.e., silver, gold, and copper, can be incorporated into the target device. Surface plasmon (SP) has been one of intensively studied subjects in optical and material science in the last two decades. As a collective electric charge density oscillation of metal at dielectric-metal interface, SP resonance brings about strong electric field in the vicinity of metal surface (refer to Figure 4). Intensive studies on optical properties of SP depending on the size, the material, and the morphology of diverse dielectric-metal compositions revealed high potential of SP for its ubiquitous applications; such as biochemical sensors, surface-enhanced Raman spectroscopy (SERS), nanooptical components, negative refractive index materials, and photovoltaic devices.

Part II

AEROSOL-DERIVED NANOPARTICLE BASED
PLASMONIC DEVICES: PLASMONIC ORGANIC
SOLAR CELLS

PLASMONIC ORGANIC SOLAR CELLS

Nanobump assembly (NBA) structure for plasmonic OPV



I report the effect of a nanobump assembly (NBA) constructed with molybdenum oxide (MoO₃) covering Ag nanoparticles (NPs) under the active layer on the efficiency of plasmonic polymer solar cells. Here, the NPs with precisely controlled concentration and size have been generated by an atmospheric evaporation/condensation method and a differential mobility classification and then deposited on an indium tin oxide electrode via room temperature aerosol method. NBA structure is made by enclosing NPs by MoO₃ layer via vacuum thermal evaporation to isolate the undulated active layer formed onto the underlying protruded NBA. Simulated scattering cross-sections of the NBA structure reveal higher intensities with a strong forward scattering effect than those from the flat buffer cases. Experimental results of the device containing the NBA show 24% enhancement in short-circuit current density and 18% in power conversion efficiency compared to the device with the flat MoO₃ without the NPs. The observed improvements are attributed to the enhanced light scattering and multi-reflection effects arising from the NBA structure combined with the undulated active layer in the visible and near-infrared regions. Moreover, I demonstrate that the NBA adopted devices show better performance with longer

exciton lifetime and higher light absorption in comparison with the devices with Ag NPs incorporated flat poly (3,4-ethylenedioxythiophene) poly (styrenesulfonate) (PEDOT : PSS). Thus, the suggested approach provides a reliable and efficient light harvesting in a broad range of wavelength, which consequently enhances the performance of various organic solar cells.

2.1 INTRODUCTION

2.1.1 *Metal Nanoparticles*

Bulk heterojunction organic photovoltaics (OPVs) consisting of an interpenetrating donor- acceptor network have been extensively studied for their advantages such as thin, light-weight, flexible, large-area features, as well as simple and cost-effective processes.[1][2] It is well known that the thickness of OPVs is limited to several tens of nm for the effective charge collection with reduced recombination losses due to lower mobility and shorter exciton diffusion length of organic materials compared to inorganic ones.[2][3] However, such thin film structure leads to insufficient light absorption in a photoactive layer, so the efficient light trapping and coupling with the active layer are required to improve the device efficiency. In this respect, metal nanoparticles (NPs) or nanostructures incorporated in single and tandem OPVs have been reported to improve efficiency in device performance,[4][5][6][7][8][9][10] which is mainly attributed to plasmonic near field enhancement and prolonged optical paths of the incident light onto the active layer by scattering elements.[9][11][12]

2.1.2 *PEDOT : PSS vs. MoO₃*

Meanwhile, the placement of metal NPs at different locations of OPVs enables one to manipulate different mechanisms for optical and (or) electrical enhancement in power conversion efficiency (PCE). [7][12][13] When a polymer based active layer and metal NPs are combined, the PCE is enhanced by the improvement in light absorption or electrical conductivity, but there is a concern on the possibility of exciton quenching in the active layer.[14][15] Thus, metal NPs are mainly incorporated in the interlayer of conventional OPVs between the indium tin

oxide (ITO) anode and the active layer: poly(3,4-ethylenedioxythiophene) poly(styrenesulfonate) (PEDOT : PSS), and there have been reports demonstrating the enhancement in the short-circuit current (J_{SC}) and the open-circuit voltage (V_{OC}). [5] [16][17] In those cases, the metallic NPs such as Ag, Au, and Cu have been mostly embedded within the PEDOT : PSS via wet chemical synthesis. [5][18] However, this wet approach involves large amounts of solvents and needs to use surfactants to avoid aggregation among the NPs. Also, there exist contamination problems from impurities during the particle generation, and it is hard to control the concentration and distribution of the NPs during a spin coating process. Moreover, the PEDOT : PSS layer has acidic and hygroscopic features, leading to instability of a device which also arises from etching the ITO electrode and migrating indium to an active layer.[19] Furthermore, degraded PEDOT : PSS is considered as a part of an insulating layer that would deteriorate the device performance.[20] In this regard, several metal oxides such as molybdenum oxide (MoO_3), vanadium oxide, tungsten oxide, and nickel oxide have been demonstrated as efficient hole extraction materials for OPV devices to replace the PEDOT : PSS. [21][22][23] Especially, MoO_3 is more stable in the air compared to the PEDOT : PSS and prevents the diffusion of moisture or oxygen into the active layer, resulting in longer lifetime or lower degradation rate. Hence, the OPVs fabricated with this oxide buffer layer has better performance in current density, mobility, and charge carrier conduction with good stability than the devices with the PEDOT : PSS layer. [19][24] Additionally, thermally evaporated metal oxide layer can uniformly follow the surface morphology of underlying nanostructures, while the PEDOT : PSS layer tends to maintain its flat morphology even on textured structures.

2.1.3 Nanobump architecture via Aerosol Process

In recent studies, MoO_3 /Ag NPs/ MoO_3 structure [25][26] and solution-processed Ag NPs- MoO_3 composite film [27] as a hole extraction layer (HEL) have been located on the flat active layer for inverted-type organic solar cells to enhance device performance by the enhanced light absorption via plasmonic backscattering[25][26] and the improvement of the carrier transport, [27] respectively. Here, the NPs were floated randomly inside the MoO_3 layer, while the active layer formed a flat

shape. In order to fully use the conformal property of the MoO_3 and, as a consequence, to induce enhanced light-matter interaction in the active layer, the NPs could be deposited prior to the active layer. In such case, the MoO_3 covering the NPs, deposited on an ITO electrode, as a HEL has a bumped shape, and the active layer itself is forced to have an undulated structure by the underlying MoO_3/Ag NPs. The increased interface area between the active layer and the anode electrode can be expected to contribute to the PCE enhancement in optical as well as electrical aspects. [28] In spite of these advantages, there have been few reports on the NPs embedded nanobump-plasmonic architecture placed under the active layer to enhance the PCE of OPVs, due to the inherent difficulty to precisely form textured metal-structures by conventional wet chemical process. To generate metallic NPs and nanostructures in a controlled manner, an aerosol approach utilizing the evaporation and condensation methods has been extensively studied since the work of Scheibel and Porstendörfer,[29] demonstrating various shapes and sizes of generated NPs [30] and local heating control. [31]

2.1.4 *Outline of the Research*

Therefore, in this report, I firstly demonstrate the 18% PCE enhancement of OPVs by implementing the nanobump assembly (NBA), constructed with the protruded MoO_3 covering the aerosol-derived Ag NPs, under the active layer in comparison with the device employing the flat HEL with the Ag NPs. Then, the underlying mechanism of enhanced device performance arising from the NBA combined with the undulated active layer is analyzed by simulations of cross-sections and absorption spectra, photoluminescence (PL), current density-voltage (J-V) characteristics, and incident photon conversion efficiency (IPCE). Moreover, the effect of Ag NP's size and concentration on device performance in the NBA structure is systematically studied in terms of the enhanced light trapping and multi-reflections through the aforementioned theoretical and experimental works. This study was performed together with Hyung-Jun Song in Department of Electrical and Computer Engineering at Seoul National University.

2.2 RESULTS AND DISCUSSION

2.2.1 *The Fabrication Process of the Plasmonic OPV Employing Nanobump Assembly*

Figure 1 a-e show the fabrication process for the plasmonic OPVs employing the NBA structure. First, I prepared an ITO-coated glass substrate, and then Ag NPs synthesized and classified by atmospheric evaporation/condensation and differential mobility classification methods were deposited on the ITO by room temperature aerosol process. After covering these Ag NPs with 20 nm vacuum-thermally-evaporated MoO₃ to implement the NBA, the mixture of the poly[N-9''-hepta-decanyl-2,7-carbazole-alt-5,5-(4',7'-di-2-thienyl-2',1',3'-benzothiadiazole) (PCDTBT) / [6,6]-phenyl C₇₀ butyric acid methyl-ester (PC₇₀BM) was spin-coated on top of the NBA. Finally, the device fabrication was completed by depositing 0.5 nm lithium-fluoride (LiF) and 100 nm aluminum electrode. Figure 1f shows a cross-sectional schematic of the completed OPVs incorporating the NBA structure. Cross-sectional transmission electron microscopy (TEM) images of the device embedding 40 nm Ag NPs (the left side of Figure 1g) show the conformal MoO₃ layer with a thickness of 20 nm on the upper half surface of the NPs, which is thick enough to fully cover the Ag NPs without significantly changing the PCE of devices. [32] In addition, mapping images for each material obtained by energy dispersive spectrometer (EDS) analysis in g clearly identify the distribution of the MoO₃ and the Ag NPs on the ITO electrode, confirming successful formation of the NBA structure with a protruding shape and a textured active layer. In this report, I denote the Ag NPs with an average diameter d nm as Ag d. Figure 8 also presents the conformal surface morphologies of the NBAs formed on top of Ag 20, 40, and 60. Small-sized Ag 20 and 40 were fully encapsulated by the MoO₃, while the lower part of Ag 60 was barely covered with the MoO₃ due to the inherent feature of a thermal evaporation process. It is likely that there would be little exciton quenching problem even for Ag 60 enclosed by the MoO₃ because the exciton lifetime of polymer casted on it, measured by time resolved PL, turns out to be the same as those of the NBAs with Ag 20 and 40 (See Figure 9). Therefore, I have successfully fabricated the OPVs that implement the NBA including Ag NPs generated by the evaporation and condensation method.

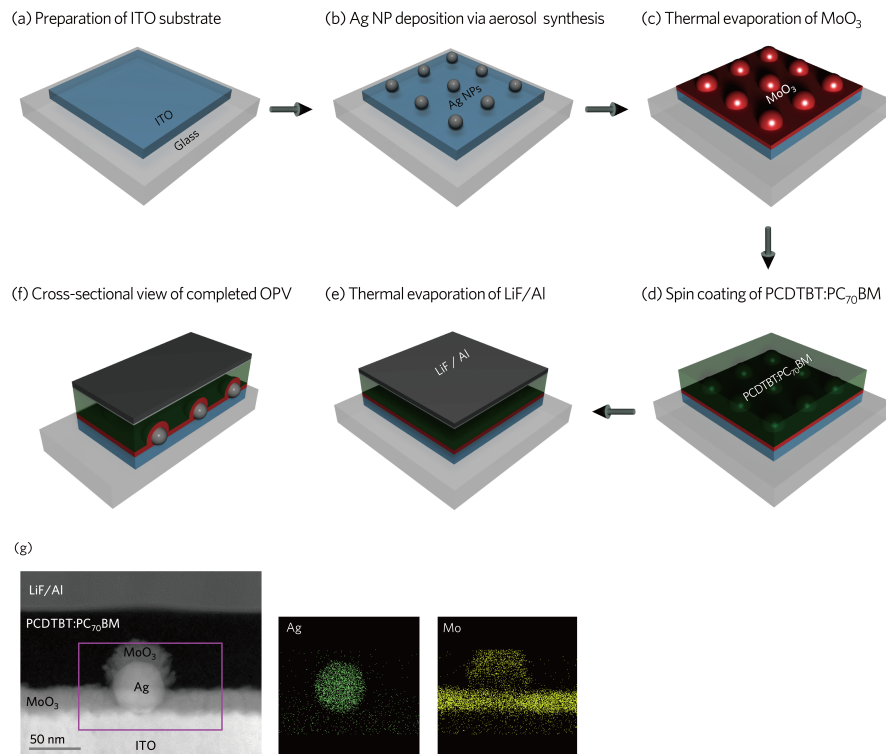


Figure 1: The fabrication process of the plasmonic OPV employing nanobump assembly : (a) preparation of a cleaned ITO substrate, (b) Ag NPs deposition on the ITO substrate via the evaporation and condensation method, (c) thermal evaporation of MoO₃ nanobump layer on Ag NPs / ITO, (d) spin coating of PCDTBT : PC₇₀BM active layer on MoO₃ layer, (e) thermal evaporation of LiF and Al electrode on the active layer, (f) schematic cross-section of completed device: ITO / Ag₄₀ / MoO₃ / PCDTBT : PC₇₀BM / LiF / Al, (g) cross-sectional TEM image and its corresponding EDS data showing the elements of Ag and Mo in the NBA (scale bar : 50 nm).

2.2.2 *Evaporation and Condensation Method*

Figure 2a depicts the experimental setup for the evaporation and condensation method via the aerosol process, which consists of a tube furnace, a nano-differential mobility analyzer (nano-DMA), a DMA controller, a neutralizer, a high voltage power supply, two mass flow controllers (MFCs), and a deposition chamber in a glove box. To deposit Ag NPs on the substrate, a solid silver strip (Alfaesar) was placed at the end of quartz tube located inside the center of the tube furnace (Okdu SiC tube furnace). Two MFCs (Tylan FC280S) were utilized to supply 99.999% N₂ carrier gas with 1.5 standard liter per minute into the quartz tube. As the tube furnace was heated at 1150 °C, the Ag NPs were generated. After the high temperature NPs passed through cooling water line maintaining 26 °C, charged NPs were grown by condensation and coagulation processes. The ionized poly-dispersive Ag NPs were produced via a neutralizer (HCT Aerosol Neutralizer 4530), and positively charged mono-dispersive NPs were classified by the nano-DMA (TSI 308500) and the DMA controller (AERIS). By varying the applied voltage according to particle's electrical mobility through the DMA controller such as 1.03, 3.93, and 8.42 kV, I could classify Ag 20, 40, and 60 with well-defined sizes. Here, I set the concentration of charged particle as $3.0 \times 10^5 \text{ cm}^{-3}$ on average, while depositing Ag NPs onto an ITO substrate. By regulating the deposition time, it is possible to control the surface density of Ag NPs on the ITO ranging from 0.2 to $1.5 \times 10^9 \text{ cm}^{-2}$. From the field emission-scanning electron microscopy (FE-SEM) images ($\times 50,000$ in magnification, $6.0 \mu\text{m} \times 4.2 \mu\text{m}$ in analysis area) in Figure 2b, it is confirmed that incorporated Ag 20, 40, and 60 are uniformly but randomly deposited onto the ITO with small standard deviations of their sizes (σ): $\sigma = 1.9, 2.9,$ and 2.5 nm for Ag 20, 40, and 60, respectively. This analysis was performed by the ImageJ software (version 1.46r).

2.2.3 *FDTD Simulation : Cross-sections and E-field distributions of NBA OPV*

To investigate the effect of the NBA structure on the optical enhancement, I analyzed near field profiles and radiation patterns using a three dimensional finite-difference time-domain (FDTD) solution pack-

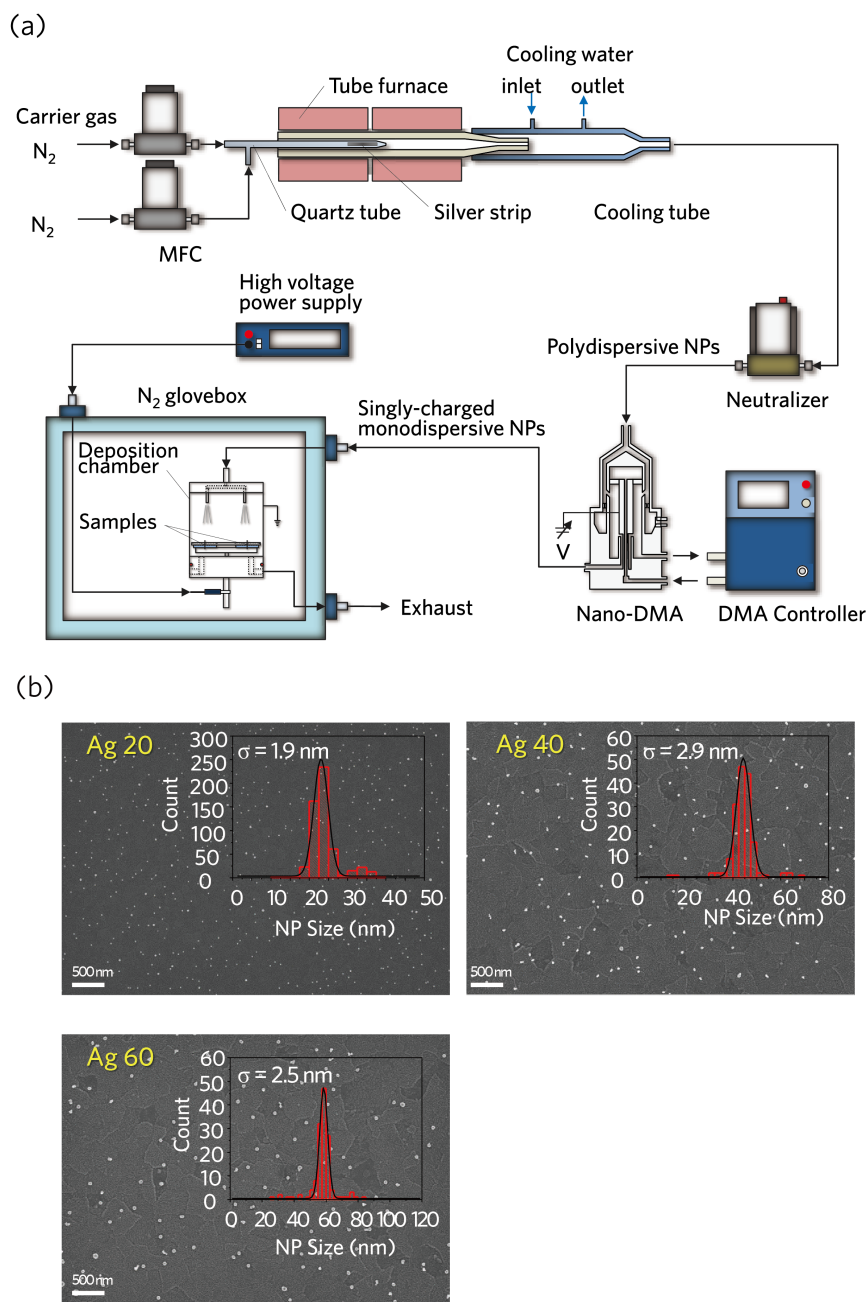


Figure 2: (a) Schematic of the evaporation and condensation setup to generate Ag NPs and deposit them onto the substrate sample. (b) FE-SEM images of Ag 20, 40, and 60 coated on ITO electrodes. The insets represent the size distribution of the NPs generated by the aerosol method (scale bar: 500 nm).

age (version 8.4.3, Lumerical solutions) for the Ag 20, 40, and 60 cases in which the NPs deposited on the ITO were enclosed by different HELs (MoO_3 , PEDOT : PSS) and then encompassed by the same background material (PCDTBT : PC_{70}BM). Figure 3a shows the schematics of simulated structures for the d nm Ag NPs embedded in the flat PEDOT : PSS (FP-d), flat MoO_3 (FM-d), and NBA (NBA-d) surrounded by the PCDTBT : PC_{70}BM , as well as Ag NPs without HEL (w/o HEL-d) immersed in the active layer. To compare with the aforementioned cases, Ag NPs within air background case (not shown here) were also simulated. Then, I calculated scattering cross-sections (CS) for the Ag 20, 40, and 60 cases where the NPs were located in the four different structures to investigate the variation of scattering intensities with respect to different refractive index (n) as shown in Figure 3b-d and Table 1. Simulated results show that the scattering CS increases and localized surface plasmon resonance (LSPR) peaks are red-shifted when the Ag NP size increases from 20 to 60 nm. The LSPR peak is shifted from 358 to 368 nm as the size of Ag NPs within air background increase from 20 to 60 nm, which is less than those for the other four cases. Since the optical refractive index of the PEDOT : PSS, MoO_3 , and PCDTBT : PC_{70}BM layers at visible wavelength are larger than that of air ($n = 1$), I anticipate that the LSPR spectra for those structures are more red-shifted compared to that of the NPs within air as the size of NPs increases. Especially, the NBA shows the highest value of scattering CS in the spectral range of 450 to 600 nm, which is well matched with the main absorption band of the PCDTBT : PC_{70}BM . As the diameter of Ag NPs increases from 20 to 60 nm, the degree of spectral shift in LSPR peaks for the NBA is relatively lower than those of the other cases shown in Figure 3b-d, but its intensity level is much higher than the other cases covering the whole absorption band of the active layer.

Figure 3e represents the ratio of scattering CS to absorption CS for Ag NPs at each maximum value with increasing the diameter from 20 to 60 nm in the four different surrounding materials, illustrating that the ratio is proportional to the Ag NP size. The CS ratio for the NBA-30, 40, 50, and 60 are 0.37, 0.61, 0.91, and 1.20, respectively, higher values than those of the other architectures (see Table 1). Since light scattering is much more dominant factor than absorption loss for extending the optical path length and light trapping efficiency within the active layer, the NBA enclosing Ag NPs within OPVs has a prominent enhancement

Table 1: Ratios of scattering CS to absorption CS for differently sized Ag NPs in each HEL

HEL	NP size (nm)				
	20	30	40	50	60
FP	0.31	0.29	0.46	0.57	0.88
FM	0.15	0.23	0.29	0.40	0.60
NBA	0.15	0.37	0.61	0.91	1.20
w/o HEL	0.02	0.07	0.17	0.39	0.74

of the plasmonic effect. To observe the degree of light propagation into the active layers, the electric field profiles for the Ag 40 embedded in different surrounding media were calculated as shown in Figure 4f-i: the scattered light from the NBA propagates farther into the active region than those from the other cases. Thus, the optically amplified fields in the vicinity of Ag NPs via LSPR coupling with the incident electromagnetic fields for the NBA case give rise to more enhanced light scattering and trapping effects within the active layer. [12]

2.2.4 FDTD Simulation : Near Field Radiation Patterns of NBA OPV

Figure 5 shows the calculated near field radiation patterns of FP-d, FM-d, NBA-d, and w/o HEL-d, with respect to xz - and yz -planes at each plasmon resonance peak of the NBA-20, 40, and 60. In all the cases, the radiated power intensities in xz - and yz -planes are proportional to the size of Ag NPs. The intensities of near fields for the NBA-20, 40, and 60 within the BHJ layer are higher than those of the other architectures: particularly, the intensities of the NBA both in xz - and yz -planes are at least four times larger than that of the flat MoO_3 . Also, the radiated field profiles of all the cases show strong forward scattering characteristics: especially the scattering intensities in xz - and yz -plane of the NBA are dominant over all the other cases. Thus, the incident light interacting with the NBA can be considerably harvested within the OPVs via forward scattering effect. Therefore, the simulation results on the optical near field reveal that the NBA can be a platform for outstandingly enhancing plasmonic OPV compared to the other architectures in the optical point of view.

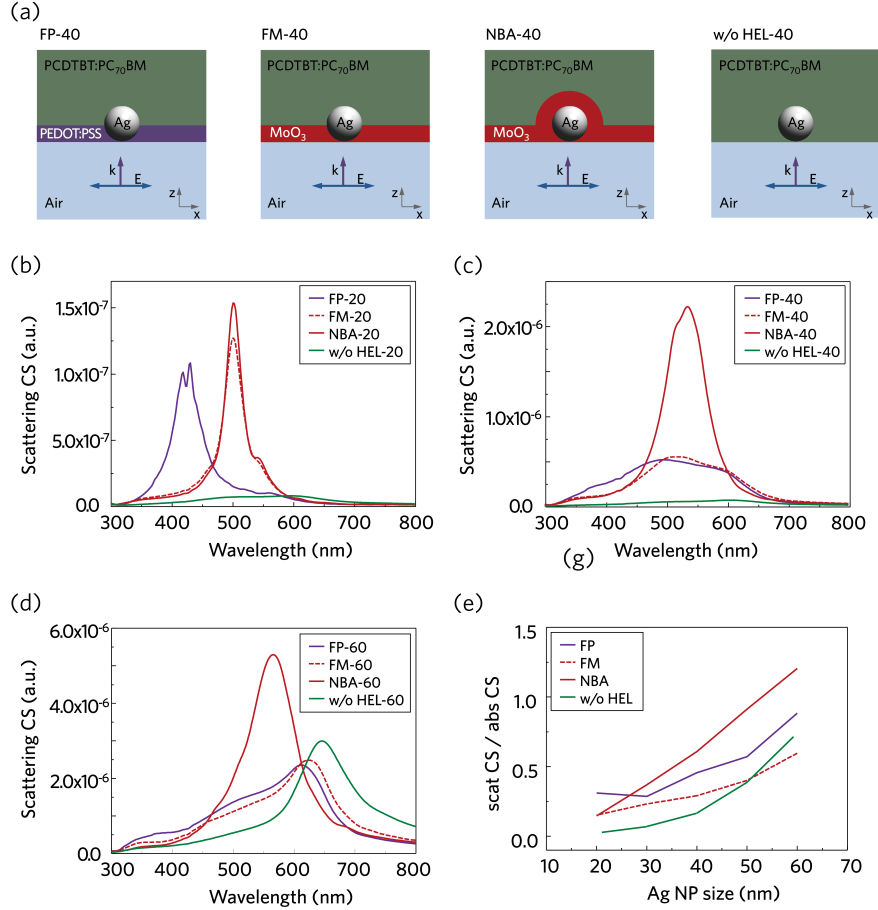


Figure 3: (a) Schematics of the FDTD simulation structures of Ag NPs in the different HELs (PEDOT : PSS, flat MoO₃, NBA, and without HEL) surrounded by PCDTBT : PC₇₀BM, and calculated scattering cross-sections (CS) for differently sized Ag NPs : (b) Ag 20, (c) 40, and (d) 60. (e) The ratio of scattering CS to absorption CS as a function of particle diameter in different surrounding media. Here, FP-d, FM-d, and NBA-d represent d nm Ag NPs embedded within PEDOT : PSS, flat MoO₃, and NBA, respectively, surrounded by PCDTBT : PC₇₀BM, while w/o HEL-d denotes d nm Ag NPs surrounded only by the PCDTBT : PC₇₀BM without HEL.

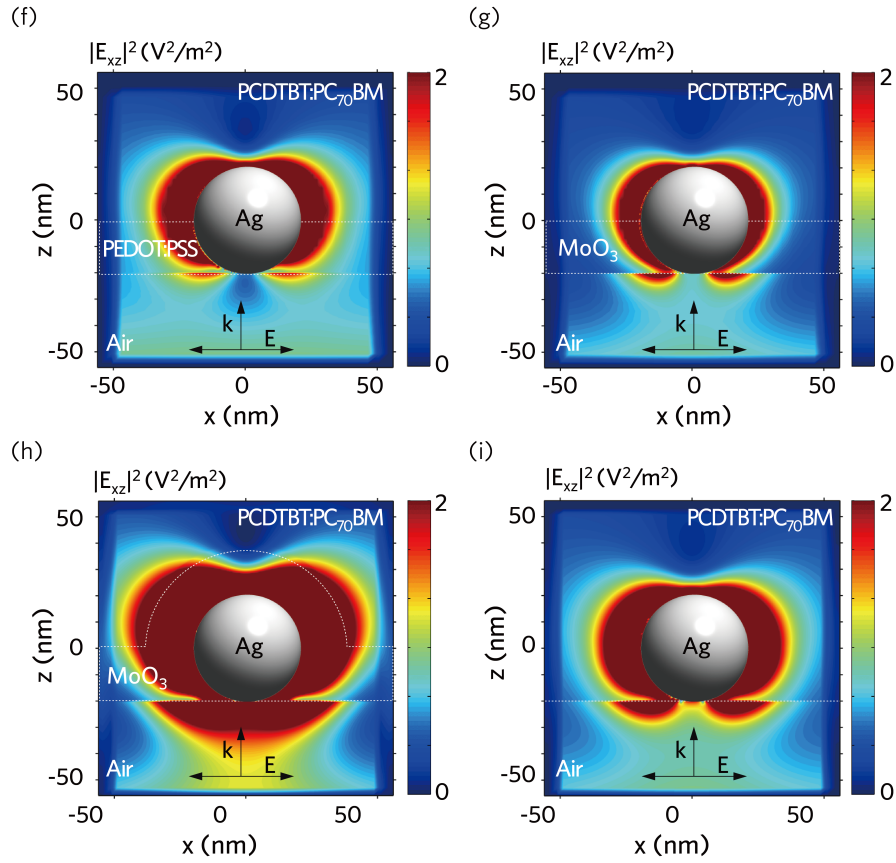


Figure 4: Calculated electric field distributions in xz -plane at LSPR peak of the NBA-40 ($\lambda = 533$ nm) for the schematics shown in (a): (f) FP-40, (g) FM-40, (h) NBA-40, and (i) w/o HEL-40.

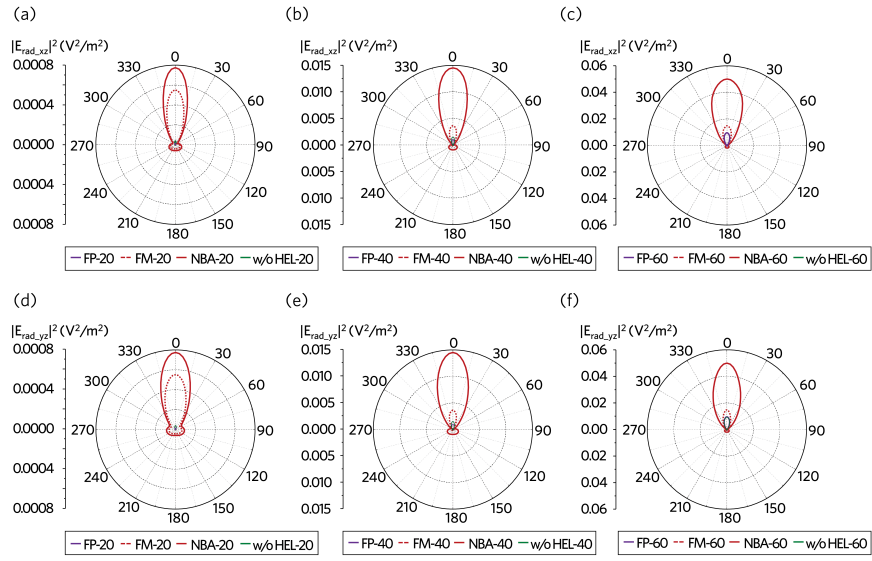


Figure 5: FDTD simulations on near field radiation patterns arising from the plasmonic resonance peaks of the NBA for the flat PEDOT : PSS, flat MoO_3 , NBA, and without HEL embedding (a) Ag 20, (b) 40, and (c) 60 in xz -plane, and (d) Ag 20, (e) 40, and (f) 60 in yz -plane.

2.2.5 *J-V and IPCEs characteristics of NBA OPV*

To quantify the effect of the combination of the NBA and the undulated active layer on device performance, OPVs incorporating the NBA with different diameters of 20, 40, and 60 nm were fabricated, and compared with the reference device including 20 nm MoO₃ HEL without Ag NPs. The J-V characteristics of the devices with the NBA structure and the reference device were taken under AM 1.5G 100 mW/cm² illumination as shown in Figure 6. The photovoltaic parameters for each case are summarized in Table 2. The PCE of the devices with NPs is improved from 5.16% in the reference device to 5.80% (NBA-20), 6.07% (NBA-40), and 5.65% (NBA-60), respectively. Interestingly, the observed improvement in the PCE is originated from the increase in J_{SC} from 9.16 mA/cm² (the reference device) to 10.15 mA/cm² (NBA-20), 10.58 mA/cm² (NBA-40), and 11.36 mA/cm² (NBA-60), accordingly. The enhancement ratio in J_{SC} is more than 10% without changing the V_{OC}. Especially, the photocurrent increases as the diameter of incorporated NPs increases, which is coincident with aforementioned optical simulation results showing the enhanced ratio of scattering to absorption CS in the NBA with large-size NPs. To further investigate underlying mechanism for the enhanced J_{SC} from the devices employing the NBA, I have measured exciton generation rates of the devices. The increased exciton generation rate (8.8% - 23.4%) of the devices with the NBA supports the enhancement in the photocurrent as shown in Figure 10 and Table 3. In addition, it is noted that the absorption intensities of the films with Ag NPs in visible region is higher than that of the counterpart without NPs (See Figure 11), which indicates the match between the enhanced plasmonic peaks induced by the NBA and the absorption band of PCDTBT : PC₇₀BM blend. Also, as the size of NPs increases, the absorption is enhanced, which is consistent with the measured photocurrents. Furthermore, the enhancement in a steady-state PL of PCDTBT layer casted on the NBA at a broad wavelength of 700 - 900 nm (See Figure 9) provides us direct evidence of plasmonic effects.^{8,17} Therefore, the higher PCE is mainly attributed to the optical enhancement in the devices embedding the NBA structure. Despite the highest J_{SC} of the OPV embedding NBA-60, the PCE of it is lower than those of NBA-20 and 40 because of the low fill factor (FF). Since the reverse dark current of the device with NBA-60 is two order of magnitude higher and its shunt resistance is lower

compared to those of the others, this reduction of FF can be mainly caused by the increased leakage current and recombination losses [33] (See Figure 12a). The leakage current might be attributed to the thin thickness of the active layer (approximately 20 to 30 nm) in the region where the Ag NPs were inserted between the anode and the cathode (Figure 12d). Many research groups have reported similar drop of FF in devices employing large-size and highly concentrated NPs.[14][15][34] By decreasing the concentration of NPs in NBA-60, the higher PCE of 5.81% was achieved with maintaining FF of 0.65, while the J_{SC} (10.24 mA/cm^2) was lowered due to the reduced plasmonic effect by the decreased number of NPs (See Figure 12b and Table 5), which shows good agreement with literatures about the flat interlayers incorporating NPs. [35][36] Consequently, the leakage current arising from the short distance between the cathode and the NBA degrades the device performance in spite of the increased J_{SC} . It is not only observed that the PCE of the device containing the NBA-60 with high volume ratio of NPs to the active layer (0.49%) is lowered than that of one with low concentration (0.27%), but device performances of highly concentrated NBA-20 ($> 0.1\%$) and 40 ($> 0.2\%$) also reduced due to the reduction in J_{SC} as shown in Figure 13. It may be attributed to reduced volume of the active layer arising from the presence of NPs, which augments the leakage current and decreases light harvesting. To analyze the influence of the NP size on the external quantum efficiency (EQE), the IPCEs of devices with the NBA and the reference device including 20 nm MoO_3 HEL without Ag NPs were measured. Figure 12b shows that the IPCE of OPVs with the NBA is higher than that of reference sample, which reflects the enhancement in J_{SC} . The effect of the NBA on these OPVs is investigated systematically by comparing measured IPCE with calculated one in terms of enhancement ratio of devices as illustrated in Figures 12c and d. The results show three unique features in the spectral responses of the device. First of all, the enhancement ratio of measured IPCE increases proportionally to the size of NPs in the spectral range of 400 to 600 nm, consistent with the optical simulation. The highest IPCE enhancement ratio of each device in this wavelength range increases by 21%, 28%, and 30% in NBA-20, 40, and 60, respectively, with respect to the reference one. The enhancements in experimental IPCE are slightly higher than those of the calculated absorption model because an electrical enhancement coming from an enlarged surface area of the

anode with the NBA was not considered in the simulation. Next, the wavelength of the main peak in IPCE enhancement plot, (465 nm for NBA-20, 490 nm for NBA-40, and 520 nm for NBA-60) is red-shifted with increasing the size of NPs. Simulated absorption data follows the IPCE experimental results regardless of slight difference in the distribution between a calculated model and a fabricated architecture. Even though previous studies have predicted similar phenomenon[11], the relationship between the IPCE peak and the NP size enclosed with the metal oxide layer has not been verified experimentally. The experimental finding of the IPCE peak dependency on the incorporated NP size might have been successfully achieved by the low possibility of aggregation among the NPs and the low deviation of NPs' size in the NBA through the evaporation and condensation method based on the dry aerosol process. Lastly, the additional enhancement peak at the red and near infrared (IR) region (650 to 800 nm) is prominent in both the experimental IPCE and calculated absorption enhancement plots (the inset of Figure 12c and d), which is not observed in the calculated scattering CS shown in Figure 3. Interestingly, this improvement shown in the range above 650 nm is much higher than that occurring around at 450 to 600 nm. By comparing the absorption of the active layer with and without Al back reflector throughout the simulation, I found that the multi-reflection between the NBA on the ITO electrode and the Al electrode causes to increase the absorption in low energy light (See Figure 14). But, the absorption of the PCDTBT : PC₇₀BM in this region is so low that this enhancement cannot substantially contribute to photocurrent enhancement. If this NBA is applied to near IR absorbing materials, further improvement in device performance is expected.

2.2.6 *J-V, IPCE, and PL characteristics of devices with different HEL layers*

Furthermore, to identify the difference in the plasmonic effect between the NBA and the conventionally used flat interfacial layers including Ag NPs, devices containing PEDOT:PSS with and without 40 nm of Ag NP were fabricated. The relatively thin PEDOT:PSS (20 nm) was chosen as the HEL for direct comparison with the NBA case. [37] The device structure and all manufacturing procedures except the HEL were exactly the same as those of devices with the NBA. Figure 7a shows the J-V characteristics of devices with different plasmonic structures.

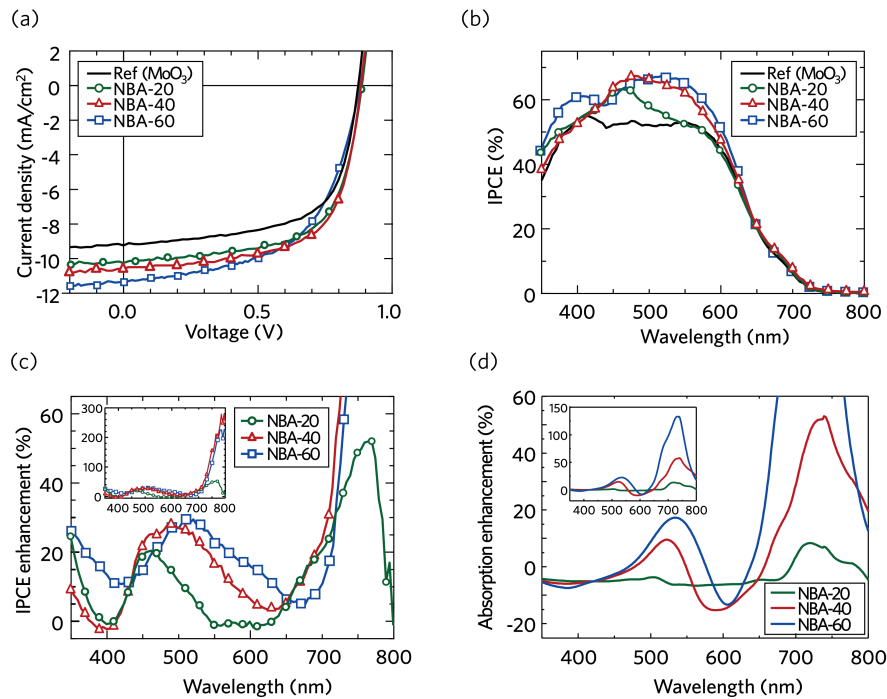


Figure 6: (a) J-V characteristics of the plasmonic OPVs with the NBA incorporating sized NPs (NBA-20, 40, and 60). (b) IPCEs of the OPVs with the NBA. (c) The IPCE enhancement ratio and (d) calculated absorption enhancement ratios of the plasmonic solar cells as a function of wavelength. The inset graphs in (c) and (d) illustrate the enhancement ratio in a full scale.

	J_{SC} (mA/cm ²)	V_{OC} (V)	FF	Efficiency (%)	R_{SH} (k Ω .cm ²)
Ref	9.12 \pm 0.10 (9.16)	0.88 \pm 0.01 (0.88)	0.64 \pm 0.01 (0.64)	5.07 \pm 0.08 (5.16)	2.0
NBA-20	10.04 \pm 0.09 (10.15)	0.88 \pm 0.01 (0.88)	0.64 \pm 0.01 (0.65)	5.62 \pm 0.15 (5.80)	2.1
NBA-40	10.43 \pm 0.12 (10.58)	0.88 \pm 0.01 (0.88)	0.64 \pm 0.01 (0.65)	5.87 \pm 0.17 (6.07)	2.4
NBA-60	11.11 \pm 0.24 (11.36)	0.87 \pm 0.01 (0.88)	0.55 \pm 0.02 (0.57)	5.37 \pm 0.26 (5.65)	0.4

Table 2: Device performance of the plasmonic solar cells containing the NBA with differently sized NPs^a

^a The average and standard deviation values of the photovoltaic parameters are shown. The values inside parentheses represent the parameters of OPVs with the highest PCE for each case.

	Exciton generation rate (/m ³ s ¹)	Enhancement ratio
Ref	5.59 $\times 10^{27}$	-
NBA-20	6.07 $\times 10^{27}$	8.8%
NBA-40	6.42 $\times 10^{27}$	14.8%
NBA-60	6.90 $\times 10^{27}$	23.4%

Table 3: Exciton generation rate and its enhancement for the devices with NBA and reference sample with 20 nm of MoO₃ HEL

The PCE of the device with FP-40 (5.67%) is improved compared to its counterpart without Ag NPs (5.20%). As the flat PEDOT:PSS is replaced with the NBA structure as a HEL, the PCE of the NBA-40 further increases to 6.07% because of the enhancement in J_{SC} from 10.24 mA/cm² to 10.58 mA/cm². It should be noted that the device performance of the samples without Ag NPs is very similar to each other regardless of HEL types (Table 3). These results of device performance demonstrate that the NBA structure more significantly influences on the photovoltaic characteristic compared to the device with the same sized NPs embedded in the flat PEDOT:PSS. The enhancement in J_{SC} can be attributed to the higher exciton generation of the device assisted by the NBA because of its excellent optical effects: the LSPR and near field analysis. The effects of different optical properties caused by each plasmonic structure on device performance are reflected in the IPCE of two devices as illustrated in Figure 7b. The increase in J_{SC} of the NBA-40 is mainly caused by the increased EQE at the wavelength of 450 – 600 nm, while the IPCE of FP-40 is outstandingly improved at a short wavelength (~ 350 nm), similar to the previous reports on the devices embedding Ag NPs in PEDOT:PSS layer. [5] This results are coincided with the simulated result on the scattering CS (Figure 3c) and the UV-visible light absorption spectra of the PCDTBT:PC₇₀BM films casted on the both MoO₃ and PEDOT:PSS with Ag NP (See Figure 11). Therefore, it is obvious that the enhanced scattering intensity near the green light with a strong forward direction via the combination of the NBA and the undulated active layer makes the photocurrent of device higher compared to the case with flat buffer layers.

In addition, the steady-state PL of the spin-casted PCDTBT films with NBA-40 and FP-40 is a supportive evidence to show better optical properties of the NBA. Figure 7c represents that the PL intensity of the NBA-40 is broadly enhanced compared to that of the FP-40. Commonly, the steady-state PL intensity is generally determined by two factors: the resonance frequency overlap between the absorption band gap of polymer and the nanostructure induced plasmonic effects, as well as the decay of photo-generated excitons. [38] The aforementioned simulation and measured results already reveal that the superior optical properties of the NBA contribute to the change of steady-state PL. However, the difference in the steady-state PL between the NBA-40 and FP-40 is bigger than that of J_{SC} for each corresponding device. To distinguish the op-

HEL layer	Ag NPs	J_{SC} (mA/cm ²)	V_{OC} (V)	FF	Efficiency (%)
NBA	None	9.12 ± 0.10 (9.16)	0.88 ± 0.01 (0.88)	0.64 ± 0.01 (0.64)	5.07 ± 0.08 (5.16)
	NBA-40	10.43 ± 0.12 (10.58)	0.88 ± 0.01 (0.88)	0.64 ± 0.01 (0.65)	5.87 ± 0.17 (6.07)
Flat PEDOT:PSS	None	9.18 ± 0.10 (9.19)	0.89 ± 0.01 (0.89)	0.62 ± 0.01 (0.63)	5.08 ± 0.11 (5.20)
	FP-40	10.10 ± 0.12 (10.24)	0.89 ± 0.01 (0.89)	0.61 ± 0.01 (0.62)	5.57 ± 0.06 (5.63)

Table 4: Comparison of device performance for the NBA-40 and the FP-40.^a

^a The average and standard deviation values of the photovoltaic parameters are shown. The values inside parentheses represent the parameters of OPVs with the highest PCE for each case.

tical and electrical effect of different plasmonic buffer layers, transient PLs of both films were measured at the wavelength of 690 nm (Figure 7d) and decay times of films on each buffer were estimated by using exponential function.¹⁷ In the films with FP-40, the short exciton lifetime (478 ± 28 ps) is observed, whereas the lifetime of NBA-40 (575 ± 25 ps) is similar to that of film without NPs (See Figure 9b). Generally, the fast decay of exciton is related to high recombination losses and exciton quenching.^[17, 26] Moreover, it is well known that the direct contact between metal NPs and polymer layers can be a source of the exciton quenching.^{[38][39]} As a result, the NBA, which has Ag NPs fully covered by the thermally evaporated MoO₃, prevents the device from recombination losses, while the exciton quenching can occur at partially disclosed Ag NPs placed in the flat PEDOT : PSS. Therefore, the NBA does not only enhance device performance due to its superior optical properties, but also has low recombination losses arising from isolation of the NPs from the active layer without any degradation of the enhanced optical properties. Consequently, it is apparent that the NBA induced plasmonic effect and light scattering are higher than those from the conventional structure.

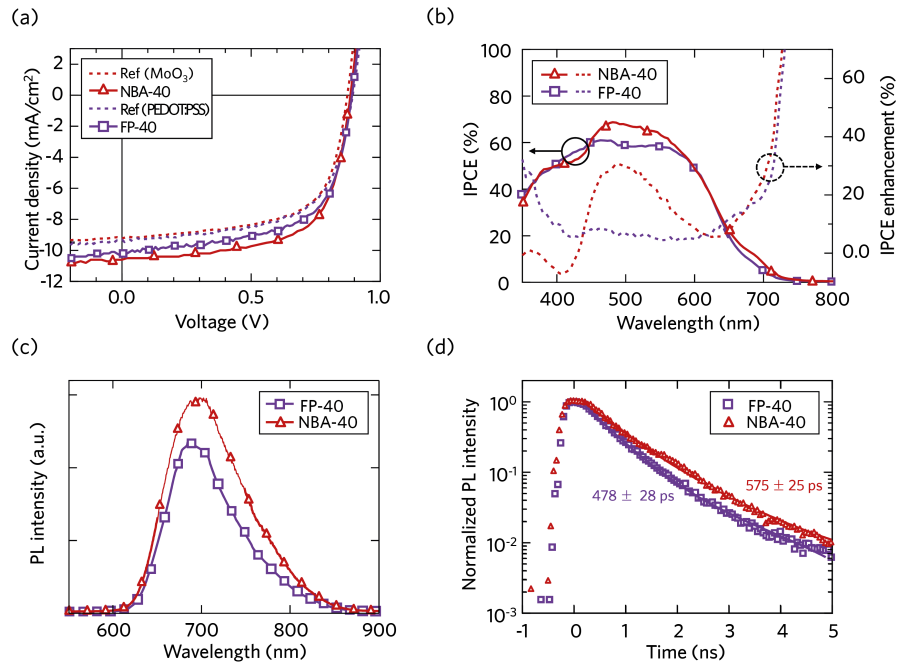


Figure 7: (a) The J-V characteristics of devices with different HEL layers. The solid lines denote the devices with Ag 40, while the dash lines represent the devices without Ag NP. (b) The IPCE data and their enhancement ratios compared to each reference sample (c) Steady-state PL spectra of PCDTBT films with different buffer layers (d) Time resolved PL ($\lambda = 690$ nm) of PCDTBT films with the NBA-40 compared to the FP-40, where the numbers represent the exciton lifetime inside each active material. Here, the measured data (symbols) are fitted using exponential functions (solid lines).

2.2.7 TEM analysis and EDS mapping data for the NBA with different sizes of Ag NP

Scanning-transmission electron microscopy (S-TEM) images of devices with the NBA shown in Figure 8a-c have revealed that the 20 nm thick MoO₃ bumps are uniformly deposited over Ag 20, 40, and 60 on the ITO surface and well follow the underlying structure of Ag NPs. To identify the spatial distribution of the NBA, I mapped the distribution of Ag and Mo elements using the EDS analysis for the rectangular area of S-TEM images denoted by violet lines. In some cases of Ag 60, the lower parts of Ag NPs are barely covered with MoO₃ coming from the inherent feature of thermal deposition equipment, because the size of NP is relatively larger than the 20 nm thickness of MoO₃ layer.

2.2.8 Steady-state and time resolved PL of PCDTBT layer on the NBA structure

To verify the enhanced absorption inside the polymer layer arising from the nanostructure induced plasmonic peak, photoluminescences (PL) of PCDTBT casted on the NBA with differently sized NPs (20, 40, 60 nm) were measured. As shown in Figure 9a, PL intensities of all the samples containing Ag NPs, excited by 405 nm laser diode, are higher than that of its counterpart without NPs. Since PL intensity typically reflects the resonance spectral overlap between the absorption band and the induced plasmonic wavelength, these results indicate that the absorption of polymer layer increases due to the NBA induced plasmonic effect. Thus, the light absorption inside the polymer with the NBA can be enhanced. In addition, the PL intensity is proportional to the NP size. This may be ascribed that higher scattering CS ratio in the NPs with larger size allows better optical enhancement in the polymer layer, resulting in increasing the J_{SC} of devices. Next, Figure 9b illustrates time resolved PL of the active layer to compare exciton lifetime at the wavelength of 690 nm. The laser diode ($\lambda = 405$ nm) was used as an excitation light source and the resolution of measurement was 55 ps. Exciton lifetimes for all the samples deduced from exponential function [17] are similar to each other regardless of the existence of NPs and their sizes. Since the steady-state PL is influenced not only by optical effect, but also by the decay of exciton, the increase in the steady-state PL is mostly caused

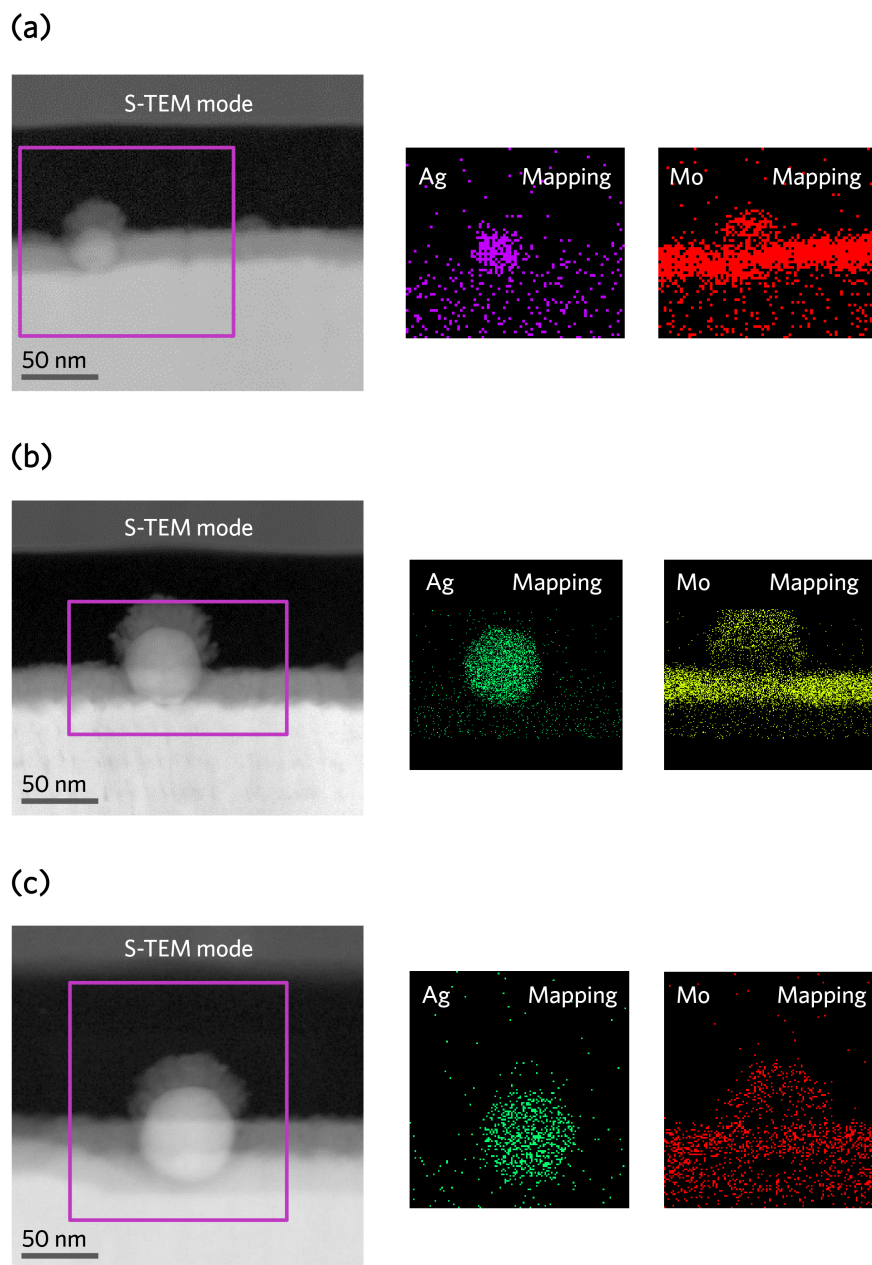


Figure 8: Cross-sectional S-TEM images and their EDS analysis to confirm the morphology and existence of the NBA embedding (a) Ag 20, (b) 40, and (c) 60.

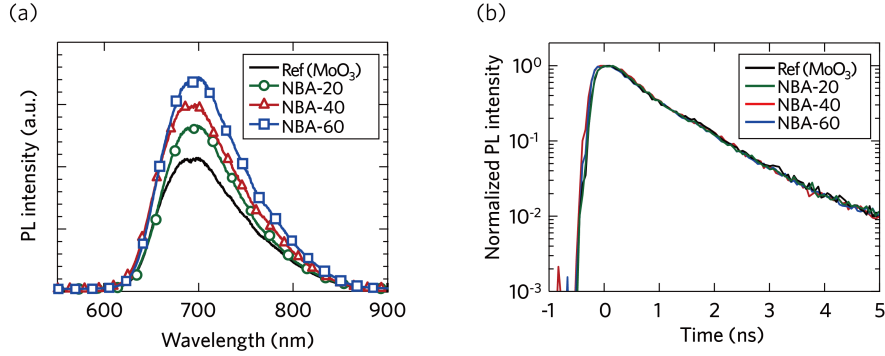


Figure 9: (a) Steady-state PL spectra and (b) transient PL of PCDTBT (80 nm) films with and without the NBA. The sizes of NPs for NBA are 20, 40, and 60 nm.

by the superior absorption properties in the active layer induced by the NBA. Meanwhile, previous researches reported that if the NPs were not fully isolated from the active layer, the exciton lifetime would decrease because they act as exciton quenching sites or recombination centers. [38][25] Since the lifetimes of the films incorporating even larger sized NPs are the same as that of the film without NPs, I believe that Ag NPs up to 60 nm are fully covered with 20 nm thermally evaporated MoO₃.

2.2.9 Exciton generation rate of the OPVs with and without Ag NPs

For exploring the plasmonic effects in devices, I derived the maximum exciton generation rate (G_{MAX}). Figure 10 illustrates the dependence of the photocurrent density (J_{ph}) on the effective voltage (V_{eff}) for devices with and without Ag NPs. Here J_{ph} and V_{eff} are given by the following equations, $J_{ph} = J_L - J_D$, $V_{eff} = V_o - V_a$ where J_L (J_D) are the current densities under illumination (in the dark), V_o is the voltage when the J_{ph} is zero, and V_a is the applied voltage. According to previous reports, [40] G_{MAX} can be expressed as a function of the thickness of device and saturated photocurrent, $J_{sat} = q G_{MAX} L$ where q represents a charge amount of single electron, L the device thickness, and J_{sat} saturated photocurrent. J_{sat} was derived from the J_{ph} in the high reverse voltage. [40] The deduced exciton generation rate, shown in Table 5, increases as the size of incorporated Ag NP increases, which shows the same trend with the J_{SC} enhancement in devices employing the NBA.

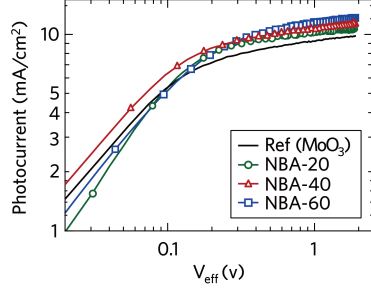


Figure 10: Photocurrent density (J_{ph}) versus effective voltage characteristics of the OPVs incorporating Ag NPs with different diameters.

	Volume concentration (%)	Best				
		J_{SC} (mA/cm ²)	V_{OC} (V)	FF	Efficiency (%)	R_{SH} (k Ω .cm ²)
Ref	-	9.16	0.88	0.64	5.16	2.0
NBA-60	0.27	10.24 (11.8%)	0.88	0.65	5.81 (12.6%)	1.0
	0.49	11.36 (24.0%)	0.88	0.57	5.65 (9.5%)	0.4

	Volume concentration (%)	Best			
		J_{SC} (mA/cm ²)	V_{OC} (V)	FF	Efficiency (%)
Ref	-	9.12 ± 0.10	0.88 ± 0.01	0.64 ± 0.01	5.07 ± 0.08
NBA-60	0.27	10.25 ± 0.07 (12.4%)	0.87 ± 0.01	0.64 ± 0.01	5.67 ± 0.15 (11.8%)
	0.49	11.11 ± 0.25 (21.8%)	0.87 ± 0.01	0.55 ± 0.02	5.37 ± 0.28 (5.9%)

Table 5: Device performance of the NBA-60 with different concentrations. The values inside parenthesis represent the amounts of increase in percentage with respect to that of the reference cell without NPs.

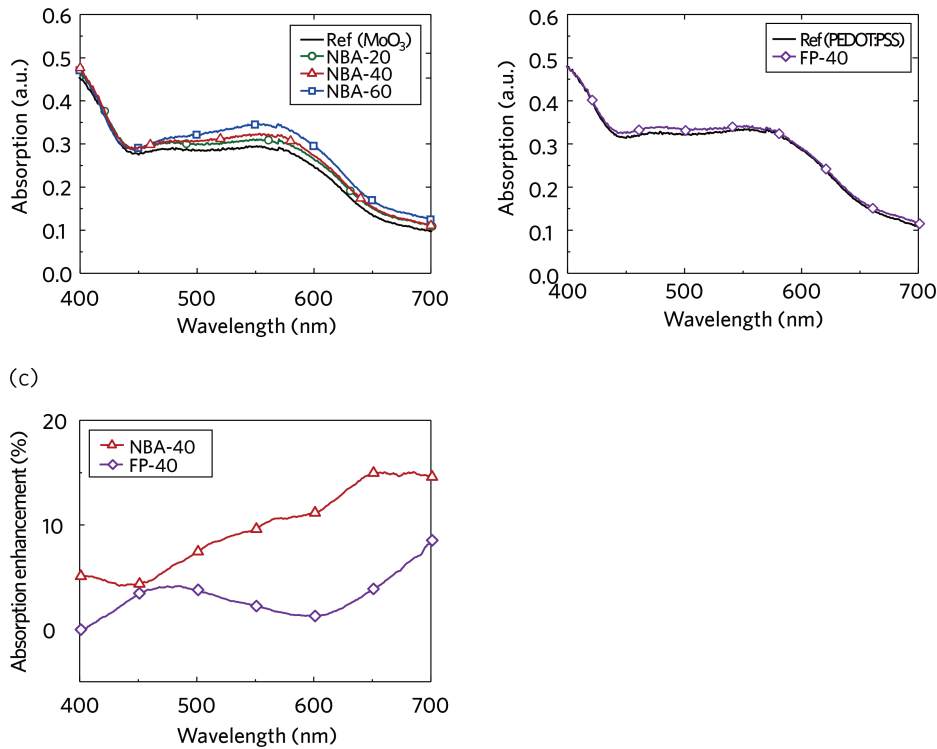


Figure 11: Absorption spectra of PCDTBT : PC₇₀BM (a) with and without the NBA structure containing various sizes of NPs, and (b) with and without 40 nm Ag NPs inside PEDOT : PSS. (c) The absorption enhancement of the NBA-40 and the FP-40 with respect to each reference sample.

2.2.10 Absorption enhancement of PCDTBT : PC₇₀BM with and without the NBA

UV-visible absorption spectra of various polymer solar cells are shown in In Figure 11. The absorption spectra of PCDTBT : PC₇₀BM polymer cells with and without the NBA structure containing various sizes of Ag NPs are represented in Figure 11 (a).

The absorption spectra of PCDTBT : PC₇₀BM polymer cells with and without 40 nm Ag NPs inside PEDOT : PSS are shown in Figure 11 (b). The absorption enhancement of the NBA-40 and the FP-40 with respect to each reference sample depicted in Figure 11 (c).

2.2.11 *J-V characteristics of the OPVs with different concentrations and sizes*

In order to explore the cause of the low FF, the J-V characteristics under dark condition were analyzed. I have observed that the dark current density of the NBA-60 at the reverse bias voltage (-1 V) is higher by two orders of magnitude than those of the other devices (Figure 12a). Moreover, its shunt resistance (R_{SH}), deduced from the slope at the J_{SC} , is approximately one-fifth of R_{SH} value of the others. This means that the reduction of FF is mainly caused by the increased leakage current and the recombination losses in the NBA-60. Next, I present the J-V characteristics of the NBA-60 with different volume concentrations in dark state along with the case under illumination (Figure 12b and c). Here, the volume concentration was derived using the ratio of the occupied space of Ag NPs in average to the volume of the active layer. The device performances of the NBA-60 with different volume concentrations (low and high) are also summarized in Table 5. The results show that the more Ag 60 is located on the ITO surface, the higher J_{SC} is obtained with reducing the FF. As the active layer was only 20 - 30 nm thicker than the size of Ag 60 (Figure 12d), the possibility for leakage current and recombination losses might increase in highly concentrated NBA-60. This is supported by the measured dark current density of the NBA-60 at -1 V and its shunt resistance estimated from the slope at the J_{SC} . Hence, I could identify that the devices employing Ag 60 with high concentration result in the reduction of FF, which is not favorable for further improvement of the device performance.

2.2.12 *Device parameters of OPV embedding the NBA with different volume concentrations*

Figure 13 shows the relationship between the volume concentration of NPs and the device performance with them. Note that the volume concentration was defined by using the ratio of the occupied space of Ag NPs in average to the volume of the active layer. The PCEs of all the samples show parabolic curves with the maximum points at the volume concentration of around 0.1 to 0.25%. When the volume concentration is lower than the optimal one, the J_{SC} decreases due to low plasmonic effect. In addition, the J_{SC} generally decrease in the devices incorporating metal NPs with higher concentration than the optimal one because

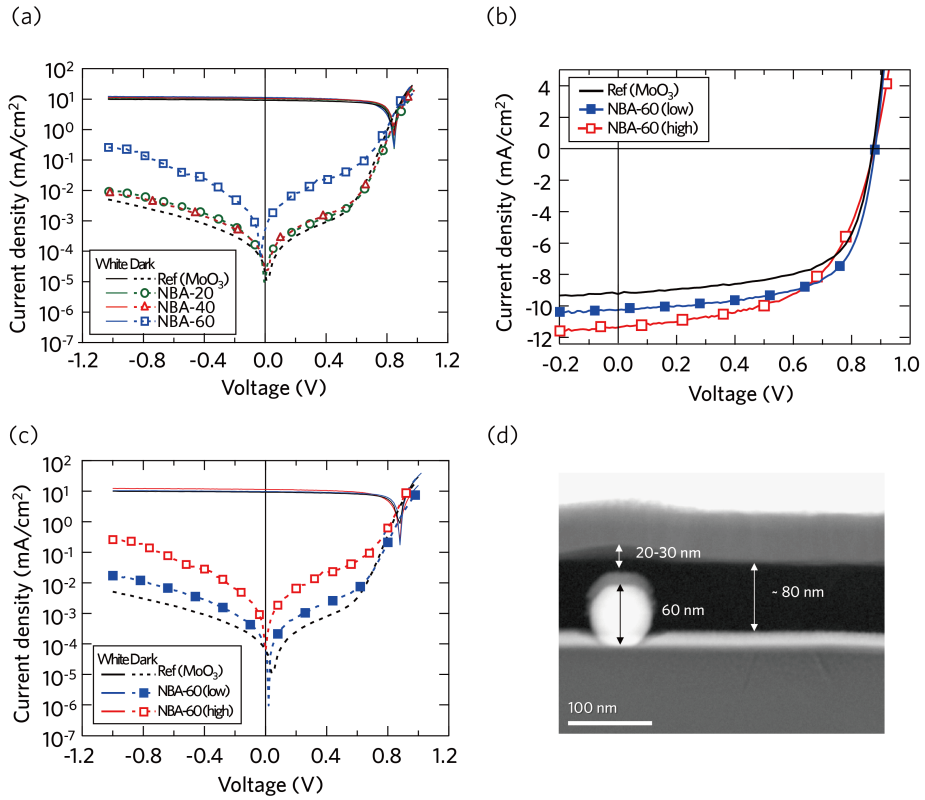


Figure 12: (a) The analysis of J-V characteristics for the OPVs with differently sized Ag-NPs under dark condition and white illumination of AM 1.5G 100 mW/cm² J-V characteristics of the OPVs with different concentrations of Ag 60 and without NPs, (b) under illumination, and (c) dark condition. (d) The representative S-TEM image of the NBA-60.

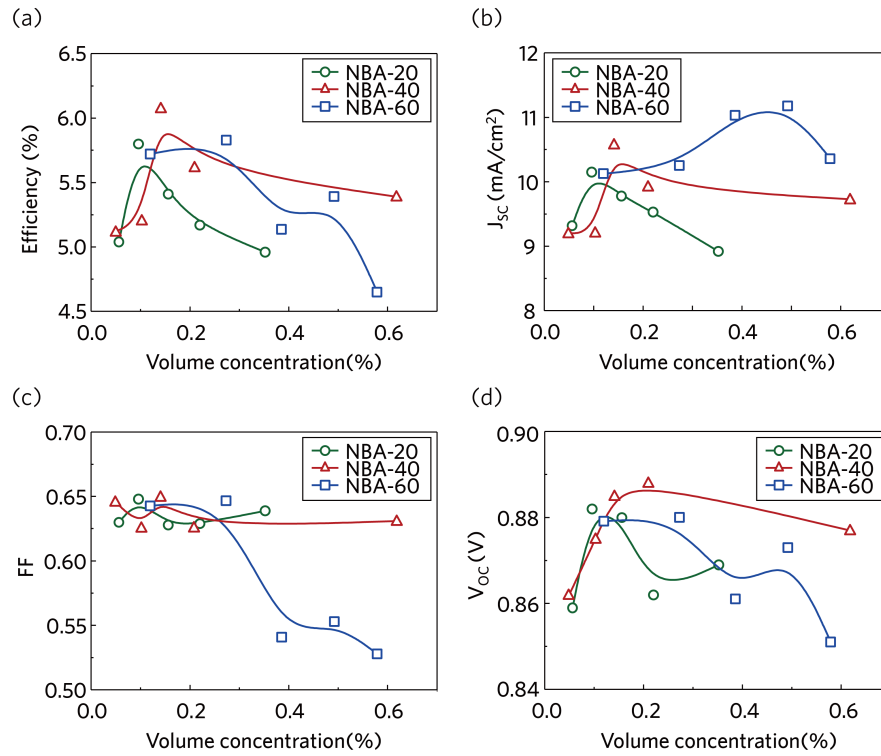


Figure 13: Device performance parameters: (a) Efficiency, (b) J_{SC} , (c) FF, and (d) V_{OC} of the NBA-20, 40, and 60, as a function of volume concentration under illumination.

of the followings: the incident light blocking by NPs themselves, the reduced volume of active layer, and high leakage current. In the case of NBA-60, the J_{SC} is continuously enhanced when the volume concentration is beyond the optimal point, where the enhanced J_{SC} is overwhelmed by the leakage current, resulting in reduced V_{OC} and FF as demonstrated in Figure 13c and d.

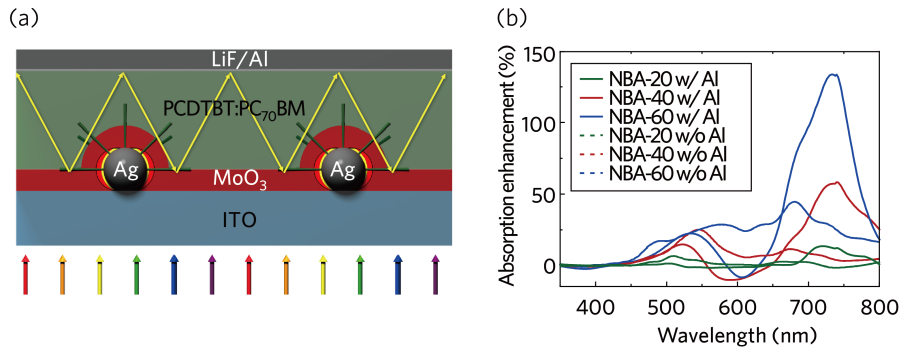


Figure 14: (a) Schematic of light trapping and multi-reflection by the excitation of LSPR and scattering of the devices with the NBA, (b) calculated absorption enhancement versus wavelength for Ag NPs incorporated devices with the Al electrode (solid line) and without the one (dash line).

2.2.13 Multi-reflection effect with and without Al cathode within plasmonic OPV cells

2.3 EXPERIMENT AND METHOD

2.3.1 3D FDTD simulation for CS and IPCE enhancement

I set the incident light source (300 – 800 nm in wavelength) propagating in z-direction with TE polarization (or horizontal polarization), and used symmetric boundary conditions for x,y- axes and perfectly matched layer (PML) condition for z-axis. I selected total field scatter field (TFSF) light source to the FDTD model. The absorption CS and the scattering CS were calculated by a total field (incident field + scattered field) power monitor and a scattered field power monitor. Using these power monitors, power flows induced by the interaction of the incident wave and a particle scatterer were estimated. Dispersive complex refractive indices (n, k) for PEDOT : PSS, MoO₃, and PCDTBT : PC₇₀BM measured by spectroscopic ellipsometer (M2000D, Woollam) were adopted in to the simulation model. It was assumed that both Ag NPs and the NBA were concentric spheres and Ag NPs were point-contacted onto the ITO-coated glass. Also, the ITO and Al electrodes were excluded so as to consider only the scattering effect by plasmonic NPs neglecting multi-reflection phenomena between the two electrodes. I also imposed

an average interdistance of 200 nm on Ag 20, 40, and 60 from the particle analysis of the SEM images. The thickness for the PEDOT : PSS and MoO₃ layers on the ITO-coated glass substrate was fixed at 20 nm to reproduce real device structure. Finally, the calculated absorption enhancement is compared with the experimental IPCE enhancement. The actual structure of plasmonic OPV was modeled by considering the measured thickness of the device with and without NPs. The plane wave source under AM 1.5G illumination was imposed on the model and the rest of boundary conditions were the same as the near field CS simulations. By inserting power monitor into the model, the absorption enhancement within plasmonic architecture was extracted.

2.3.2 *Device fabrication and electro-optical measurement*

The devices were fabricated on ITO-coated glass substrates with a sheet resistance of 20 Ω/cm^2 . The ITO patterned substrates were pre-cleaned with acetone for 15 min and isopropyl alcohol for 15 min and were dried in a vacuum oven. And then, the ITO-coated glasses were treated with UV-ozone. The various sizes of silver NPs were deposited on the ITO using the evaporation and condensation method in the nitrogen globe box. Afterwards, the mixture of the PCDTBT : PC₇₀BM in dichlorobenzene (1:4 weight ratio, 20 mg/mL) was spin-casted at 600 rpm for 60 s on top of the MoO₃ layer of 20 nm thickness by thermal evaporation process to construct nanobump arrays and was annealed at a high vacuum ($<10^{-6}$ Torr) chamber for two hours. The active layer was 80 - 90 nm in thickness. Finally, the device fabrication was completed by thermal evaporation of 0.5 nm LiF for electron extraction layer and 100 nm Al as the cathode through shadow masks under high vacuum chamber. For comparison, the reference device without Ag NPs was also fabricated. And the films without LiF and the cathode electrode for UV-visible absorption spectra and the ones substituting the active layer with 80 nm PCDTBT for PL measurement were fabricated as well. The J-V characteristics were measured by using a Keithley 237 source measurement unit under AM 1.5G illumination condition at an intensity of 100 mW/cm² with an Oriel So13ATM solar simulator. IPCE spectra of devices were obtained using Oriel IQE 200 model, which combined monochromator and lock-in amplifier by comparison to a calibrated silicon photodiode. The J-V feature and IPCE measurement procedures

were performed in the nitrogen glove box to prevent the device degradations. For UV-visible spectroscopy measurement, the Cary 5000 UV-Vis-NIR spectrophotometer (Agilent Technologies) with integrating sphere system was used. On the other hand, the steady-state and time resolved PL excited by 405 nm laser diode were recorded using iHR320 (Horiba, Ltd.).

2.4 CONCLUSIONS

I have demonstrated a considerable enhancement both in J_{SC} and PCE of the plasmonic PCDTBT : PC₇₀BM solar cells employing the NBA composed of MoO₃ layer and Ag NPs under the active layer, compared to the reference devices including MoO₃ HEL without NPs. Here, the NPs with different diameters (Ag 20, 40, and 60) have been generated by the evaporation and condensation method using the aerosol process in dry environment without aggregation, impurity, and contamination issues that can usually happen in the wet synthesis. FDTD calculation results on scattering cross-sections and near field profiles inside the active materials show higher intensities with a strong forward scattering effect in the devices with the NBA than those with the flat PEDOT : PSS. J-V characteristics show that J_{SC} increases continuously as the size of NPs increases and the best performance is achieved at the device embedding NBA-40. The improved performance depending on the size of NPs is explained by the strong forward light scattering effect coming from near-field enhancement in the vicinity of Ag NP in the visible region, as well as the multi-reflection between the cathode and the nanobumped anode in the near IR region. Furthermore, I have presented that the OPVs containing the NBA show better performance than those with PEDOT : PSS incorporating NPs due to smaller recombination losses and higher absorption intensity. Therefore, this approach can be a promising platform for efficient light harnessing in a broad spectral range for use in diverse OPV devices.

BIBLIOGRAPHY

- [1] G. Yu, J. Gao, J. C. Hummelen, F. Wudl, and A. J. Heeger. Polymer photovoltaic cells: Enhanced efficiencies via a network of internal donor-acceptor heterojunctions. *Science*, 270(5243):1789–1791, December 1995. (Cited on page 12.)
- [2] Gang Li, Rui Zhu, and Yang Yang. Polymer solar cells. *Nat. photonics*, 6(3):153–161, 2012. (Cited on page 12.)
- [3] Yuhki Terao, Hiroyuki Sasabe, and Chihaya Adachi. Correlation of hole mobility, exciton diffusion length, and solar cell characteristics in phthalocyanine/fullerene organic solar cells. *Appl. Phys. Lett.*, 90(10):103515, March 2007. (Cited on page 12.)
- [4] Qiaoqiang Gan, Filbert J. Bartoli, and Zakya H. Kafafi. Plasmonic-enhanced organic photovoltaics: Breaking the 10% efficiency barrier. *Adv. Mater.*, page n/a–n/a, 2013. (Cited on page 12.)
- [5] Luyao Lu, Zhiqiang Luo, Tao Xu, and Luping Yu. Cooperative plasmonic effect of ag and au nanoparticles on enhancing performance of polymer solar cells. *Nano Lett.*, 13(1):59–64, January 2013. (Cited on pages 12, 13, and 29.)
- [6] Jun Yang, Jingbi You, Chun-Chao Chen, Wan-Ching Hsu, Hai-ren Tan, Xing Wang Zhang, Ziruo Hong, and Yang Yang. Plasmonic polymer tandem solar cell. *ACS Nano*, 5(8):6210–6217, 2011. (Cited on page 12.)
- [7] Dong Hwan Wang, Do Youb Kim, Kyeong Woo Choi, Jung Hwa Seo, Sang Hyuk Im, Jong Hyeok Park, O Ok Park, and Alan J. Heeger. Enhancement of Donor–Acceptor polymer bulk heterojunction solar cell power conversion efficiencies by addition of au nanoparticles. *Angew. Chem. Int. Ed.*, 50(24):5519–5523, 2011. (Cited on page 12.)
- [8] Bo Wu, Than Zaw Oo, Xianglin Li, Xinfeng Liu, Xiangyang Wu, Edwin Kok Lee Yeow, Hong Jin Fan, Nripan Mathews, and Tze Chien

- Sum. Efficiency enhancement in bulk-heterojunction solar cells integrated with large-area ag nanotriangle arrays. *J. Phys. Chem. C*, 116(28):14820–14825, 2012. (Cited on page 12.)
- [9] Yu-Sheng Hsiao, Shobhit Charan, Feng-Yu Wu, Fan-Ching Chien, Chih-Wei Chu, Peilin Chen, and Fang-Chung Chen. Improving the light trapping efficiency of plasmonic polymer solar cells through photon management. *J. Phys. Chem. C*, 116(39):20731–20737, 2012. (Cited on page 12.)
- [10] Chuan-Sheng Kao, Fang-Chung Chen, Ching-Wen Liao, Michael H. Huang, and Chain-Shu Hsu. Plasmonic-enhanced performance for polymer solar cells prepared with inverted structures. *Appl. Phys. Lett.*, 101(19):193902–193902–4, November 2012. (Cited on page 12.)
- [11] Xi Yang, Chu-Chen Chueh, Chang-Zhi Li, Hin-Lap Yip, Peipei Yin, Hongzheng Chen, Wen-Chang Chen, and Alex K-Y. Jen. High-efficiency polymer solar cells achieved by doping plasmonic metallic nanoparticles into dual charge selecting interfacial layers to enhance light trapping. *Adv. Energy Mater.*, page n/a–n/a, 2013. (Cited on pages 12 and 26.)
- [12] Harry A. Atwater and Albert Polman. Plasmonics for improved photovoltaic devices. *Nat. Mater.*, 9(3):205–213, March 2010. (Cited on pages 12, 20, and 52.)
- [13] Di Qu, Fang Liu, Yidong Huang, Wanlu Xie, and Qi Xu. Mechanism of optical absorption enhancement in thin film organic solar cells with plasmonic metal nanoparticles. *Opt. Express*, 19(24):24795–24803, 2011. (Cited on page 12.)
- [14] George D. Spyropoulos, Minas M. Stylianakis, Emmanuel Stratakis, and Emmanuel Kymakis. Organic bulk heterojunction photovoltaic devices with surfactant-free au nanoparticles embedded in the active layer. *Appl. Phys. Lett.*, 100(21):213904, May 2012. (Cited on pages 12 and 25.)
- [15] Mei Xue, Lu Li, Bertrand J. Tremolet de Villers, Huajun Shen, Jinfeng Zhu, Zhibin Yu, Adam Z. Stieg, Qibing Pei, Benjamin J. Schwartz, and Kang L. Wang. Charge-carrier dynamics in hybrid plasmonic organic solar cells with ag nanoparticles. *Appl. Phys. Lett.*, 4(6):119–119, June 2011. (Cited on pages 12 and 25.)

- [16] N. Kalfagiannis, P.G. Karagiannidis, C. Pitsalidis, N.T. Panagiotopoulos, C. Gravalidis, S. Kassavetis, P. Patsalas, and S. Logothetidis. Plasmonic silver nanoparticles for improved organic solar cells. *Sol. Energy Mater. Sol. cells*, 104(0):165–174, 2012. (Cited on page 13.)
- [17] Jyh-Lih Wu, Fang-Chung Chen, Yu-Sheng Hsiao, Fan-Ching Chien, Peilin Chen, Chun-Hong Kuo, Michael H. Huang, and Chain-Shu Hsu. Surface plasmonic effects of metallic nanoparticles on the performance of polymer bulk heterojunction solar cells. *ACS Nano*, 5(2):959–967, 2011. (Cited on pages 13, 30, and 32.)
- [18] Jian Ye, Niels Verellen, Willem Van Roy, Liesbet Lagae, Guido Maes, Gustaaf Borghs, and Pol Van Dorpe. Plasmonic modes of metallic semishells in a polymer film. *ACS Nano*, 4(3):1457–1464, 2010. (Cited on page 13.)
- [19] Yanming Sun, Christopher J. Takacs, Sarah R. Cowan, Jung Hwa Seo, Xiong Gong, Anshuman Roy, and Alan J. Heeger. Efficient, air-stable bulk heterojunction polymer solar cells using MoO_x as the anode interfacial layer. *Adv. Mater.*, 23(19):2226–2230, 2011. (Cited on page 13.)
- [20] Kenji Kawano, Roberto Pacios, Dmitry Poplavskyy, Jenny Nelson, Donal D.C. Bradley, and James R. Durrant. Degradation of organic solar cells due to air exposure. *Sol. Energy Mater. Sol. Cells*, 90(20):3520–3530, 2006. (Cited on page 13.)
- [21] Vishal Shrotriya, Gang Li, Yan Yao, Chih-Wei Chu, and Yang Yang. Transition metal oxides as the buffer layer for polymer photovoltaic cells. *Appl. Phys. Lett.*, 88(7):073508, February 2006. (Cited on page 13.)
- [22] Seungchan Han, Won Suk Shin, Myungsoo Seo, Dipti Gupta, Sang-Jin Moon, and Seunghyup Yoo. Improving performance of organic solar cells using amorphous tungsten oxides as an interfacial buffer layer on transparent anodes. *Org. Electron.*, 10(5):791–797, 2009. (Cited on page 13.)
- [23] Michael D. Irwin, D. Bruce Buchholz, Alexander W. Hains, Robert P. H. Chang, and Tobin J. Marks. p-type semiconducting nickel

- oxide as an efficiency-enhancing anode interfacial layer in polymer bulk-heterojunction solar cells. *PNAS*, 105(8):2783–2787, February 2008. PMID: 18287067. (Cited on page 13.)
- [24] Do Young Kim, Jegadesan Subbiah, Galileo Sarasqueta, Franky So, Huanjun Ding, Irfan, and Yongli Gao. The effect of molybdenum oxide interlayer on organic photovoltaic cells. *Appl. Phys. Lett.*, 95(9):093304, September 2009. (Cited on page 13.)
- [25] Pan-Pan Cheng, Guo-Fu Ma, Jian Li, Yan Xiao, Zai-Quan Xu, Guo-Qiang Fan, Yan-Qing Li, Shuit-Tong Lee, and Jian-Xin Tang. Plasmonic backscattering enhancement for inverted polymer solar cells. *J. Mater. Chem.*, 22(42):22781–22787, October 2012. (Cited on pages 13 and 34.)
- [26] Pan-Pan Cheng, Lei Zhou, Jie-Ai Li, Yan-Qing Li, Shuit-Tong Lee, and Jian-Xin Tang. Light trapping enhancement of inverted polymer solar cells with a nanostructured scattering rear electrode. *Organic Electronics*, 14(9):2158–2163, 2013. (Cited on pages 13 and 30.)
- [27] Xinchun Li, Wallace C. H. Choy, Fengxian Xie, Shaoqing Zhang, and Jianhui Hou. Room-temperature solution-processed molybdenum oxide as a hole transport layer with ag nanoparticles for highly efficient inverted organic solar cells. *J. Mater. Chem. A*, 1(22):6614–6621, May 2013. (Cited on page 13.)
- [28] Dong Hwan Wang, Jason Seifert, Jong Hyeok Park, Dae-Geun Choi, and Alan J. Heeger. Efficiency increase in flexible bulk heterojunction solar cells with a nano-patterned indium zinc oxide anode. *Adv. Energy Mater.*, 2(11):1319–1322, 2012. (Cited on page 14.)
- [29] H.G. Scheibel and J. Porstendorfer. Generation of monodisperse ag- and NaCl-aerosols with particle diameters between 2 and 300 nm. *J. Aerosol Sci.*, 14(2):113–126, 1983. (Cited on page 14.)
- [30] Martin H. Magnusson, Knut Deppert, Jan-Olle Malm, Jan-Olov Bovin, and Lars Samuelson. Gold nanoparticles: Production, reshaping, and thermal charging. *J. Nanopart. Res.*, 1(2):243–251, June 1999. (Cited on page 14.)
- [31] Jae Hee Jung, Hyun Cheol Oh, Hyung Soo Noh, Jun Ho Ji, and Sang Soo Kim. Metal nanoparticle generation using a small ce-

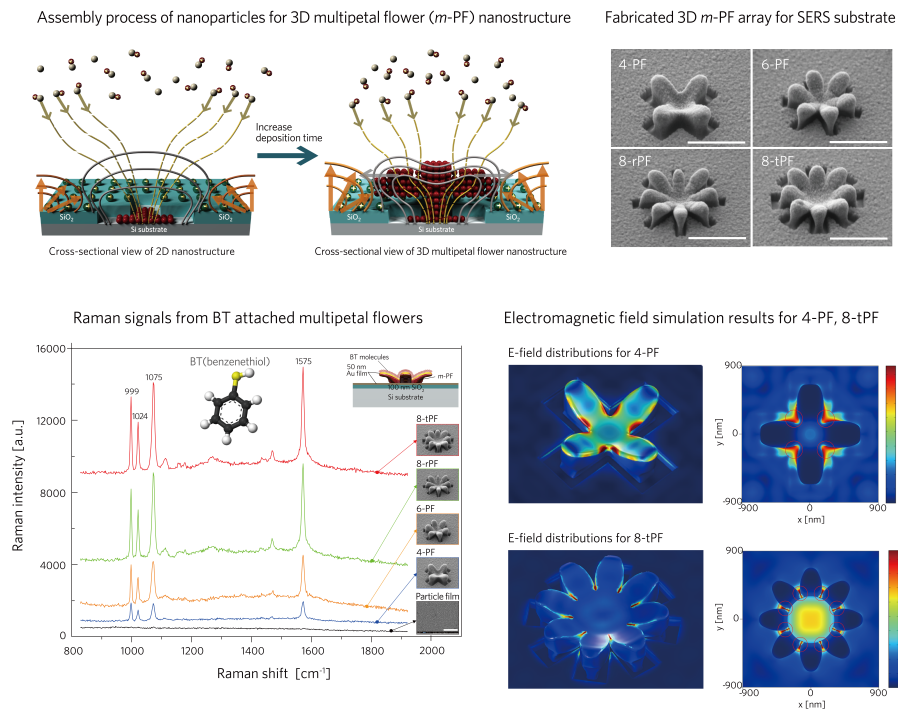
- ramic heater with a local heating area. *J. Aerosol Sci.*, 37(12):1662–1670, 2006. (Cited on page 14.)
- [32] Seunguk Noh, C.K. Suman, Donggu Lee, Seohee Kim, and Changhee Lee. Study of buffer layer thickness on bulk heterojunction solar cell. *Journal of Nanoscience and Nanotechnology*, 10(10):6815–6818, 2010. (Cited on page 15.)
- [33] Boyuan Qi and Jizheng Wang. Fill factor in organic solar cells. *Phys. Chem. Chem. Phys.*, 15(23):8972–8982, May 2013. (Cited on page 25.)
- [34] Ji Hwang Lee, Jong Hwan Park, Jong Soo Kim, Dong Yun Lee, and Kilwon Cho. High efficiency polymer solar cells with wet deposited plasmonic gold nanodots. *Org. Electron.*, 10(3):416–420, 2009. (Cited on page 25.)
- [35] Se-Woong Baek, Jonghyeon Noh, Chun-Ho Lee, BongSoo Kim, Min-Kyo Seo, and Jung-Yong Lee. Plasmonic forward scattering effect in organic solar cells: A powerful optical engineering method. *Sci. Rep.*, 3, April 2013. PMID: 23615663 PMCID: PMC3635054. (Cited on page 25.)
- [36] Ricky B. Dunbar, Thomas Pfadler, and Lukas Schmidt-Mende. Highly absorbing solar cells - a survey of plasmonic nanostructures. *Opt. Express*, 20(S2):A177–A189, 2012. (Cited on page 25.)
- [37] Gilles Dennler, Markus C. Scharber, and Christoph J. Brabec. Polymer-fullerene bulk-heterojunction solar cells. *Advanced Materials*, 21(13):1323–1338, 2009. (Cited on page 26.)
- [38] Jian Wang, Yun-Ju Lee, Arvinder S. Chadha, Juan Yi, Michael L. Jespersen, John J. Kelley, Hue M. Nguyen, Michael Nimmo, Anton V. Malko, Richard A. Vaia, Weidong Zhou, and Julia W. P. Hsu. Effect of plasmonic au nanoparticles on inverted organic solar cell performance. *J. Phys. Chem. C*, 117(1):85–91, 2013. (Cited on pages 29, 30, and 34.)
- [39] Michael Salvador, Bradley A. MacLeod, Angela Hess, Abhishek P. Kulkarni, Keiko Munechika, Jennifer I. L. Chen, and David S. Ginger. Electron accumulation on metal nanoparticles in plasmon-enhanced organic solar cells. *ACS Nano*, 2012. (Cited on page 30.)

- [40] V. D. Mihailesti, H. X. Xie, B. de Boer, L. J. A. Koster, and P. W. M. Blom. Charge transport and photocurrent generation in poly(3-hexylthiophene): Methanofullerene bulk-heterojunction solar cells. *Advanced Functional Materials*, 16(5):699–708, 2006. (Cited on page [34](#).)

Part III

AEROSOL-DERIVED NANOPARTICLE BASED
PLASMONIC DEVICES: SERS

SERS (SURFACE-ENHANCED RAMAN SCATTERING)



I present novel 3D metallic structures composed of multipetal flowers consisting of nanoparticles and demonstrate the control of surface plasmon hot-spots in terms of locations and intensities as a function of petal number for uniform and reproducible surface-enhanced Raman spectroscopy (SERS) with high field enhancements. I believe that multipetal nanoflower SERS substrate would pave the way to reliable SERS substrate platform based on dry aerosol technology.

3.1 INTRODUCTION

3.1.1 *Surface plasmon*

Surface plasmon (SP) has been one of intensively studied subjects in optical and material science in the last two decades. As a collective electric charge density oscillation of metal at dielectric-metal interface, SP resonance brings about strong electric field in the vicinity of metal surface. Intensive studies on optical properties of SP depending on the size, the material, and the morphology of diverse dielectric-metal compositions revealed high potential of SP for its ubiquitous applications; such as biochemical sensors [1], surface-enhanced Raman spectroscopy (SERS) [2, 3, 4, 5, 6, 7, 8, 9], nanooptical components [10, 11], negative refractive index materials [12], and photovoltaic devices [13].

3.1.2 *SERS Substrate*

Ideal SERS substrates should satisfy three important requirements including sufficiently high enhancement factors, uniformity and reproducibility, and facile synthesis of the substrate [4, 14]. Since it is now believed that the enhancement factors above 10^7 [4, 15, 16] or even above 10^6 [14, 17] would be sufficient for single molecule detection, the issues of uniformity, reproducibility, and practical synthesis become more important. However, SERS nanostructures made by nanoparticle based bottom-up approach face significant challenge of producing reproducible and uniform Raman response due to the difficulty making uniform SERS active sites while those structures could generate very high electric field enhancement at certain positions [4, 8, 18, 19]. On the other hand, electron or ion beam lithography-based top-down approaches could produce more uniform and reproducible nanostructures which would provide relatively uniform and reproducible signals [20]. But these nanofabrication techniques not only require time consuming serial processing in vacuum, which prohibits their practical application for large scale production, but also have limitation in fabricating versatile three dimensional nanostructures, which prevents to exploit the full advantages of SP. For example, SP nanostructures produced by lithography-based approaches have well-defined lateral shapes, but the shape in the vertical direction is hardly controllable although techni-

cally formidable layer-by-layer processes can be used. Even the most recently developed three-dimensional (3D) fabrication techniques [21, 22, 23, 24, 25] are not completely free from those limitations in tailoring the geometry / material and thus the resonance of nanostructures. Recent development of nanoimprint lithography could produce SERS nanostructures with practicality, however, still it may need multiple steps producing reliable nanogaps of metal structures, which could pose a problem of uniformity and reproducibility [5]. As a reliable nanoscale resolution, and tractable method of 3D architecture assembly in wafer scales, Ion-Assisted Aerosol Lithography (IAAL) [26, 27, 28, 29], which is a nanoparticle assembly method by ion induced electrostatic force guiding, has been introduced recently. This atmospheric and parallel process could provide uniform 3D nanostructures having 3D nanogaps that can be exploited for hot-spot engineering.

3.1.3 *Outline*

In this report I fabricate flower-shaped 3D metallic structures composed of m -petals, and demonstrate the control of SP hot-spots (in terms of their locations and intensities) as a function of the petal number m (4, 6, and 8). With the increase of the petal number, both the numbers of hot-spots that are formed in 3D nanogaps located between adjacent petals, and the field intensity in the hot-spots show super-linear m -dependent increase in the SERS enhancement as a whole. The obtained SERS enhancement is $\sim 10^7$, sufficient for the single molecule detection [4, 14, 15, 16, 17]. Quantitative and qualitative optical behaviors of fabricated 3D multipetal flower assemblies are also studied by measuring dark field (DF) spectra. Enhanced excitation of non-radiative higher order SP modes for the higher m -petal flowers is also interpreted in terms of m -petal geometry, in agreement with the results of SERS, DF spectra, and rigorously calculated electromagnetic field and surface charge density distributions. The uniformity and reproducibility of the present 3D multipetal flower SERS substrates were also examined. This study was performed together with Sungjun In in Department of Electrical and Computer Engineering at Seoul National University.

3.2 RESULT AND DISCUSSION

3.2.1 IAAL(*ion-assisted aerosol lithography*) for Nanoflower Arrays

I fabricated four different arrays of 3D plasmonic multipetal flower (*m*-PF) assemblies composed of nanoparticles for SERS substrates using spark discharge [30, 31] and ion induced electrostatic focusing method [26]. The homemade spark discharge device [31] is constructed by three chambers schematically shown in Figure 1a: a pin-to-plate type spark and a corona discharge chamber and a deposition chamber. In the spark discharge chamber a sharpened copper pin and a copper plate with a hole (~ 1 mm in diameter) are fixed with a distance of about 1 mm. Prior to the charged nanoparticle generation process, positive N_2 ions generated in the corona discharge chamber are deposited on the surface of SiO_2 which is patterned on a Si substrate. In the spark discharge chamber electric sparks are periodically generated between the pin and the plate by applying a positive voltage to the pin and connecting a ground to the plate. Electric sparks evaporate quasi-instantaneously copper, and charged copper nanoparticles (2 - 4 nm in diameter) are produced and blown into the deposition chamber by N_2 carrier gas fed into the spark discharge chamber. In the deposition chamber, a patterned electrically insulating SiO_2 layer with a 100 nm thickness on a Si substrate is biased by a negative voltage through the sample holder to attract only positive copper nanoparticles. Due to the repulsive Coulomb interaction from deposited N_2 positive ions on the surface of the SiO_2 layer, positively charged copper nanoparticles can be convergently assembled onto the center of bare Si surface in etched SiO_2 area.

In Figure 1b I illustrate 3D assembly processes by showing the electric field (dotted lines) and the corresponding equi-potential lines (solid lines) at an early (left) and a 3D building stage (right) in a cross sectional view of a 4-PF assembly cut by a symmetric plane. Rigorous numerical simulations of 2D electric field and equi-potential line distributions during particle deposition can be found elsewhere [29, 32]. At the early stage equi-potential lines determined by positive N_2 ions on the SiO_2 layer and the negative voltage on the Si substrate form a convex electrostatic lens [26] which focuses electric field lines on the bare Si surface. Therefore, positively charged copper nanoparticles following the electric field lines are deposited on the center region of etched area

within the SiO₂ layer. As assembled metal nanoparticles pile up in the vertical direction, quasi-electrostatic field lines change. In the 3D building stage, the attractive lenses covering the open area in the SiO₂ layer (grey lines) are weakened and suppressed by the neighboring repelling lenses (orange lines), which eventually allows nanoparticles to grow in the lateral direction as well. The repelling fields act as an electrostatic scaffold which determines lateral shapes of 3D nanoparticle buildings [29].

3.2.2 Fabrication of Multipetal Nanoflower Arrays using IAAL Method

Field-emission scanning electron microscope (FE-SEM) images of fabricated 4-, 6-, and two different 8-PF assemblies are presented in Figure 1 with the SiO₂ etched patterns at each top left corner. The several hundreds nanometer level SiO₂ prepatterns with 100 nm thickness on the Si substrate were prepared by undergoing E-beam lithography (JBX9300FS, JEOL) and etching (Multiplex ICP, STS) procedures although practical photolithography could be used for the present several hundreds nanometer level SiO₂ pre-patterns in principle. Here, I discriminate two 8-PF assemblies depending on the etched pattern in the SiO₂ layer, labeled as 8-r(t)PF (r and t denoting rectangular and trapezoidal, respectively). For the 4-PF array (Figure 1a) a square cross pattern having 500 nm in length and width with a 3000 nm period is used. The hexagonal pattern for the 6-PF array (Figure 1b) is constructed by rectangles with 500 nm in length and 200 nm in width in a 2500 nm periodic array. While the octagonal pattern for the 8-rPF array (Figure 2c) is composed of rectangles with 600 nm in length and 200 nm width in a 3000 nm periodic array, the 8-tPF array (Figure 2d) is based on a trapezoid with 600 nm in length, 400 nm for the topside, and 200 nm for the lower side in a 3500 nm periodic array. All of the *m*-PF arrays are fabricated under the same experimental conditions. At the positive ion generation step, 2.5 kV bias is applied to the tungsten pin while -1.5 kV to the Si substrate, the carrier gas flow rate into the corona discharge chamber is 4 lpm, and deposition time is set to be 20 min. During the charged nanoparticle generation and deposition step, 5.6 kV bias is applied to the pin and -4 kV to the Si substrate. The flow rate of the carrier gas into the spark discharge chamber is controlled to 4 lpm during the deposition time of 4 hours. For quantitative comparison of the SERS

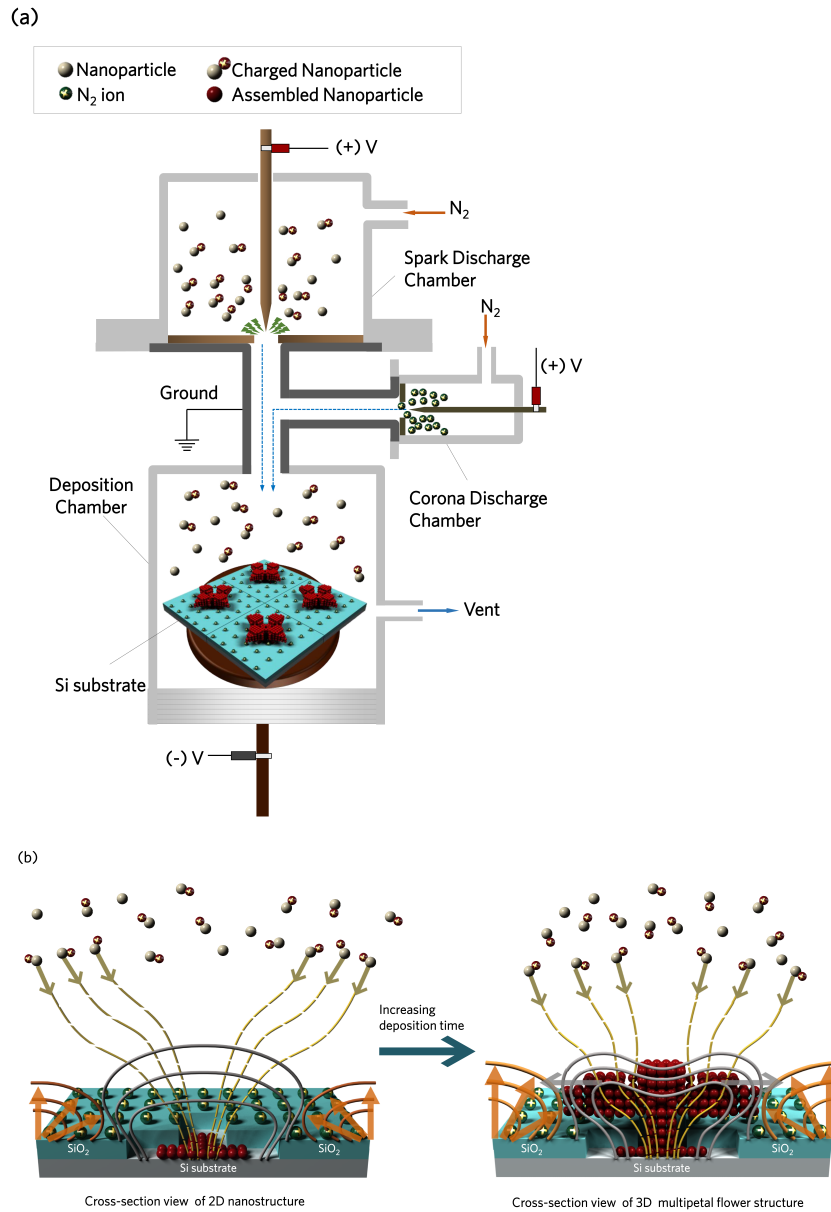


Figure 1: Fabrication of plasmonic 3D multipetal flower (*m*-PF) arrays and illustration of ion-assisted focusing lenses. (a) Scheme of *m*-PF building method using spark discharge device. (b) cross-sectional view illustrating assembly process of nanoparticles for 4-PF array through ion-assisted focusing lenses: a flat structure in an early stage (left), full grown flower structure in a 3D building stage (right).

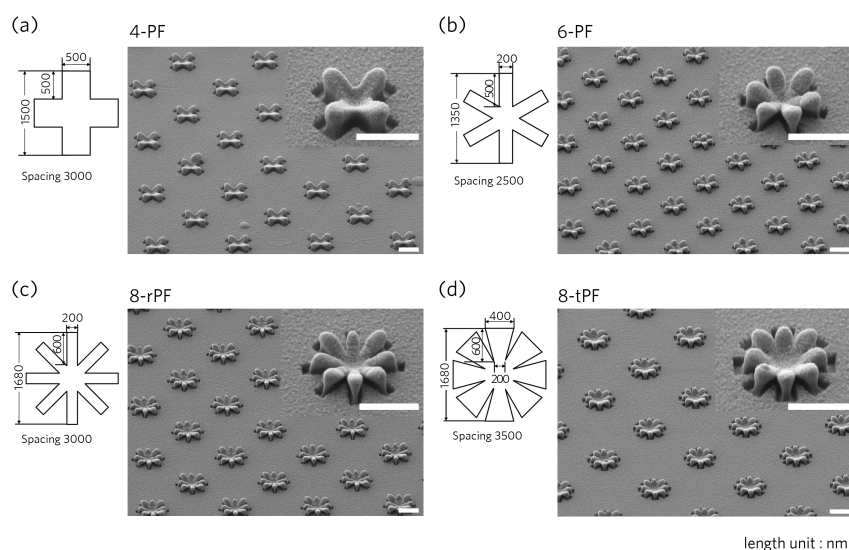


Figure 2: FE-SEM images of fabricated multipetal flowers (*m*-PF) arrays with etched pattern geometries at each left top corner. (a) 4-PF (b) 6-PF (c) 8-rPF (d) 8-tPF (scale bar: 1000 nm).

enhancement of the 3D *m*-PF arrays I also fabricated a 2D flat particle film by using the same spark discharge method. Four hours of deposition time was used to build up a flat copper particle film. I chose benzenethiol (BT) as a Raman-active probe. However, on account of the chemical character of BT molecules which are hardly binding to copper surfaces but easily chemisorbed as a monolayer on the surface of a thiol (-SH) group such as gold, I sputtered gold onto SERS substrates to a thickness of 50 nm. The same gold sputtering was also done to the 2D flat particle film for a fair comparison. For other analytes than gold binding molecules, the SERS surface should be modified by using various surface functionalizations. [1, 33] For Raman spectrum measurement a 633 nm cw He-Ne laser was employed with a beam spot size of 860 nm (100× objective with NA = 0.9). The scattered light intensity from samples was measured by a LN₂ cooled CCD detector attached to the spectrometer.

3.2.3 SERS Experiments

Figure 3a illustrates SERS experimental configuration for multipetal architecture (left) and particle film (right). These SERS configurations consist of three steps that are copper nanoparticle deposition on the substrate via spark discharge, 50 nm thick gold layer sputtering on the structure, and BT molecules binding on the top gold layer. Figure 3b presents Raman spectra of BT molecules chemisorbed on gold coated 4-, 6-, two 8-PF arrays, and the flat gold coated particle film. One can find four distinctive Raman peaks of BT molecules at 997 cm^{-1} , 1023 cm^{-1} , 1075 cm^{-1} , and 1575 cm^{-1} which correspond respectively to the CCC ring in-plane bending mode, CH in-plane bending mode, in-plane CCC ring breathing mode with CS stretching mode, and CC stretching mode [34]. Compared to Raman spectrum of the flat particle film surface, I observe significant increase of Raman peak intensities as the number of petals increases and obtain the highest intensity value when the 8-tPF array was used as a SERS substrate. I estimate the SERS enhancement factor (EF) of each SERS substrate by using the formula $EF = (I_{SERS}/N_{SERS})/(I_{ref}/N_{ref})$ where I_{SERS} and I_{ref} are Raman peak intensities of BT molecules chemisorbed on a SERS substrate and in a reference sample at 1575 cm^{-1} , respectively and N_{SERS} and N_{ref} are the numbers of BT molecules exposed to the incident laser on the SERS substrate and in the reference sample, respectively. In Table 1 I list measured Raman intensities and SERS EFs for each SERS substrate. An EF on a scale of $\sim 10^7$ is obtained for the 8-r(t)PF array. Compared to the Raman intensity ratio of the 4-PF arrays with respect to that of the gold coated particle film surface ($I_{4-PF}/I_{film} \sim 16$), both 6-PF and 8-r(t)PF arrays show much larger enhancements than those determined by the ratio of petal numbers.

3.2.4 Electromagnetic Simulations for Four and Eight Petal Nanostructures

To elucidate the physical origin and confirm for the experimentally observed SERS EF of the m -PF, I performed finite element method electromagnetic simulation analysis (COMSOL Multi-physics) for 3D m -PF structures imported from CATIA (CAD modeling program) construction (Figure 4a and 5a). For calculating the electric field distribution of each m -PF, I used the z -direction propagating x -(or y -) polarized

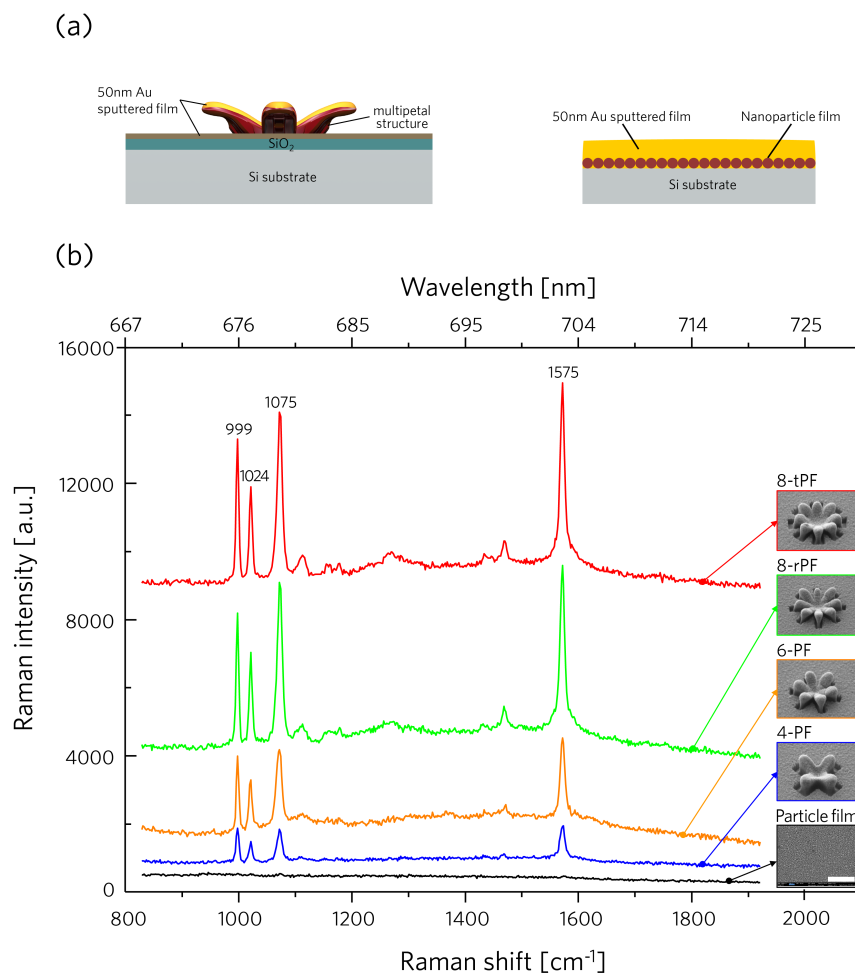


Figure 3: (a) Schematic illustration of SERS substrate configuration for a multipetal architecture (left) and a particle film (right). These SERS configurations consist of three steps: copper nanoparticle deposition on the substrate via spark discharge, 50 nm thick gold layer sputtering on the structure, and BT molecules binding on the top gold layer. (b) Raman spectra of BT molecules for the particle film, 4-, 6-, 8-r, and 8-tPF array (scale bar: 1000 nm).

Architecture	Raman intensity	EF	Raman intensity Ratio (I_{m-PF}/I_{film})
8-tPF	5234	1.91×10^7	87.2
8-rPF	4984	1.82×10^7	83.1
6-PF	2341	9.84×10^6	39.0
4-PF	939	4.66×10^6	15.7
film	60	2.19×10^5	1

Table 1: Raman intensities and enhancement factors of BT molecules (10^{-4} M) for particle film and *m*-PF arrays at 1575cm^{-1}

Gaussian wave source focused on the center of the *m*-PF. The material parameters of the *m*-PF were taken from the experimentally measured complex and dispersive optical constants (SiO_2 [35], Si [36], copper[36] and gold [37]). To understand these behaviors of the *m*-PF SERS EF, I focus on 4-PF and 8-tPF cases as shown in Figure 4b and 5b to show the distinctive hot-spots of the *m*-PF, developed in 3D nanogaps where adjacent two petals converge. Figure 4c and 5c show the plots of the electric field distributions at $z = 220$ nm for 4-PF and $z = 300$ nm for 8-tPF, respectively with unpolarized light source, confirming the role of 3D nanogaps as the dominant hot-spots in the *m*-PF. This is well explained by the behavior of free-carriers in metallic nanogaps under the quasi-static regime. Upon the light incident on the deep-subwavelength scale nanogap between the petals, the in-plane gap-normal component of quasi-static electromagnetic field induces huge accumulation of opposite charges at both sides of the nanogap, creating extra-ordinary enhanced electric field [38, 39]. The 8-PF with 8 nanogaps has twice as many hot-spots as than the 4-PF of four nanogaps, and most importantly due to the smaller gap width (than the case of 4-PF), has a stronger field in the gap than that of the 4-PF, which was confirmed by calculations. The "super-linear" (faster than m_1 from the increased number of hot spots) increase of EF for the increased number of petals is observed experimentally, which is in good agreement with numerical results obtained by integrating $|E|^4$ over the SERS volume covering petal surface where the SERS molecule resides. In this calculations, I followed the method used in Kang et al. [40] where $|E|^4$ was integrated over the SERS volume by varying thicknesses on the SERS surface from

10 to 50 nm to be compared with experimentally determined Raman signal enhancement. As shown in Table 3, compared to Au film case, both 4-PF and 8-tPF cases yielded much enhanced results and the calculated enhancement of the 8-tPF case indeed showed “super-linear” behavior ranging 5 to 7 times compared to the 4-PF case for all tested thicknesses, which is in agreement with experimental data (measured SERS intensity ratio of 8-tPF to 4-PF \sim 5.55 can be estimated from Table 1).

3.2.5 Dark field(DF) microscopy : DF Spectra and DF Images

Resonance feature of the *m*-PF arrays is also investigated by measuring DF microscopy image and spectrum. In Figure 6a and 6b I compare images and spectra of a 4-PF and an 8-tPF. (DF images for 4, 6-PF, and 8-r(t)PF arrays are shown in Figure 7.) In DF images (insets) I identify that while the image of the 4-PF is dominated by two colors (orange and green), the 8-PF shows a more colorful image. Such optical behaviors are in good agreement with DF spectra. Four broad peaks at 440, 640, 700, and 768 nm are assigned to the 4-PF (Figure 6a), whereas six peaks at 440, 625, 668, 711, 750, and 788 nm are assigned to the 8-PF (Figure 6b). The peak at 440 nm and the dip at 495 nm found in both spectra are attributed to the collective plasmon resonance in the *m*-PF arrays sharing similar array periodicity (\sim 3 μ m) and overall feature size (\sim 1.7 μ m). Figure 6c-f shows the calculated surface charge density distributions of the 4-PF and the 8-tPF, for the incidence of linearly *x*-polarized light at 495 nm and 700 nm. For the wavelength of 495 nm (Figure 6c and e), as expected, in addition to the dipole-like charge distributions on each nanoflower surface, strong interactions between horizontally and vertically neighboring flower assemblies can be noticed. Furthermore, I can address localized surface plasmon multipole resonance on the 8-tPF at the wavelength of 700 nm in Figure 6f, which could account for the reduced reflectivity in whole wavelength range, compared to that of the 4-PF. By virtue of the increased number of hot-spots accompanied by enhanced hot-spot intensity, the 8-PF has stronger near-field characteristics than the 4-PF, which is also consistent with the enhanced SERS efficiency.

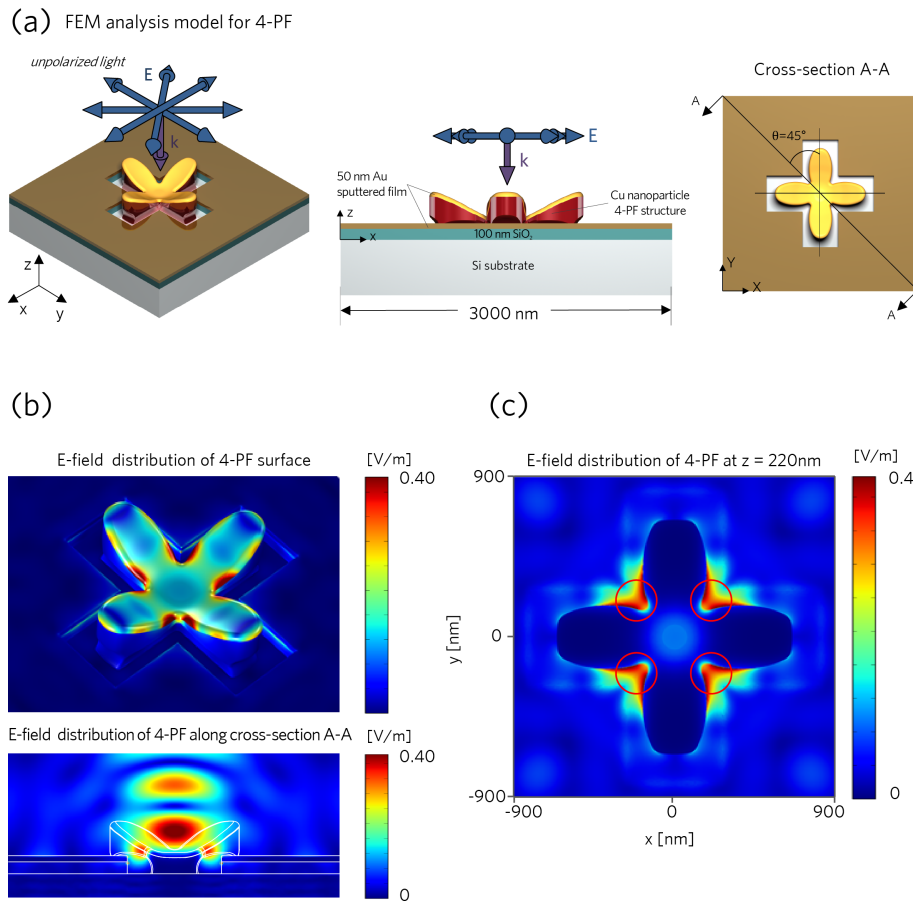


Figure 4: Electromagnetic simulation results of the 4-PF. (a) Schematic view of the simulation model (left), model structure and geometry (middle), a cross-section location of A-A line (right). (b) 3D perspective view (top) and 2D electric field distributions in the plane containing A-A (bottom), (c) The electric field distribution at $z = 220$ nm for unpolarized light.

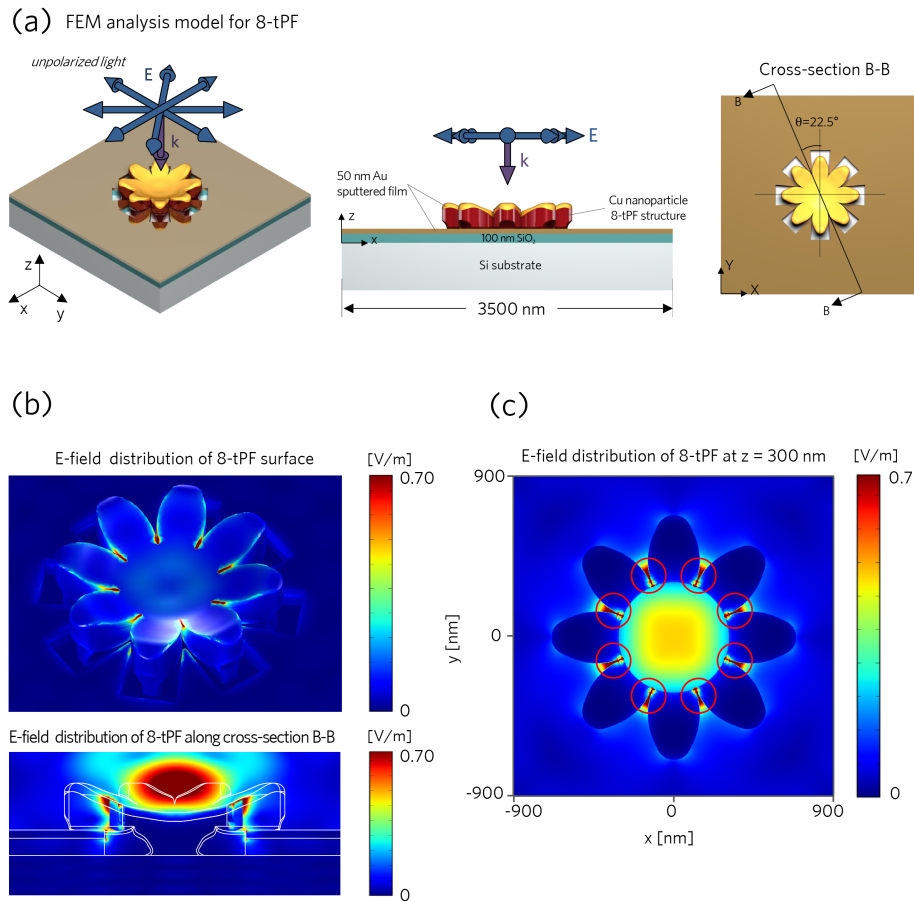


Figure 5: Electromagnetic simulation results of the 8-tPF. (a) Schematic view of the simulation model (left), model structure and geometry (middle), a cross-section location of B-B line (right). (b) 3D perspective view (top) and 2D electric field distributions in the plane containing B-B (bottom), (c) The electric field distribution at $z = 300$ nm for unpolarized light

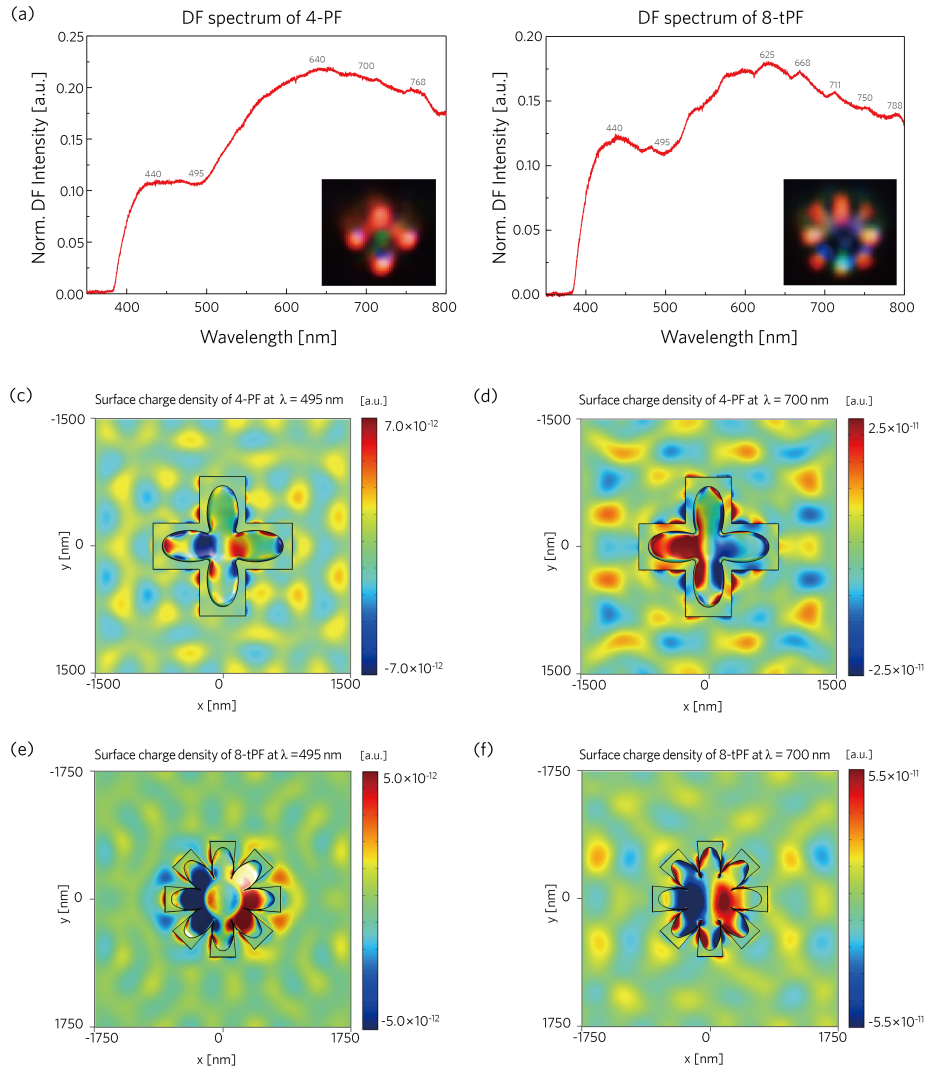
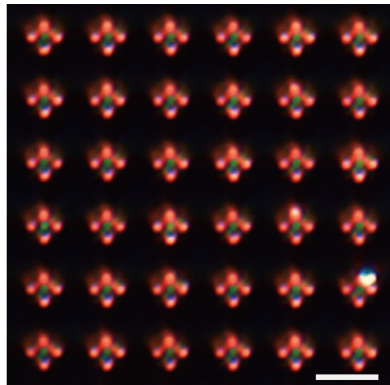
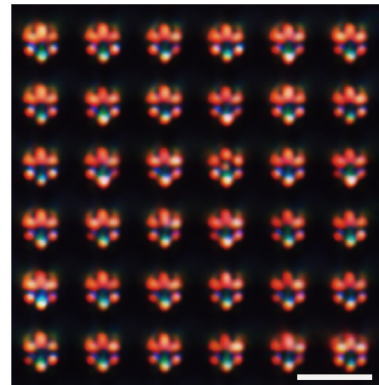


Figure 6: DF spectra, DF images of a 4-PF and an 8-tPF, and calculated surface charge density distributions. DF spectra and images (inset) of the 4-PF (a) and the 8-tPF (b). Surface charge density distributions of the 4-PF (c and d) and the 8-tPF (e and f) at $\lambda = 495$ nm (c and e) and $\lambda = 700$ nm (d and f) for the x- polarized light.

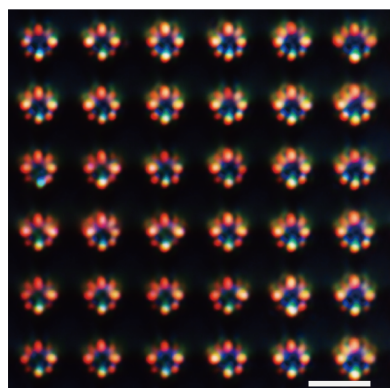
(a) 4-PF



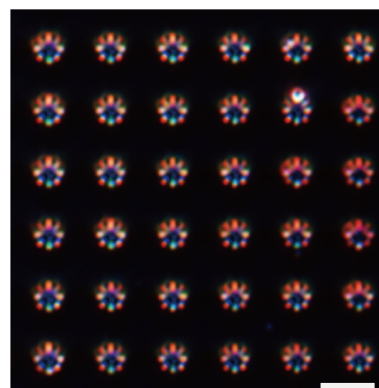
(b) 6-PF



(c) 8-rPF



(d) 8-tPF



Scale bar : 3000nm

Figure 7: DF images of gold film coated copper nanoparticle multipetal arrays with m -fold symmetric multicolor distribution : (a) 4-PF (b) 6-PF (c) 8-rPF (d) 8-tPF (Scale bar : 3000 nm)

3.2.6 *Reproducible and Uniform SERS Substrate of m-PF Arrays*

I also did additional control experiments using gold coated Cu nanoparticle film case (the same sizes of Cu nanoparticles used for the fabrication of present 3D multi petal flowers), 50 nm Au nanoparticle case, and Au coated SiO₂ pattern case (the same patterns used for fabricating these 3D multi-petal flowers) all of which showed lower Raman signals compared to the 3D multi-petal flowers. For 50 nm Au nanoparticle coated sample, non-uniform Raman signals were observed as shown in Fig. S3(b) due to the difficulty to provide uniform distribution of nanogaps made between nanoparticles deposited on the substrate. One can expect the similar difficulty for nanorods case if they are randomly coated on the substrate. Precise alignment and positioning of nanorods should be needed to ensure uniformity and reproducibility. In contrast, as mentioned above, the 3D multi-petal flower structures show uniform and reproducible signals with sufficiently high EF $\sim 10^7$. It is known that bottom-up approach of assembly of nanoparticle or nanorods usually suffer the problem of uniformity and reproducibility while the top down approach such as electron-beam lithography generally can manufacture well defined uniform and reproducible nanogaps, therefore, provide uniform and reproducible Raman signal. However, the nanoscale top down approaches such as E-beam lithography or focused ion beam lithography need vacuum and serial approach, therefore, scalability is an issue. Note that this approach is a hybrid method combining (bottom up) particle assembly and (top-down) photo-lithography, both of which are parallel process. Now I would like to emphasize that this method provides an easy route for manufacturing the complicated 3D structures containing uniform/reproducible nanogaps compared with previously used methods. This method only needs (parallel) photo-lithography when producing a few hundred nanometer range SiO₂ pre-patterns since as shown in the revised version, the electrostatic focusing capability could produce (3D) nanogaps between petals of 3D nanoparticle flowers by assembling charged nanoparticles with significantly reduced feature at atmospheric condition. Even though these 3D structures seem to be shown very complicated to be fabricated, the present method that is an atmospheric parallel process is much simpler than commonly used electron beam lithography (that requires vacuum and serial approach), but can easily produce complicated 3D structures

with nanoscale resolution and uniform reproducibility, which is a major advantage of the present methodology. Another top down, but practical (parallel) approach, NIL (Nanoimprint Lithography) can produce versatile 2D nanostructures with reproducibility. Note that NIL requires e-beam lithography to fabricate stamp, but this method only needs photo-lithography in principle. Furthermore, it would not be easy to fabricate metal nanostructures ensuring nanogaps with NIL since usually NIL is used for soft materials (such as polymer) patterning and NIL alone would be difficult to pattern even soft materials within 10 nm scale in the current stage. Additional steps may be needed to ensure nanogaps when using NIL. For example, Ou et al. [5] reported three combined steps (to ensure nanogaps) including (1) NIL approach to fabricate polymer nano-pillars (2) metal coating on these pillars (3) collapsing of these Au coated pillars by microcapillary force. But it is not clear whether these multiple steps (particularly, collapsing step) could ensure uniform and reproducible nanogap structures. I would like to emphasize that the atmospheric (although several hundred nm level SiO₂ pre-patterns require practical photo-lithography in principle) and parallel particle assembly method would be much easier to fabricate various 3D structures containing 3D nanogaps that ensure high enough EF, uniform and reproducibility.

I carried out additional experiments for a comparison of the 3D multipetal structures with three different controlled samples; gold coated Cu particle film (the same Cu nanoparticles used for the fabrication of the 3D multipetal flowers), 50 nm gold nanoparticle coated sample, and gold coated SiO₂ patterns that are the same SiO₂ patterns that I utilized (Figure 8). Compared to the 3D multipetal flowers, the other three controlled samples showed significantly lower Raman signals. Furthermore, Au nanoparticle adsorbed substrate case showed non-uniform signals in Figure 8b. To examine the uniformity and reproducibility, I performed SERS experiments for two different samples of the multipetal flower arrays. I obtained SERS signals at five different flowers of each 4-PF, 6-PF, 8-rPF, and 8-tPF array in each sample. The standard deviation of five signals is less than 10% of average SERS signal (uniformity) and the average SERS signal difference between two different samples is less than 6% (reproducibility). The detailed results for uniformity and reproducibility are shown in Table 2, Figure 10, and Figure 11

Architecture	Sample 1	Sample 2	Difference (%)
	Raman intensity (average \pm std)	Raman intensity (average \pm std)	
8-tPF	989 \pm 46	1003 \pm 87	1.4
8-rPF	2438 \pm 234	2370 \pm 191	2.8
6-PF	5244 \pm 314	4920 \pm 305	6.2
4-PF	5121 \pm 213	5287 \pm 261	3.1

Table 2: Average Raman intensities of BT molecules at 1575 cm^{-1} and their differences for 3D multipetal flower arrays obtained from two different SERS substrates sample 1 and 2 (SEM images shown in Figure 8).

$|E|^4$ volume integration ratios, $(\int |E|^4 dV / \int dV)_{4-8-tPF} / (\int |E|^4 dV / \int dV)_{film}$

Layer thickness(t)	10 nm	20 nm	30 nm	40 nm	50 nm
Equations					
4-PF / film	52.67	27.92	16.03	9.89	6.51
8-tPF / film	376.75	160.31	88.93	56.56	39.55
8-tPF / 4-PF	7.15	5.74	5.55	5.72	6.08

Table 3: Calculated ratios of $|E|^4$ integration for 4-PF (8-tPF) over the SERS volume covering multipetal surface with variation of the layer thickness ($t = 10 - 50$ nm) compared to that of gold coated film.

and the SEM images of 4-PF, 6-PF, 8-PF arrays for two different samples are shown in Figure 8.

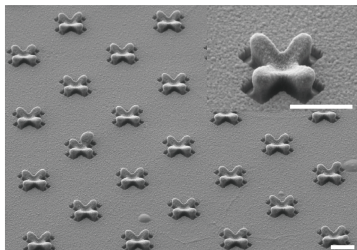
3.3 EXPERIMENT

3.3.1 SERS Enhancement Factor Calculation

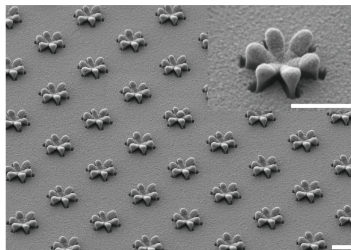
I calculated the enhancement factors (EFs) for the quantitative evaluation of the SERS efficiency of different morphology of structures by analyzing the relative Raman intensities of the specific peak (1575 cm^{-1}) of benzenethiol, Raman reporter molecule.

(1) Sample 1

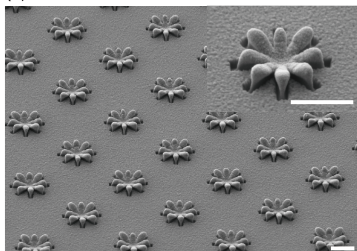
(a) 4-PF



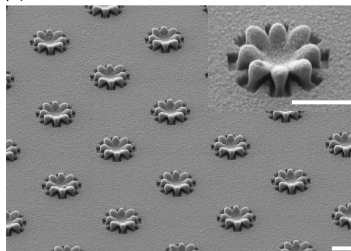
(b) 6-PF



(c) 8-rPF

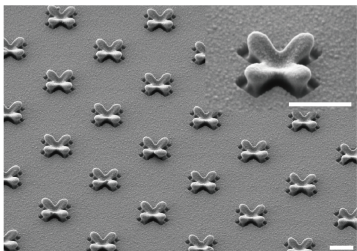


(d) 8-tPF

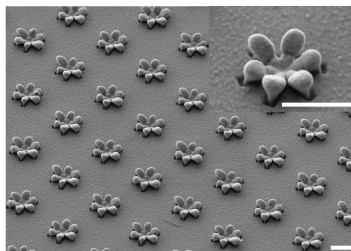


(2) Sample 2

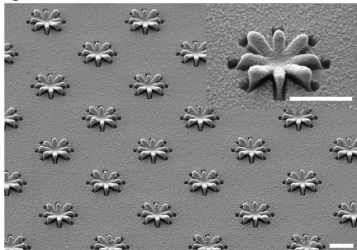
(e) 4-PF



(f) 6-PF



(g) 8-rPF



(h) 8-tPF

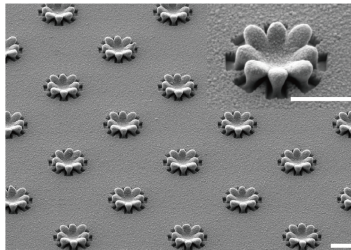


Figure 8: FE-SEM images of fabricated multipetal flower arrays for two different samples. (a) 4-PF (b) 6-PF (c) 8-rPF (d) 8-tPF arrays in the SERS sample 1 and (e) 4-PF (f) 6-PF (g) 8-rPF (h) 8-tPF arrays in the SERS sample 2 (scale bar: 1000 nm).

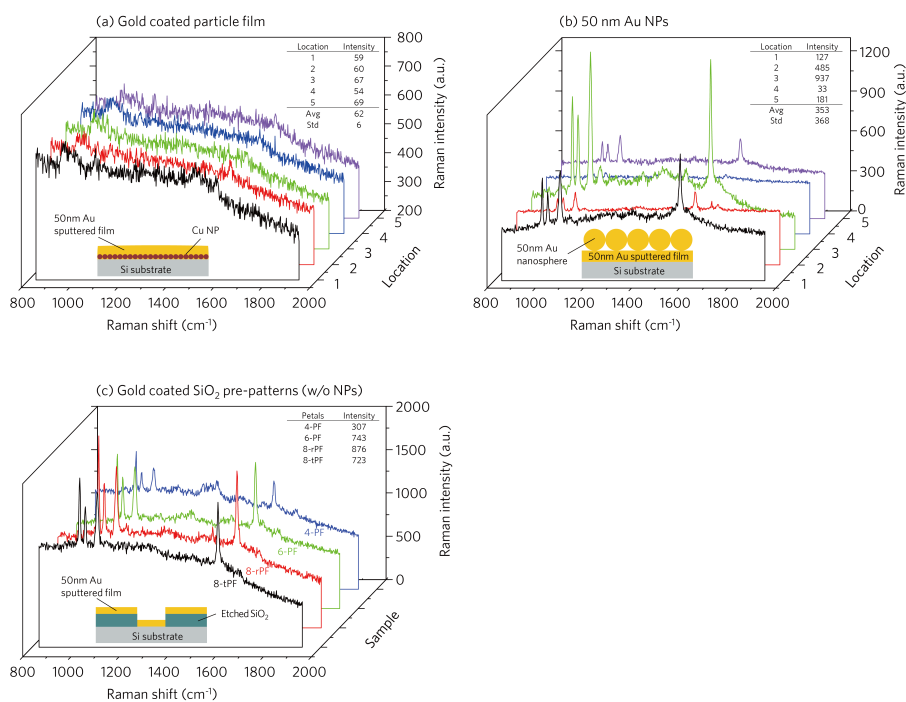


Figure 9: Raman spectra of BT molecules for (a) gold coated Cu particle film on Si substrate (b) spin-coated Au NPs ($d = 50$ nm) on Si substrate (c) gold coated pre-patterned samples (having SiO₂ etched part as shown in Figure 2) without Cu nanoparticles deposition. Each schematic inset at the bottom side represents the experiment configuration for SERS substrate. Each inset table at the top right corner demonstrates Raman intensity of the BT molecules at 1575 cm^{-1} .

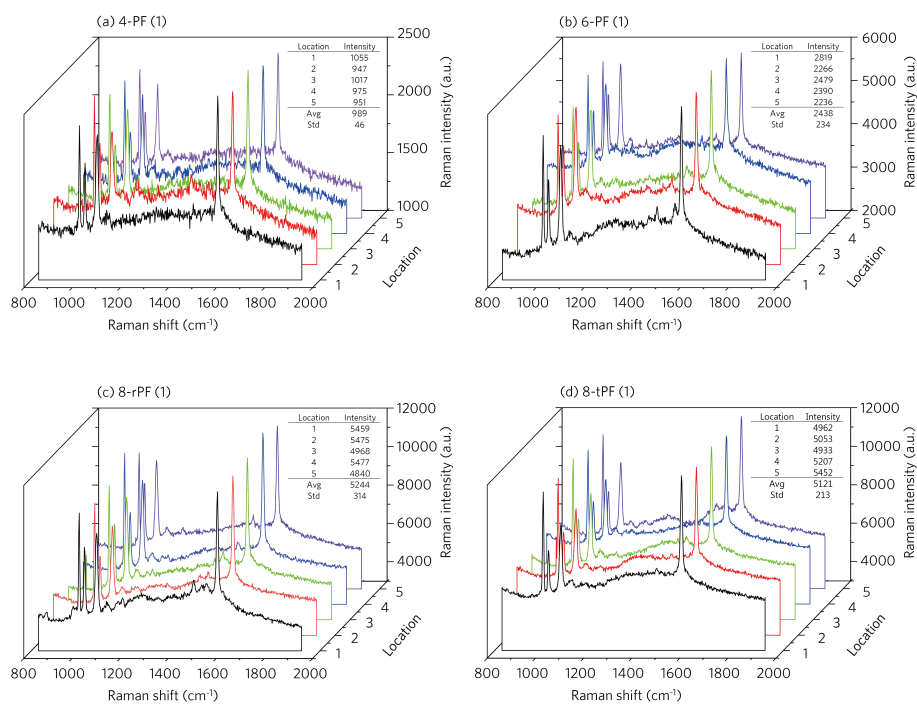


Figure 10: Raman spectra of BT molecules for (a) 4-PF (b) 6-PF (c) 8-rPF (d) 8-tPF arrays of the SERS substrate sample 1 depicted in Figure 8 (a)-(d). Each inset table at the top right corner demonstrates Raman intensity of the BT molecules at 1575 cm^{-1} for five different locations.

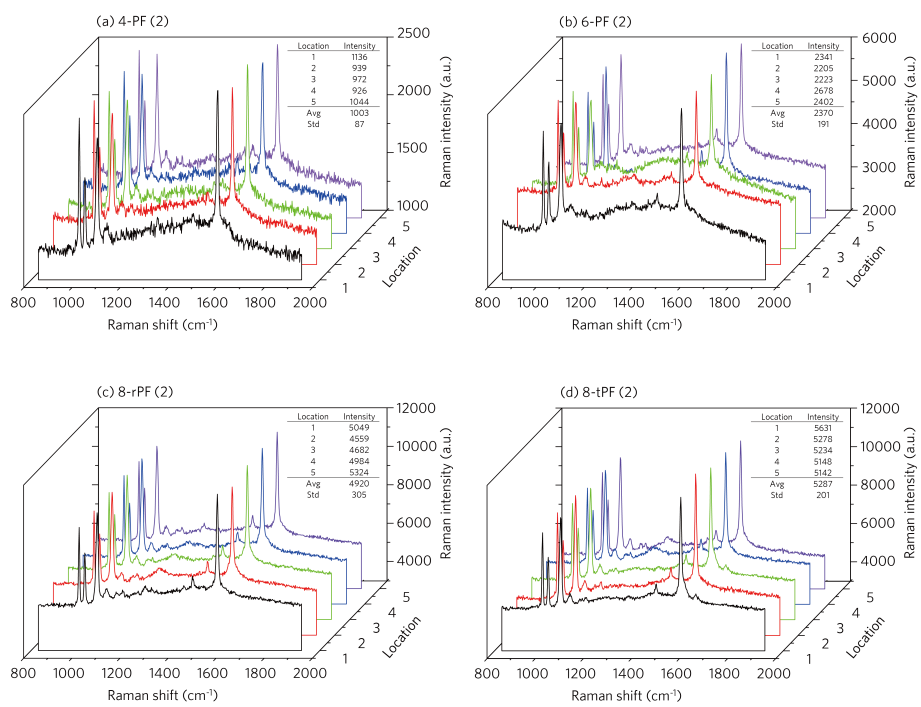


Figure 11: Raman spectra of BT molecules for (a) 4-PF (b) 6-PF (c) 8-rPF (d) 8-tPF arrays of the second SERS substrate sample 2 depicted in Figure 8 (e)-(h). Each inset table at the top right corner demonstrates Raman intensity of the BT molecules at 1575 cm^{-1} for five different locations.

I evaluated SERS EFs on the particle film and the m-PF arrays by following equation:

$$EF = \eta_{collection} \cdot \frac{I_{SERS}/N_{SERS}}{I_{ref}/N_{ref}} = \eta_{collection} \cdot \frac{I_{SERS}}{I_{ref}} \cdot \frac{N_{ref}}{N_{SERS}}$$

where light collection efficiency, $\eta_{collection} = 0.071$ [41], was considered since different objectives were employed for measuring I_{SERS} and I_{ref} (100× objective for I_{SERS} and 10× objective for I_{ref}). I_{SERS} is the Raman intensity of BT on the film and the m-PF arrays as shown in Table 1 and I_{ref} is the reference Raman intensity of BT of the reference sample. N_{SERS} is the number of excited molecules on the particle film and the m-PF and N_{ref} is the number of excited molecules in the reference sample. For the reference BT sample, I implemented a microwell with an area of 0.2 cm² (d = 5 mm) and a height of 62 μm in which BT solution is filled. If this height of microwell is below than the penetration depth of the bulk BT solution for the given optical system, I can easily estimate the reference Raman signal of BT molecules since the volume of BT solution illuminated by the laser source can be simply calculated by the beam spot area times the height of the microwell. In this case, I do not require the penetration depth which is only needed when BT bulk solution filled in a macro-scale glass vial or bottle is used for reference Raman experiment. I need to check whether the height of the microwell is below the penetration depth of BT bulk solution or not. To check about this, I additionally tested a microwell with the same area, but a larger height about 120 μm to confirm whether Raman signal is increasing with the height or maintains the same. If the Raman signal of reference BT maintains the same even with the increase of the height, then the penetration depth should be less than 62 μm. For the present case I confirmed that Raman signal was proportionally increasing with the height, which indicated that the height of the microwell, 62 μm is less than that of the 120 μm; Raman signals of reference BT for the microwell configuration with 62 μm and 120 μm heights were 67 and 112, respectively. Then, as mentioned above, I can directly estimate the reference Raman signal of BT from the measured Raman signal (67) and the volume of BT solution in the microwell with 62 μm height illuminated by laser beam spot. I calculated N_{ref} as follows:

$$N_{ref} = \frac{V_{laser} \times \rho_{BT} \times N_{AV}}{M_{BT}} = \frac{\left(\frac{\pi w_{ref}^2}{4} \times h\right) \times \rho_{BT} \times N_{AV}}{M_{BT}}$$

V_{laser} is laser excitation volume, w_{ref} is laser spot size through the 10× objective, and h is the height of the microwell for the reference BT sample (62 μm). ρ_{BT} is the density of BT molecules (1.08 g/cm³), N_{Av} is Avogadro number (6.02×10²³ molecules/mol), and M_{BT} is molar mass of BT molecules (110.19 g/mol). By considering the NA of objectives and the incident wavelength of laser, I can calculate the He-Ne laser spot size (w_{ref}) below equation [42]:

$$w_{ref} = 1.22 \frac{\lambda_{ex}}{NA_{10 \times obj}} = 1.22 \frac{633 \text{ nm}}{0.25} = 3089 \text{ nm} \approx 3.1 \mu\text{m}$$

Then,

$$N_{ref} = \frac{\left(\frac{3}{4}(3.1 \mu\text{m})^2 \times 1.08 \text{ g/cm}^3 \times 6.02 \times 10^{23} \text{ molecules/mol}\right)}{110.19 \text{ g/mol}} = 2.74 \times 10^{12} \text{ molecules}$$

I determined N_{SERS} as below:

$$N_{SERS} = S \times \sigma_{BT} \times N_{AV}$$

S is the effective surface area of nanoparticle structure where BT molecules are adsorbed and can be estimated by SEM images and 3D CAD package. ρ_{BT} is the surface density (0.45 nmol/cm²[43]) of BT molecules forming a monolayer on the metal surface. Then,

$$N_{SERS} = 1.21 \mu\text{m}^2 \times 0.45 \text{ nmol/cm}^2 \times 6.02 \times 10^{23} \text{ molecules/mol} = 3.27 \times 10^6 \text{ molecules}$$

Finally, the SERS EF of an 8-tPF is obtained as

$$EF_{8-tPF} = \eta_{collection} \cdot \frac{I_{SERS}}{I_{ref}} \cdot \frac{N_{ref}}{N_{SERS}} = 0.071 \frac{5234 / (0.16 \text{ mW} \times 30 \text{ s})}{67 / (2 \text{ mW} \times 10 \text{ s})} \cdot \frac{2.74 \times 10^{12}}{3.27 \times 10^6} = 1.91 \times 10^7$$

Reference	λ_{ex} [nm]	Objective		Penetration depth [μm]	
		Magnification	NA	In article	Calculation
					$h = \frac{2\lambda_{ex} \cdot n_{BT}}{NA^2}$
A[45]	633	20 ×	0.4	75	12.57
B[46]	633	50 ×	0.75	20	3.57
C[24]	633	50 ×	0.5	110	8.04

(Refractive index of benzenethiol, $n_{BT} = 1.588$)

Table 4: Comparison of penetration depths with respect to calculations and references

I also evaluated relative Raman intensity ratios of the m-PF array to the film as shown in Table 1.

3.3.2 Penetration Depth

The equation was for the depth of focus of the lens which was assumed to be equivalent to the penetration depth in [44]. Originally, I followed this assumption to evaluate the penetration depth of bulk BT, however, I realized during that this assumption would result in large errors since the studies adopting actual measurement values of penetration depth consistently revealed much larger penetration depths compared to the calculations based on the depth of focus. I described significant differences below; see the comparison between the penetration depths used in the previous studies and calculations based on the equation.

From this comparison, I concluded that the calculation based on the depth of focus could lead to erroneous results of penetration depth since the actual penetration depth should not only depend on the lens characteristics, but also on the absorption characteristic of the solution which was not taken into account in the equation of the depth of focus. Therefore, I did not use this equation to estimate penetration depth, but I adopted more direct way of measurement to determine reference Raman intensity from one molecule of BT (benzenethiol). Instead of using macroscale BT solution which required the correct estimation of penetration depth, I used a micro well with an area of 0.2 cm^2 ($d \sim 5$

mm) and a height of $62 \mu\text{m}$ in which BT solution is filled. If this height of the well is below than the penetration depth of the bulk BT solution, I can easily estimate the reference Raman signal of one BT molecule since the volume of BT solution illuminated by the source laser can be simply calculated by the beam spot area times the height of the micro-well. In this case, I do not need to know the penetration depth that is only needed if BT bulk solution is used. Of course I need to check whether the height of the well is below the penetration depth of bulk BT solution or not. To check about this, I additionally tested a micro well with the same area, but a larger height about $120 \mu\text{m}$ to confirm whether Raman signal is increasing with the height or maintains the same. If the Raman signal maintains the same even with the increase of the height, then the penetration depth should be less than $62 \mu\text{m}$. However, for the present case, I confirmed that Raman signal was proportionally increasing with the height, which indicated that the height of the micro-well, $62 \mu\text{m}$, is less than the bulk penetration depth. Then, as mentioned above, I can directly estimate the reference Raman signal of one BT molecule from the measured Raman signal and the volume of BT solution in the micro well illuminated by laser beam spot.

3.3.3 SERS Experiment

A titanium adhesion layer (5 nm in thickness) and a gold layer (50 nm in thickness) are sputtered respectively onto the copper flower arrays including a SiO_2 layer and a copper film. Gold coated flower arrays are dipped in 10^{-4} M ethanol solution of benzenethiol (98% Sigma Aldrich) for 12 hours and are dried through nitrogen blower for several minutes. Raman microscope with a LN_2 cooled CCD multichannel detector (LabRam HR, Horiba Jobin-Yvon) records Raman spectra from SERS substrate. A He-Ne laser with 633 nm excitation wavelength was utilized to illuminate onto the reference sample and the SERS substrates through a $10\times$ (NA = 0.25, beam diameter $\sim 3.1 \mu\text{m}$) and a $100\times$ objective (NA = 0.9, beam diameter ~ 860 nm), respectively. The SERS spectra are recorded using the LN_2 cooled CCD detector that collects the back-scattered light from the SERS substrate. The average diameter of laser beam was approximately 860 nm. An incident laser with 0.16 mW was irradiated onto the sample for 30 seconds.

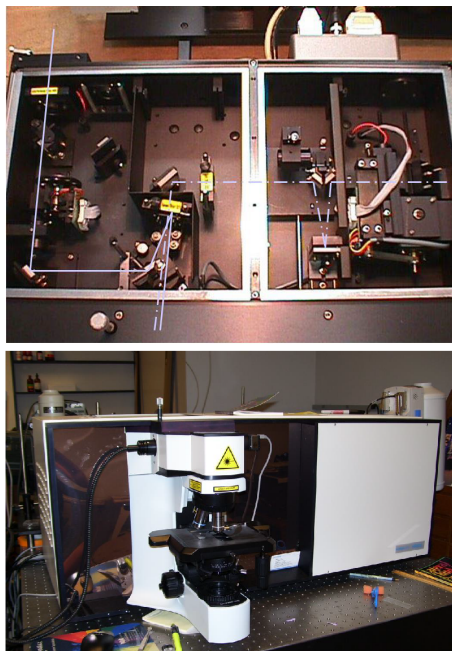
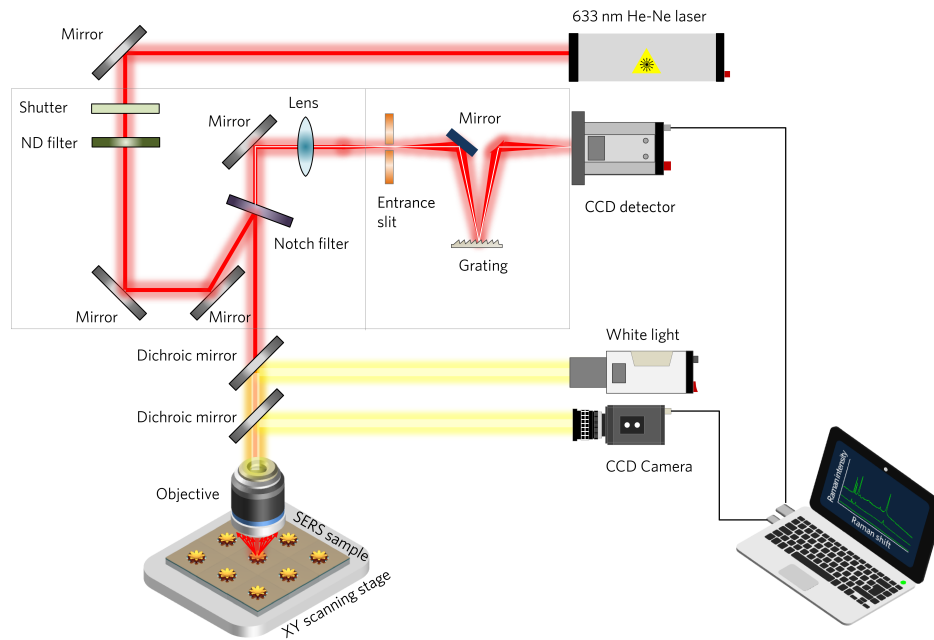


Figure 12: Schematic representation of Raman spectroscopy system for measuring SERS signals (top), SERS experimental setup of confocal micro-Raman microscope (bottom)

3.3.4 *Dark field (DF) Microscopy*

An optical microscopy (BX51, Olympus) with a 100W halogen white light source utilizes a 17.3 mega pixels color CCD camera (DP73, Olympus), a 100× dark field objective (NA=0.9), and a spectrometer that consists of an imaging monochromator (MonoRa320i, Dongwoo Optron) and a cooled CCD (iDus DU420A-BR-DD, Ando technology). The visible light that passes through a DF condenser illuminates onto the sample through the 100× objective. The scattered/reflected light that passes through the objective is recorded by the spectrometer set for DF spectra. The back-scattered light from the sample is collected by the color CCD camera to capture DF images. By adjusting the opening size of the slit mounted on the spectrometer set using a micrometer head, I can select pixels with separated region. Then the DF images for one isolated structure are recorded by the color CCD camera and the DF spectra for the same structure are acquired by the spectrometer set.

3.3.5 *Method for SERS experiment*

1. *Preparation for SERS substrate*

Fabricate copper nanoparticles assembled 3D nanostructures by spark discharge method for SERS substrate.

2. *Sputtering process*

Sputter 5 nm thick Ti layer and 50 nm thick Au layer onto the fabricated metal nanostructures.

3. *SERS experiment for Au sputtered nanostructure array*

a) Chemical binding of BT onto the Au sputtered SERS substrate

1) Prepare gold layer sputtered nanostructures for SERS substrate.

2) In the SERS experiment experimenter should put on personal protective clothing i.e., lab coat, safety mask, and latex gloves when dealing with solutions.

3) By using syringe, deliver 0.5 ~ 1 mL of neat BT into the cleaned glass vial.

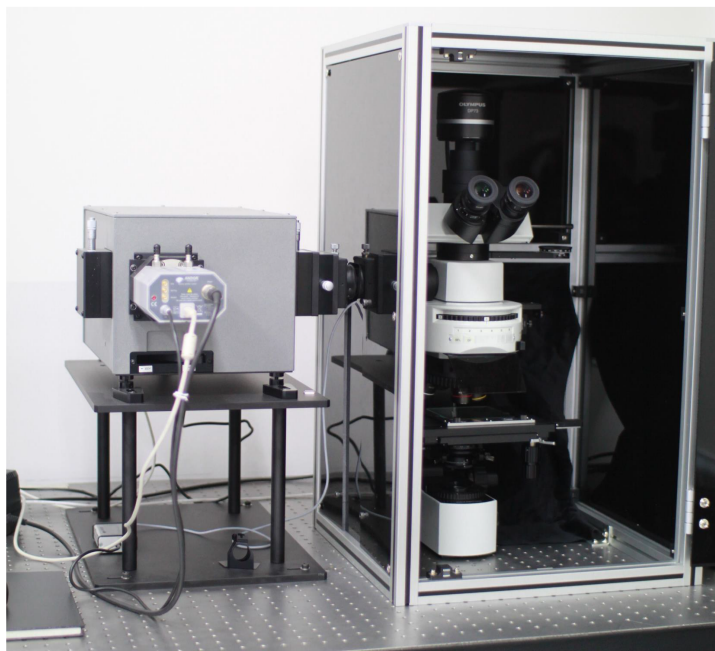
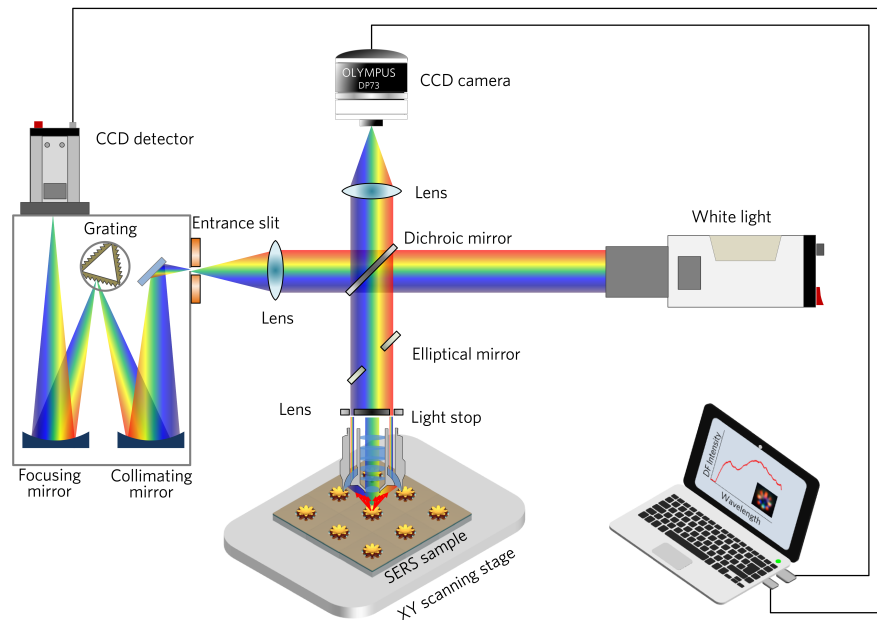


Figure 13: Schematic representation of dark-field spectroscopy system for measuring spectra and images (top), experimental setup for dark-field spectroscopy (bottom)

- 4) Deliver 39 ml ethanol into the cleaned 40 ml glass vial or centrifugal tube.
- 5) Pipette 0.4 μl neat BT 39 ml ethanol in the glass vial via micropipette; stir the BT dissolved BT solution to set the concentration as 10^{-4} M.
- 6) Depending on the number of SERS substrates, 5 ml vials are cleaned .
- 7) Distribute 10^{-4} BT solution into 5 ml glass vials.
- 8) Put the gold sputtered SERS substrates into 10^{-4} BT solution in the 5 ml vials.
- 9) Immerse the SERS substrates in 10^{-4} BT solution for 12 hours.
- 10) Prepare 100 ml ethanol solution in the beaker or glass bottle.
- 11) Take the SERS substrates out of the BT solution and rinse in the ethanol solution several times to get rid of nonbind BT molecules to the surface of SERS substrate.
- 12) By applying nitrogen gas blow gun, the SERS substrates are dried for several minutes

b) Measurement of penetration depth (micro well thickness) and Raman signal from the neat BT (reference) solution (refer to Figure 14)

- 1) Attach four pieces of half scotch tape (62 μm thick) on the large cover glass; the side of inner rectangle of tapes is approximately 5 mm.
- 2) Release one drop of BT solution on the inner rectangle of scotch tapes via pipette.
- 3) A smaller cover glass covers on the large glass; BT drop should be inside the inner rectangle.
- 4) Sealed the four sides of smaller cover glass with silicon on the large cover glass by glue gun.

4. Measurement of Raman signal from BT adsorbed on nanostructures (refer to Figure 14)

a) Raman signal measurement of neat BT solution as a reference sample

- 1) Mount the BT solution sealed by cover glass on the stage of micro Raman microscope.

2) By irradiating 633 nm He-Ne laser with 2 mW onto the BT solution, measure the Raman signal from the neat BT solution for 10 sec through 10× objective (NA = 0.25, beam diameter \approx 3.1 μ m)

b) Raman signal measurement of BT adsorbed onto the SERS substrate

1) Put down the BT adsorbed SERS substrate on the stage of micro Raman microscope.

2) Through 10, 50, and 100× objectives, ensure that the location of nanostructures from the SERS substrate.

3) Determine the center location of one nanostructure where laser is will irradiate through XY scanning stage (10 nm resolution) attached on the stage of micro Raman microscope via 100× objective.

4) Through 100× objective (NA = 0.9, beam diameter \approx 860 nm), the He-Ne laser (633 nm) with 0.16 mW irradiates on the BT adsorbed nanostructure ; the spectrometer collects the back-scattered Raman signal of BT for 30 sec.

3.3.6 Method for DF experiment

a) DF spectra measurement of reference mirror (I_{ref})

1) Turn on the halogen lamp as a light source and CCD of spectrometer set.

2) Place a reference mirror on the stage of DF microscope.

3) Confirm the location of the sample, set the objective magnification from 5× to 100×.

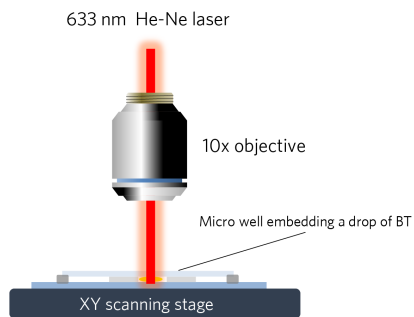
4) Through 100× objective, the spectrometer collects the scatted light from the substrate in the visible range by choosing second grating [Grating 2. VIS-NIR: 1200gr/mm, 500nm blaze (330-850nm)] in the menu.

5) Set the start wavelength and end wavelength to 300 and 800 nm, respectively; enable the step and glue function in the menu to obtain broad band spectra in the visible range.

6) By rotating the knob of horizontal micrometer head on the right side, the width of measured area is adjusted to 11 ~ 14 pixels.

7) By using multi-track option in the menu, the height of the measured area is also is adjusted to 11 ~ 14 pixels ; the pixel size depends on the size of nanostructure.

Raman experiment for bulk (neat) BT



Raman experiment for BT adsorbed nanostructure

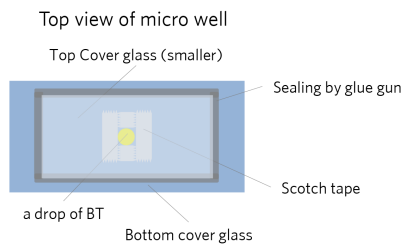
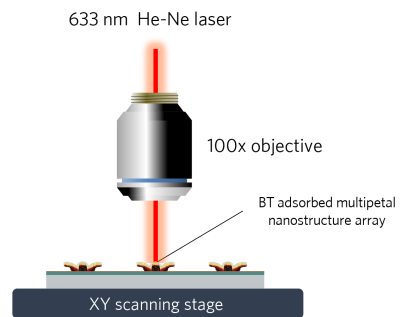


Figure 14: Raman experiments for bulk BT solution (left), BT adsorbed SERS substrate (right)

8) In the visible range, the spectrometer records the scattered light from the mirror (I_{ref}).

b) DF spectra measurement of Au coated nanostructures (I_{m-PF} , $I_{flat Au}$)

1) Prepare the gold sputtered nanostructure sample fabricated by spark discharge method.

2) Mount the sample on the stage of DF microscope.

3) To confirm the location of the sample, set the objective magnification from $5\times$ to $100\times$.

4) Through $100\times$ objective, the spectrometer collects the scattered light from the substrate in the visible range by choosing second grating [Grating 2. VIS-NIR: 1200gr/mm, 500nm blaze (330-850nm)] in the menu.

5) Set the start wavelength and end wavelength to 300 and 800 nm, respectively; enable the step and glue function in the menu to obtain broad band spectra in the visible range.

6) By rotating the knob of horizontal micrometer head on the right side, the width of measured area is adjusted to 11 ~ 14 pixels.

7) By using multi-track option in the menu, the height of the measured area is also adjusted to 11 ~ 14 pixels; the pixel size depends on the size of nanostructure.

8) In the visible range, the spectrometer records the scattered light from the gold coated nanostructure (I_{m-PF}).

9) Measure the DF scattered light from the flat gold surface by repeating 1) ~ 9) steps ($I_{flat Au}$).

c) Measurement of DF scattering images

1) Put down the sample on the stage of DF microscope.

2) Through $100\times$ objective, the spectrometer collects the scattered light from the substrate in the visible range by choosing second grating [Grating 2. VIS-NIR: 1200gr/mm, 500nm blaze (330-850nm)] in the menu.

3) By using $100\times$ objective, 17.3 mega pixel CCD camera, which is coupled to the microscope in the vertical direction, records the reflected multicolor images from the gold coated nanostructure array for several hundred milliseconds.

d) Calculation of DF spectra for multipetal nanostructures

Use below equation to evaluate the DF spectra for one multipetal nanoflower structure, normalizing the incident light source and neglecting the effect of flat gold surface on the SiO₂ pre-pattern .

$$I_{m-PF} = (I_{structure} - I_{flat Au}) / I_{ref}$$

3.4 CONCLUSIONS

In summary, I presented 3D mesoscopic multipetal flowers assembled by metallic nanoparticles as a SERS substrate. Seven orders of SERS enhancement, sufficiency for single molecule detection, and multiresonance features in whole visible frequency range are achieved by plasmonic hot-spot engineering through increasing the number of petals from four to eight. By performing DF imaging, spectrum measurements, and FEM analysis I address that hot-spots and multipole resonance modes are responsible for peculiar optical properties of the multipetal flower structures. Because the nanofabrication technique based on atmospheric spark discharge and electrostatic parallel focusing has capability to construct well-defined, uniform, and reproducible 3D nanostructures in wafer scales, it can not only open the way for manufacturing a reliable 3D SERS substrate sufficient for single molecule detection, but apply to a broad range of novel plasmonic devices.

BIBLIOGRAPHY

- [1] Jeffrey N. Anker, W. Paige Hall, Olga Lyandres, Nilam C. Shah, Jing Zhao, and Richard P. Van Duyne. Biosensing with plasmonic nanosensors. *Nat Mater*, 7(6):442–453, June 2008. (Cited on pages 52 and 57.)
- [2] Katrin Kneipp, Yang Wang, Harald Kneipp, Lev T. Perelman, Irving Itzkan, Ramachandra R. Dasari, and Michael S. Feld. Single molecule detection using surface-enhanced raman scattering (SERS). *Phys. Rev. Lett.*, 78(9):1667, March 1997. (Cited on page 52.)
- [3] Hongxing Xu, Erik J. Bjerneld, Mikael Käll, and Lars Börjesson. Spectroscopy of single hemoglobin molecules by surface enhanced raman scattering. *Phys. Rev. Lett.*, 83(21):4357–4360, 1999. (Cited on page 52.)
- [4] Dong-Kwon Lim, Ki-Seok Jeon, Jae-Ho Hwang, Hyoki Kim, Sunghoon Kwon, Yung Doug Suh, and Jwa-Min Nam. Highly uniform and reproducible surface-enhanced raman scattering from DNA-tailorable nanoparticles with 1-nm interior gap. *Nat. Nanotechnol.*, 6(7):452–460, 2011. (Cited on pages 52 and 53.)
- [5] Fung Suong Ou, Min Hu, Ivan Naumov, Ansoon Kim, Wei Wu, Alexander M. Bratkovsky, Xuema Li, R. Stanley Williams, and Zhiyong Li. Hot-spot engineering in polygonal nanofinger assemblies for surface enhanced raman spectroscopy. *Nano Lett.*, 11(6):2538–2542, 2011. (Cited on pages 52, 53, and 67.)
- [6] Hongxing Xu, Javier Aizpurua, Mikael Käll, and Peter Apell. Electromagnetic contributions to single-molecule sensitivity in surface-enhanced raman scattering. *Phys. Rev. E*, 62(3):4318–4324, 2000. (Cited on page 52.)
- [7] Paul L. Stiles, Jon A. Dieringer, Nilam C. Shah, and Richard P. Van Duyne. Surface-enhanced raman spectroscopy. *Annu. Rev. of Anal. Chem.*, 1(1):601–626, 2008. PMID: 20636091. (Cited on page 52.)

- [8] Alyssa J. Pasquale, Björn M. Reinhard, and Luca Dal Negro. Engineering Photonic–Plasmonic coupling in metal nanoparticle necklaces. *ACS Nano*, 5(8):6578–6585, 2011. (Cited on page 52.)
- [9] Jian Ye, James Andell Hutchison, Hiroshi Uji-i, Johan Hofkens, Liesbet Lagae, Guido Maes, Gustaaf Borghs, and Pol Van Dorpe. Excitation wavelength dependent surface enhanced raman scattering of 4-aminothiophenol on gold nanorings. *Nanoscale*, 4(5):1606–1611, February 2012. (Cited on page 52.)
- [10] Miyu Ozaki, Jun-ichi Kato, and Satoshi Kawata. Surface-plasmon holography with white-light illumination. *Science*, 332(6026):218–220, April 2011. (Cited on page 52.)
- [11] Lukas Novotny and Niek van Hulst. Antennas for light. *Nat. Photon.*, 5(2):83–90, 2011. (Cited on page 52.)
- [12] Henri J. Lezec, Jennifer A. Dionne, and Harry A. Atwater. Negative refraction at visible frequencies. *Science*, 316(5823):430–432, April 2007. (Cited on page 52.)
- [13] Harry A. Atwater and Albert Polman. Plasmonics for improved photovoltaic devices. *Nat. Mater.*, 9(3):205–213, March 2010. (Cited on page 52.)
- [14] Myeong-Lok Seol, Sung-Jin Choi, David J. Baek, Tae Jung Park, Jae-Hyuk Ahn, Sang Yup Lee, and Yang-Kyu Choi. A nanoforest structure for practical surface-enhanced raman scattering substrates. *Nanotechnology*, 23(9):095301, March 2012. (Cited on pages 52 and 53.)
- [15] E. C. Le Ru, E. Blackie, M. Meyer, and P. G. Etchegoin. Surface enhanced raman scattering enhancement factors: A comprehensive study. *J. Phys. Chem. C*, 111(37):13794–13803, 2007. (Cited on pages 52 and 53.)
- [16] P. G. Etchegoin and E. C. Le Ru. A perspective on single molecule SERS: current status and future challenges. *Phys. Chem. Chem. Phys.*, 10(40):6079–6089, October 2008. (Cited on pages 52 and 53.)
- [17] Won-Hwa Park and Zee Hwan Kim. Charge transfer enhancement in the SERS of a single molecule. *Nano Lett.*, 10(10):4040–4048, 2010. (Cited on pages 52 and 53.)

- [18] Xianghu Tang, Wenya Cai, Liangbao Yang, and Jinhui Liu. Highly uniform and optical visualization of SERS substrate for pesticide analysis based on au nanoparticles grafted on dendritic α -Fe₂O₃. *Nanoscale*, 5(22):11193–11199, October 2013. (Cited on page 52.)
- [19] Ying Fang, Nak-Hyun Seong, and Dana D. Dlott. Measurement of the distribution of site enhancements in surface-enhanced raman scattering. *Science*, 321(5887):388–392, July 2008. PMID: 18583578. (Cited on page 52.)
- [20] Wenqi Zhu, Mohamad G. Banaee, Dongxing Wang, Yizhuo Chu, and Kenneth B. Crozier. Lithographically fabricated optical antennas with gaps well below 10 nm. *Small*, 7(13):1761–1766, 2011. (Cited on page 52.)
- [21] H. Wang and N. J. Halas. Mesoscopic au “Meatball” particles. *Adv. Mater.*, 20(4):820–825, 2008. (Cited on page 53.)
- [22] Pola Goldberg-Oppeneheimer, Sumeet Mahajan, and Ullrich Steiner. Hierarchical electrohydrodynamic structures for surface-enhanced raman scattering. *Adv. Mater.*, 24(23):OP175–OP180, 2012. (Cited on page 53.)
- [23] Seunghyun Lee, Myung Gwan Hahm, Robert Vajtai, Daniel P. Hashim, Theerapol Thurakitserree, Alin Cristian Chipara, Pulickel M. Ajayan, and Jason H. Hafner. Utilizing 3D SERS active volumes in aligned carbon nanotube scaffold substrates. *Adv. Mater.*, 24(38):5261–5266, 2012. (Cited on page 53.)
- [24] Young-Jae Oh and Ki-Hun Jeong. Glass nanopillar arrays with nanogap-rich silver nanoislands for highly intense surface enhanced raman scattering. *Advanced Materials*, 24(17):2234–2237, 2012. (Cited on pages 53 and 75.)
- [25] Michael Stenbæk Schmidt, Jörg Hübner, and Anja Boisen. Large area fabrication of leaning silicon nanopillars for surface enhanced raman spectroscopy. *Adv. Mater.*, 24(10):OP11–OP18, 2012. (Cited on page 53.)
- [26] Hyoungchul Kim, Jaehyun Kim, Hongjoo Yang, Jeongsoo Suh, Taeyoung Kim, Bangwoo Han, Sungwon Kim, Dae Seong Kim, Peter V. Pikhitsa, and Mansoo Choi. Parallel patterning of nanopar-

- ticles via electrodynamic focusing of charged aerosols: *Nat Nano*, 1(2):117–121, 2006. (Cited on pages 53 and 54.)
- [27] Sukbeom You, Kyuhee Han, Hyoungchul Kim, Heechul Lee, Chang Gyu Woo, Changui Jeong, Woongsik Nam, and Mansoo Choi. High-resolution, parallel patterning of nanoparticles via an ion-induced focusing mask. *Small*, 6(19):2146–2152, 2010. (Cited on page 53.)
- [28] Mansoo Choi, Heechul Lee, Sukbeom You, and Changkyu Woo. Array formation of 3-d nanostructure of nanoparticle via electrodynamic focusing of charged aerosols. *American Association for Aerosol Research*, Presented at 27th Annual Conference of AAAR: Mt. Laurel, NJ:Abstract 2D.04, October 2008. (Cited on page 53.)
- [29] Heechul Lee, Sukbeom You, Peter V. Pikhitsa, Junhoi Kim, Sunghoon Kwon, Chang Gyu Woo, and Mansoo Choi. Three-dimensional assembly of nanoparticles from charged aerosols. *Nano Lett.*, 11(1):119–124, 2011. (Cited on pages 53, 54, and 55.)
- [30] N. S. Tabrizi, M. Ullmann, V. A. Vons, U. Lafont, and A. Schmidt-Ott. Generation of nanoparticles by spark discharge. *Journal of Nanoparticle Research*, 11(2):315–332, May 2008. (Cited on page 54.)
- [31] Kyuhee Han, Woongsik Kim, Jiwon Yu, Jeonghoon Lee, Heechul Lee, Chang Gyu Woo, and Mansoo Choi. A study of pin-to-plate type spark discharge generator for producing unagglomerated nanoaerosols. *Journal of Aerosol Science*, 52(0):80–88, 2012. (Cited on page 54.)
- [32] Sukbeom You and Mansoo Choi. Numerical simulation of microscopic motion and deposition of nanoparticles via electrodynamic focusing. *Journal of Aerosol Science*, 38(11):1140–1149, 2007. (Cited on page 54.)
- [33] Taejoon Kang, Seung Min Yoo, Ilsun Yoon, Sang Yup Lee, and Bongsoo Kim. Patterned multiplex pathogen DNA detection by au particle-on-wire SERS sensor. *Nano Lett.*, 10(4):1189–1193, 2010. (Cited on page 57.)
- [34] Tai Ha Joo, Myung Soo Kim, and Kwan Kim. Surface-enhanced raman scattering of benzenethiol in silver sol. *Journal of Raman Spectroscopy*, 18(1):57–60, 1987. (Cited on page 58.)

- [35] Gorachand Ghosh. Dispersion-equation coefficients for the refractive index and birefringence of calcite and quartz crystals. *Optics Communications*, 163(1–3):95–102, 1999. (Cited on page 60.)
- [36] Edward D Palik. *Handbook of optical constants of solids*. Academic Press, Orlando, 1985. (Cited on page 60.)
- [37] P. B. Johnson and R. W. Christy. Optical constants of the noble metals. *Phys. Rev. B*, 6(12):4370–4379, 1972. (Cited on page 60.)
- [38] M. A. Seo, H. R. Park, S. M. Koo, D. J. Park, J. H. Kang, O. K. Suwal, S. S. Choi, P. C. M. Planken, G. S. Park, N. K. Park, Q. H. Park, and D. S. Kim. Terahertz field enhancement by a metallic nano slit operating beyond the skin-depth limit. *Nature Photonics*, 3(3):152–156, 2009. (Cited on page 60.)
- [39] J. H. Kang, D. S. Kim, and Q-Han Park. Local capacitor model for plasmonic electric field enhancement. *Phys. Rev. Lett.*, 102(9):093906, 2009. (Cited on page 60.)
- [40] Taejoon Kang, Ilsun Yoon, Ki-Seok Jeon, Wonjun Choi, Yonghoon Lee, Kwanyong Seo, Youngdong Yoo, Q-Han Park, Hyotcherl Ihee, Yung Doug Suh, and Bongsoo Kim. Creating well-defined hot spots for surface-enhanced raman scattering by single-crystalline noble metal nanowire pairs. *J. Phys. Chem. C*, 113(18):7492–7496, 2009. (Cited on page 60.)
- [41] Peter M. Goodwin, W. Patrick Ambrose, John C. Martin, and Richard A. Keller. Spatial dependence of the optical collection efficiency in flow cytometry. *Cytometry*, 21(2):133–144, 1995. (Cited on page 73.)
- [42] James Pawley. *Handbook of Biological Confocal Microscopy (3rd edition)*. Springer, 3rd edition edition, 2006. (Cited on page 74.)
- [43] Nicholas C Linn, Chih-Hung Sun, Ajay Arya, Peng Jiang, and Bin Jiang. Surface-enhanced raman scattering on periodic metal nanotips with tunable sharpness. *Nanotechnology*, 20(22):225303, June 2009. (Cited on page 74.)
- [44] Cheng-an Tao, Qi An, Wei Zhu, Haowei Yang, Weina Li, Changxu Lin, Dan Xu, and Guangtao Li. Cucurbit[n]urils as a SERS hot-

spot nanocontainer through bridging gold nanoparticles. *Chem. Commun.*, 47(35):9867–9869, August 2011. (Cited on page 75.)

[45] Kuan Soo Shin, Hyunwoo Ryoo, Yoon Mi Lee, and Kwan Kim. Surface-enhanced raman scattering of benzenethiol adsorbed on silver-exchanged copper powders. *Bulletin of the Korean Chemical Society*, 29(2):445–449, 2008. (Cited on page 75.)

[46] ZhiQiang Guan, Ulf Håkanson, Nicklas Anttu, Hong Wei, HongQi Xu, Lars Montelius, and HongXing Xu. Surface-enhanced raman scattering on dual-layer metallic grating structures. *Chin. Sci. Bull.*, 55(24):2643–2648, August 2010. (Cited on page 75.)

Abstract

에어로졸 나노입자를 적용한 3차원 플라즈모닉 소자의 제조와 특성 분석

서울대학교 대학원 기계항공공학부

정 기 남

요약

이번 논문에서는 스파크 방전방법, 증발응축법과 같은 에어로졸 공정을 이용하여 금속나노입자로 구성된 3차원 나노구조물을 제작하고, 이 구조물을 유기태양전지와 표면증강산란(SERS) 소자에 적용하여 이 소자들의 광학적 특성을 분석하고 효율을 증가시키는 연구를 진행하였다.

첫째로, 활성층 아래에 있는 산화몰리브덴 (MoO_3) 과 은나노입자들로 구성된 나노범프구조체를 플라즈모닉 PCDTBT:PC₇₀BM 유기태양전지에 도입하여, 이 소자의 단락전류밀도(J_{SC})와 광전변환효율(PCE)을 증대시키는 연구를 진행하였다. 습식 화학 나노입자 공정에서 흔히 발생하는 입자들의 응집, 불순물 생성, 오염 등의 문제가 발생되지 않는 건식 에어로졸 공정 기반의 증발응축법을 이용하여 20, 40, 60 nm 직경의 은나노입자들을 제조하였다. 시간영역에서의 유한차분법(FDTD)으로 계산된 유기태양전지 소자의 산란 단면적과 활성층 내의 근접장 분포 및 전방산란 효과 결과는 PEDOT:PSS로 구성된 유기태양전지보다

나노범프조립체로 구성된 유기태양전지 소자가 더 우월한 효과를 보였다. 상기 소자의 전류-전압 특성 중 하나인 단락전류밀도는 나노입자의 크기에 비례하여 증가하는 경향을 보이며, 또한 최고효율은 40 nm 크기의 은입자를 도핑한 유기태양전지에서 얻어진다. 은입자 크기에 따른 증가된 소자 성능은 가시광선 영역에서 은나노입자 주변의 근접장 크기 향상으로부터 유도된 강한 전방산란 효과, 그리고 근적외선 영역에서 나노범프 위쪽 Al 음극과 아래쪽 ITO 양극 사이에서 발생한 다중반사효과로 설명할 수 있다. 그러므로, 이번 에어로졸 나노입자를 도입한 플라즈모닉 유기태양전지 연구는 다양한 유기태양전지 소자에 사용되어 광대역 파장 범위에서 효율적으로 빛을 활용할 수 있는 유망한 플랫폼이 될 수 있을 것이다.

둘째로, 에어로졸 금속 나노입자들로 구성된 3차원 꽃 잎모양의 나노구조물을 표면증강라만산란(SERS) 기판에 적용하였다. 단일분자를 충분히 측정할 수 있는 10^7 정도의 SERS 증강인자가 산출되었고, 꽃 잎의 개수를 4개에서 8개로 증가시키는 플라즈모닉 핫스팟 엔지니어링으로부터 모든 가시광선 영역에서 보여지는 다중극공진 특성이 도출되었다. 암시아산란 스펙트럼 및 이미지, 유한요소법 분석 등을 통해서, 핫스팟과 다중극공명 모드는 꽃잎구조물의 독특한 광학적 속성에 기인함을 보였다. 기상, 상압방식의 스파크 방전 방식과 정전기 병렬 포커싱에 기반을 둔 나노제조기술은 웨이퍼 스케일에서 충분히 정의되고, 균일하고, 재현성있는 3차원 나노구조물을 제조할 수 있는 기술이다. 따라서, 상기 에어로졸 기반의 나노입자제조기술은 단일분자도 충분히 측정가능한 신뢰성 있는 3차원 SERS 기판 제작과 다양한 종류의 새로운 플라즈모닉 소자의 제작에도 적용가능한 새로운 접근법으로 활용될 것이다.

입사되는 광원과 상호작용을 통해 나노입자 구조체 주변의 전기장을 증폭시킬 수 있는 에어로졸 나노입자를 도입한 3차원 플라즈모닉 소자는 넓은 파장대의 빛을 활용할 수 있는 다양한 나노스케일의 광전자 소자의 발전에 기틀을 마련할 것으로 전망한다.

주요어: 에어로졸 나노입자, 스파크 방전 방법, 증발응축 방법, 유기태양전지, 표면증강라만신란, 플라즈몬

학 번: 2009-30168